Schweizerische Eidgenossenschaft
Confédération suisse
Confederazione Svizzera
Confederaziun svizra

Eidgenössisches Departement für
Umwelt, Verkehr, Energie und Kommunikation UVEK

Bundesamt für Energie BFE

Abschlussbericht 5. April 2012

MC3

Future Mobility using Communication, Computation and Control

Auftraggeber:
Bundesamt für Energie BFE
Forschungsprogramm Verkehr
CH-3003 Bern
www.bfe.admin.ch

Auftragnehmer:
ETH Zürich
Institut für Dynamische Systeme und Regelungstechnik (IDSC)
Autonomous Systems Laboratory (ASL)
Rämistrasse 101
CH-8092 Zürich
www.ethz.ch

EPF Lausanne
Laboratoire de Technologie des Composites et Polymères (LTC)
Station 12
CH-1015 Lausanne Ort
www.epfl.ch

Autor:
Prof. Dr. Lino Guzzella, ETH Zürich, Institut für Dynamische Systeme und Regelungstechnik, guzzella@idsc.mavt.ethz.ch

BFE-Bereichsleiter: Martin Pulfer
BFE-Programmleiter: Martin Pulfer
BFE-Vertrags- und Projektnummer: 153018 / 102532

Zusammenfassung

Das Grundlagenprojekt *MC3 – Future Mobility using Communication, Computation and Control* untersuchte die Möglichkeiten und die Voraussetzungen für einen radikalen Leichtbau von Fahrzeugen, der eine Absenkung des spezifischen Kraftstoffverbrauchs um Faktor 3 zum Ziel hat. Das Gesamtprojekt war in drei Teilprojekte unterteilt:

1. Neue Materialien für Leichtbaufahrzeuge
2. Autonome Fahrzeuge und Kollisionsvermeidung
3. Optimierung und Steuerung von Drive-by-Wire-Fahrzeugen

Teilprojekt 1, *Neue Materialien für Leichtbaufahrzeuge*, entwickelte einen neuartigen Faserverbundwerkstoff mit anpassungsfähigen dynamischen Eigenschaften.

Teilprojekt 2, *Autonome Fahrzeuge und Kollisionsvermeidung,* untersuchte die Navigation autonomer Fahrzeuge in einer hochdynamischen Umgebung.

Teilprojekt 3, *Optimierung und Steuerung von Drive-by-Wire-Fahrzeugen*, befasste sich mit der aktiven Sicherheit des Fahrzeugs im Grenzbereich, insbesondere mit der optimalen Steuerung von Ausweichmanövern.

Hintergrund und Projektziele

Mit welcher Kombination aus Technik und Vernunft lässt sich in der Zukunft eine sinnvolle und global tragbare Mobilität ermöglichen? Zur Automobiltechnik lässt sich mit einem Zeithorizont von etwa 20 Jahren ein realistisches Ziel formulieren: den Treibstoffverbrauch von heute knapp 7 Liter pro 100 km auf 2 bis 3 Liter pro 100 km zu reduzieren. Diese Autos müssen vernünftige Fahrleistungen haben, kostengünstig und sicher sein, keine gesundheitsgefährdenden Schadstoffe ausstossen. Und vor allem müssen sie kleiner und leichter sein. Das Gewicht ist neben dem Wirkungsgrad des Motors der entscheidende Schlüssel zur Senkung des Kraftstoffverbrauchs.

Eine drastische Reduktion des Fahrzeuggewichts ist nur auf Kosten der *passiven* Sicherheit möglich. Daher erfordern Leichtbaufahrzeuge ein hohes Mass an *aktiver* Sicherheit. Neben Konstruktion und Material des Fahrzeugs bilden Kommunikation (z.B. von Fahrzeug zu Fahrzeug), Navigation (z.B. via Satellit), Computerprogramme (z.B. zur Bewegungsplanung und Kollisionsvermeidung), Sensorik (Radar, Kamera etc.) und Steuerung (insbesondere von Drive-by-Wire-Fahrzeugen) zentrale Forschungsfelder für Leichtbaufahrzeuge.

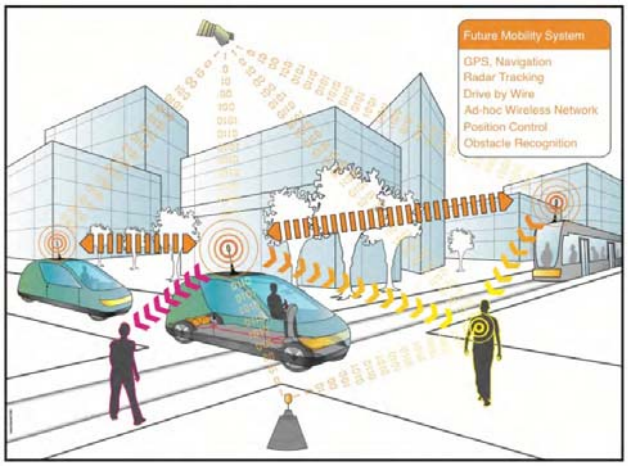

Abbildung 1: Künstlerische Darstellung eines vernetzten Verkehrssystems

Fernziel ist, durch aktive Sicherheit Verkehrsunfälle faktisch unmöglich zu machen. Dadurch liesse sich über den Verzicht auf passive Sicherheitselemente das Fahrzeuggewicht und somit der Kraftstoffverbrauch entscheidend senken. Im Rahmen dieser Vision ist es das Ziel

des vorliegenden Projektes, Ideen und Ansätze für die genannten Herausforderungen zu erarbeiten.

Durchgeführte Arbeiten und erreichte Ergebnisse

Das Gesamtprojekt ist in drei Teilprojekte unterteilt: *Neue Materialien für Leichtbaufahrzeuge, Autonome Fahrzeuge und Kollisionsvermeidung* und *Optimierung und Steuerung von Drive-by-Wire-Fahrzeugen.*

Neue Materialien für Leichtbaufahrzeuge

Forschungsziel des ersten Teilprojekts war die Entwicklung eines neuartigen Faserverbundwerkstoffs mit anpassungsfähigen dynamischen Eigenschaften. Hiermit liessen sich Steifigkeit und Dämpfungseigenschaften des Materials aktiv beeinflussen. Damit könnte bei einem Unfall die Karrosserie des Fahrzeugs, je nach Art des Unfalls, in ihren strukturellen Eigenschaften verändert und so die schädlichen Auswirkungen des Unfalls minimiert werden.

Die durch dieses Projekt entwickelten piezoelektrischen Verbundwerkstoffe und ihre optimierte Herstellung sind ein erster Schritt in diese Richtung. Die piezoelektrischen Eigenschaften ermöglichen eine Verwendung der Materials als Kraft- oder Drucksensor. Zusätzlich weist das Material eine hohe Dichtheit auf, was es z.B. für die Speicherung von Wasserstoff prädestiniert. . Die entwickelten Materialien kämen hierbei in mehrfacher Hinsicht zugute: durch ihr geringes Gewicht, durch ihre hohe Gasundurchlässigkeit und durch eine piezoelektrische Überwachbarkeit des Druckzustands.

Die Verwendung der piezoelektrischen Eigenschaft in umgekehrter Richtung (von einer Stellspannung zu einer mechanischen Eigenschaft) erfordert noch weitere Forschung. Hierzu sind noch komplexere Materialstrukturen notwendig.

Autonome Fahrzeuge und Kollisionsvermeidung

Das zweite Teilprojekt befasst sich mit der Navigation autonomer Fahrzeuge in einer hochdynamischen und unstrukturierten Innerortsumgebung als auch auf einer strukturierten Autobahn. Ziel ist die Bewegungsplanung und Vermeidung von Kollisionen während des normalen Fahrbetriebs, d.h. in stabilem Fahrzustand. Das entwickelte System muss in der Lage sein, unter Einbeziehung der Randbedingungen von Fahrzeug und Umwelt hochkomplexe Manöver zu planen und durchzuführen. Die dynamischen Anforderungen erlauben dabei nur eine begrenzte Rechenzeit.

Es wurde ein Verfahren entwickelt, das über einen kurzen Zeithorizont die Bewegung von möglichen Hindernissen in der Umgebung des Fahrzeuges und des Fahrzeugs selber prädiktiert. Dieser Prädiktion liegt ein physikalisches Modell der bewegten Körper zu Grunde. Dadurch wird einerseits die Genauigkeit der Prädiktion deutlich verbessert, andererseits können gefährliche Situation vorhergesehen werden bevor sie überhaupt auftreten. Somit wird der notwendige Stelleingriff minimiert.

Mit einem Demonstrator-Roboter wurden die Simulationsresultate bestätigt. Dabei zeigt sich aber auch, dass das Verfahren beim Übergang von einem Ausweichmanöver zum nächsten Schwächen zeigt, die zu gefährlichen Situationen führen können. Diese Anfälligkeit ist allerdings auch vom menschlichen Verhalten her bekannt und kann so in der Simulation jetzt weiter untersucht werden.

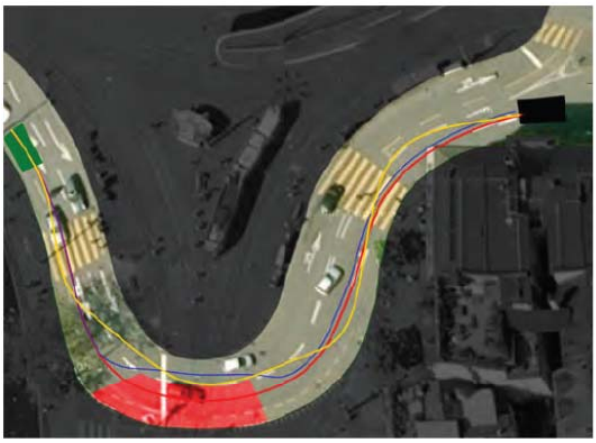

Abbildung 2: Bewegungsplanung am Zürcher Central. Die Ausgangsposition ist grün, die Zielposition schwarz. Im roten Bereich muss ein Pannenfahrzeug überholt werden. Die blaue Linie markiert den geplanten optimalen Pfad.

Optimierung und Steuerung von Drive-by-Wire-Fahrzeugen

Während sich das zweite Teilprojekt mit dem stabilen Fahrbereich befasst, zielt das dritte Teilprojekt auf sicherheitskritische Fahrsituationen im Grenzbereich unter dem Aspekt der aktiven Sicherheit. Insbesondere wurde das Ausweichen um ein stehendes Hindernis in einem dreiphasigen Manöver, s. Abb. 3, untersucht und optimiert.

Verschiedene Fahrzeugkonfigurationen, z.B. solche mit und ohne Hinterachslenkung, wurden verglichen und die Auswirkungen auf die Manövrierfähigkeit quantifiziert. Dies erlaubt eine fundierte Einschätzung der Vorteile zusätzlicher Freiheitsgrade der Steuerung gegenüber ihrem Aufwand.

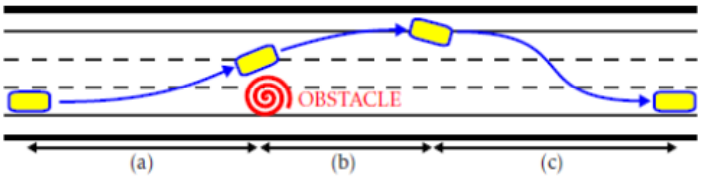

Abbildung 3: Phasen eines Ausweichmanövers um ein stehendes Hindernis. Phase (a) vermeidet die Kollision, Phase (b) verhindert das Abkommen von der Fahrbahn, Phase (c) führt auf die ursprüngliche Fahrspur zurück.

Es zeigt sich, dass das rein Ausweichmanöver nicht stark von zusätzlichen Freiheitsgraden in der Lenkung profitieren kann. Andererseits kann das Wiedereinschwenken zur nominellen Trajektorie deutlich besser gestaltet werden.

Zusätzlich wurde noch die Möglichkeit der aktiven Beeinflussung der Reifencharakteristik untersucht. Auch hier zeigt sich der erwartete Effekt (besserer Reibbeiwert, besseres Ausweichen). Die Sensitivität ist allerdings eher klein, sodass sich weitere Untersuchungen in diese Richtung zur Zeit nicht aufdrängen.

Nationale Zusammenarbeit

Teilprojekt 1, *Neue Materialien für Leichtbaufahrzeuge*, wurde am Laboratoire de Technologie des Composites et Polymères der EPFL durchgeführt und zusätzlich durch den SNF gefördert.

Teilprojekt 2, *Autonome Fahrzeuge und Kollisionsvermeidung,* wurde am Autonomous System Lab der ETH Zürich durchgeführt und zusätzlich durch den SNF.

Teilprojekt 3, *Optimierung und Steuerung von Drive-by-Wire-Fahrzeugen,* wurde am Institut für Dynamische Systeme und Regelungstechnik der ETH Zürich durchgeführt.

Internationale Zusammenarbeit

Teilprojekt 2, *Autonome Fahrzeuge und Kollisionsvermeidung,* wurde durch das EU-Rahmenprogramm EUROPA (FP7-231888) gefördert.

Final Report

MC3 – Future Mobility using Communication, Computation and Control

Lino Guzzella, February 10, 2012

Introduction

A radical reduction of fuel consumption of road vehicles (by up to a factor of three) requires a drastic reduction of the vehicle mass and an improved efficiency of the propulsion system. Unfortunately, low-cost lightweight vehicles cannot reach the same *passive safety* levels as modern heavier vehicles do. This project focused on *lightweight vehicles* and analyzed new ideas for the *active safety* of such automobiles. Communication (vehicle-to-vehicle, etc.), navigation (through satellites and road beacons), computation (trajectory planning, collision avoidance, etc.), sensing (radar, video, etc.) and control (fully drive-by-wire vehicles) are the most important components of such a system. The ultimate objective is to render road accidents virtually impossible. If this long-range goal is attained, vehicles can be built without any inherent passive safety structures and devices that currently add a lot of weight to vehicles. Combined with optimized propulsion, such vehicles have the potential to achieve those low fuel consumption figures that are necessary to satisfy the future mobility needs.

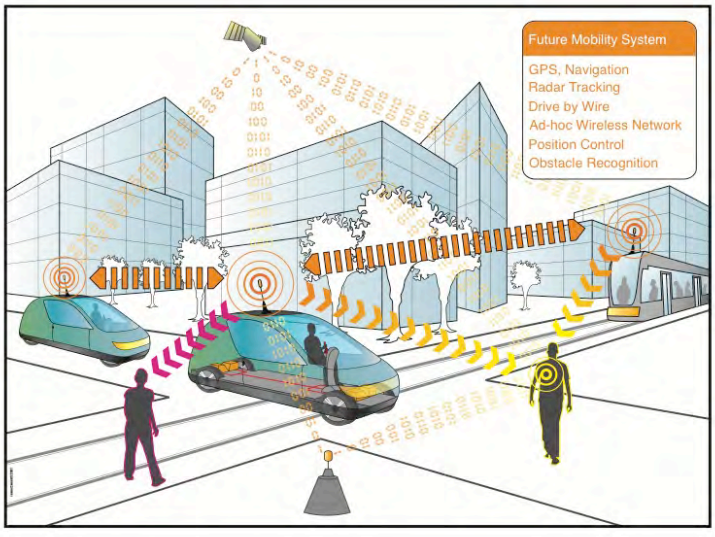

Figure 1: Artists visualization of a networked traffic system.

Obviously, such a radically new transportation system requires enormous research efforts before it can become reality. In this MC3-project, three subprojects are embedded in this general quest each aiming at contributing towards the general vision sketched above.

These three projects were:

(1) New materials and ideas for lightweight vehicles.

(2) Autonomous vehicles and collision avoidance.

(3) Optimization and control for fully drive-by-wire vehicles.

The results achieved by each of these three projects are summarized below. More detailed in formation is given in the three reports and in the publications attached to this summary report.

It is worth mentioning here, that subproject (3) was terminated prematurely after 2 years because the student working on it decided to pursue his career in industry. The corresponding funds were returned to the BfE.

Subproject 1 "New Materials an Ideas for Lightweight Vehicles"

Sara Dalle Vacche, Yves Leterrier, Véronique Michaud, Jan-Anders E. Månson, Laboratoire de Technologie des Composites et Polymères (LTC), Ecole Polytechnique Fédérale de Lausanne (EPFL), CH-1015 Lausanne, Switzerland

Summary:

The objective of the research work at LTC-EPFL in the framework of the MC3 project was to develop a novel fiber-reinforced composite material with adaptable dynamic properties, enabling an active control of the stiffness vs. damping of a structure through tailoring of the fiber/matrix interfacial force transfer.

The piezoelectric composites, and their optimized processing methods developed in this project are directly applicable to a range of applications. One specific development beyond the project is in the form of self-sensing 'liners' for lightweight composite vessels for high-pressure hydrogen storage (SNSF – Nano Tera 'Greenpower' fund). These novel materials combine two functions: vessel tightness thanks to their high gas barrier properties, and safety through piezoelectric monitoring of the vessel pressure state.

Publications:

S. Dalle Vacche, Y. Leterrier, V. Michaud, D. Damjanovic, J-A.E. Månson, '*The effect of processing conditions on the morphology, mechanical and electrical properties of $BaTiO_3$-polymer composites*', oral presentation at Polychar18, April 6-10, 2010, Siegen, Germany.

S. Dalle Vacche, F. Oliveira, Y. Leterrier, V. Michaud, D. Damjanovic, J.-A.E. Månson, '*The effect of processing conditions on the morphology, thermomechanical, dielectric and piezoelectric properties of P(VDF-TrFE)/$BaTiO_3$ composites*', accepted in the Journal of Materials Science.

Subproject 2 “Autonomous Vehicles and Collision Avoidance”

Martin Rufli, Luciano Spinello and Roland Siegwart, Autonomous System Lab, ETH Zurich, CH-8092 Zurich, Switzerland

Summary:

Within the framework of the mc3 project, lightweight robotic platforms are envisioned to safely navigate through cluttered, dynamic, unstructured inner-city as well as structured highway environments. Our contribution lies in a navigation approach, which performs motion planning and collision avoidance during regular vehicle operation, i.e. well within the limits of stable wheel traction. On the motion planning side, this calls for collision-aware systems, which respect vehicle and environmental constraints and which are able to plan and perform highly complex maneuvers in constrained areas. In order to guarantee responsive vehicle behavior in dynamic environments, the time spent computing such maneuvers needs to be low.

Within the mc3 project we developed a novel local planning and collision avoidance method based on discrete graph search. The novelty of our method is twofold: first, the generated solution trajectory is model based and can thus be directly executed by the robot with minimal control interference. Second, we successfully employed motion prediction to actively foresee and prevent dangerous situations before they arise. Tests on a differential-drive demonstrator robot confirm the superior theoretical properties in practice. Nonetheless, we also observed our algorithm is prone to switching behaviors between different avoidance maneuvers. This effect, which is also regularly encountered between humans, can lead to dangerous situations. In the future, we will further investigate to which extent these situations can be avoided or mitigated through the use of appropriate algorithms. In this regard, the concept of Velocity Obstacles [11] – mentioned in the review – seems most promising.

Publications:

M. Ru_i and R. Siegwart. On the Application of the D* Search Algorithm to Time-Based Planning on Lattice Graphs. In Proceedings of the European Conference on Mobile Robots (ECMR) , 2009.

M. Ru_i and R. Siegwart. On the Design of Deformable Input- / State-Lattice Graphs. In Proceedings of the IEEE International Conference on Robotics and Automation (ICRA) , 2010.

Subproject 3 “Fully Drive-by-wire Vehicles”

Patrick Dingle, Stephan Pleines, Lino Guzzella, Institute for Dynamic Systems and Control, ETH Zurich, CH-8092 Zurich, Switzerland

Summary:

A critical safety metric in the design of automobiles is maneuverability. This ability for vehicles to quickly change velocity is especially critical in emergency situations. The purpose of this research project was to formulate an optimal control based method that can be used to quantify the performance of a vehicle during an emergency lane-change maneuver, and to utilize the method to quantify the advantages of vehicles with various actuated degrees of freedom. In particular, the performance of two-wheel actively steered vehicles was compared to vehicles that also have active rear-wheel steering. A planar single-track bicycle model was assumed, the pitch and the roll dynamics are therefore neglected. Nonlinear tire dynamics were assumed and turned out to be the critical constraint that bounds vehicle performance. Finally, all vehicles were assumed to have unconstrained and independently controlled braking torques that can be applied to the front and rear wheels.

Publications:

Dingle P, Guzzella L., "Optimal Emergency Maneuvers on Highways for Passenger Vehicles with Two- and Four-Wheel Active Steering," 2010, Proceedings American Control Conference, Baltimore (MD), pp- 5374-5381

MC3 Final Report – February 2012

Sara Dalle Vacche, Yves Leterrier, Véronique Michaud, Jan-Anders E. Månson
Laboratoire de Technologie des Composites et Polymères (LTC)
Ecole Polytechnique Fédérale de Lausanne (EPFL)
CH-1015 Lausanne, Switzerland

Summary

The objective of the research work at LTC-EPFL in the framework of the MC3 project was to develop a novel fiber-reinforced composite material with adaptable dynamic properties, enabling an active control of the stiffness vs. damping of a structure through tailoring of the fiber/matrix interfacial force transfer. The approach identified in the initial part of the project was based on a piezoelectric coating applied on the reinforcing fibers (see report of March 2009). Multilayer demonstrator beams based on polyvinylidene fluoride (PVDF, a piezoelectric polymer) coated with Ag colloid paste electrodes on rigid PVC strips were produced and their damping behavior upon application of an electrical field was analyzed. The results were not conclusive, due to i) issues related to the friction behavior of the interfaces controlled by the roughness of the Ag electrodes and ii) the limited piezoelectric coefficient of PVDF. Focus was put on the development of piezoelectric polymer composites, based on copolymers of PVDF with trifluoroethylene, P(VDF-TrFE) and barium titanate particles, as an alternative to lead-containing piezoelectric PZT ceramics. P(VDF-TrFE) have large relative permittivity and high dielectric strength, and exhibit a relatively large piezoelectric activity. It is also possible to polarize independently the polymer and the ceramic phases therefore adding an additional degree of freedom to the tuning of the composite properties.

(0-3) P(VDF-TrFE)/$BaTiO_3$ composites containing up to 60 vol% of ceramic phase were prepared by solvent casting or compression molding (see report of November 2010). Three types of ceramic particles with different size distributions were selected. Both untreated and silylated (aminopropyltriethoxy silane) particles were prepared. The thermomechanical, dielectric, and piezoelectric properties of the composites were investigated, and discussed in the light of the properties of the basic components, the processing route and the resulting morphology. The crystalline structure of the P(VDF-TrFE) matrix was found to highly depend on the processing route, while the structure of $BaTiO_3$ was not affected by any of the processing steps. The mechanical properties of the solvent cast materials showed a maximum at 30 vol% $BaTiO_3$, while they increased monotonically with $BaTiO_3$ content for compression molded materials. This difference was attributed to a higher amount of porosity and inhomogeneity in the solvent cast composites. Permittivity as high as 120 and piezoelectric coefficient d_{33} up to 32 pC/N were obtained for compression molded composites, and the observed decrease in d_{33} with aging time was attributed to the effect of mechanical stress release in the polymer matrix. These results were presented in an international conference and are analyzed in a paper accepted for publication in the Journal of Materials Science.

The silylation of the particles highly improved the tensile storage modulus and the dielectric properties of the solvent cast composite materials, especially at high particle fraction. The dielectric losses at low frequency were reduced for the compression molded materials, although their permittivity was also slightly reduced at the same time. The piezoelectric

response and the aging behavior of the materials produced with surface modified ceramics was also improved compared with untreated particles (Figure 1).

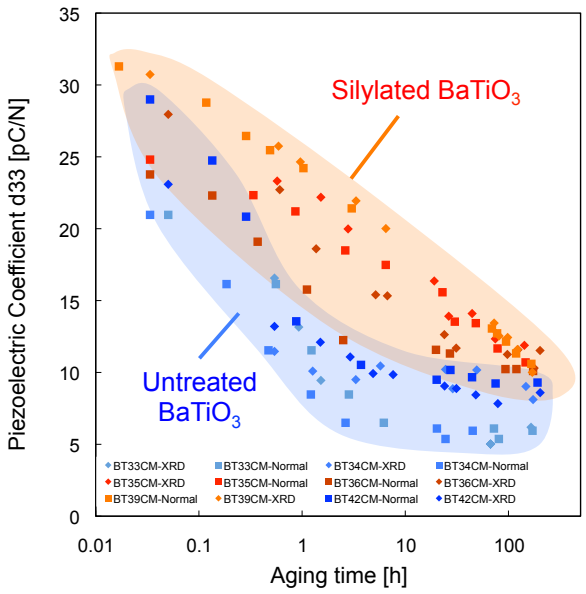

Figure 1. Influence of particle surface treatment on piezoelectric properties of $BaTiO_3$ (60 vol%) P(VDF-TrFE) composites.

The production of fiber reinforced polymer composite materials with adaptable dynamic properties based on piezoelectric fiber/matrix interfaces would require additional work. Nevertheless the piezoelectric composites, and their optimized processing methods developed in this project are directly applicable to a range of applications. One specific development beyond the project is in the form of self-sensing 'liners' for lightweight composite vessels for high-pressure hydrogen storage (SNSF – Nano Tera 'Greenpower' fund). These novel materials combine two functions: vessel tightness thanks to their high gas barrier properties, and safety through piezoelectric monitoring of the vessel pressure state.

Publications

S. Dalle Vacche, Y. Leterrier, V. Michaud, D. Damjanovic, J-A.E. Månson, '*The effect of processing conditions on the morphology, mechanical and electrical properties of $BaTiO_3$-polymer composites*', oral presentation at Polychar18, April 6-10, 2010, Siegen, Germany.

S. Dalle Vacche, F. Oliveira, Y. Leterrier, V. Michaud, D. Damjanovic, J.-A.E. Månson, '*The effect of processing conditions on the morphology, thermomechanical, dielectric and piezoelectric properties of P(VDF-TrFE)/$BaTiO_3$ composites*', accepted in the Journal of Materials Science.

THE EFFECT OF PROCESSING CONDITIONS ON THE MORPHOLOGY, MECHANICAL AND ELECTRICAL PROPERTIES OF $BaTiO_3$-POLYMER COMPOSITES.

Sara Dalle Vacche (Dr)*, Yves Leterrier (Dr)*, Véronique Michaud (Dr)*, Dragan Damjanovic (Prof), Jan-Anders E. Månson (Prof)***

** Laboratoire de Technologie des Composites et Polymères – Ecole Polytechnique Fédérale de Lausanne, Address: Station 12,1015 Lausanne, Switzerland*
*** Ceramics Laboratory – Ecole Polytechnique Fédérale de Lausanne, Address: Station 12, 1015 Lausanne, Switzerland*
E-mail: sara.dallevacche@epfl.ch

Keywords: *Ferroelectric composites, Thermomechanical properties, Electrical properties.*

Ferroelectric ceramic – polymer composites have a unique mix of electrical and mechanical properties. Piezoelectric and pyroelectric activity, a wide range of dielectric constants and high breakdown strength are combined with mechanical flexibility, formability and low acoustic impedance. Furthermore their properties may be tailored by the judicious choice of the polymeric matrix and ceramic filler, of their volume fraction, and of the type of connectivity, making these materials very attractive for applications as embedded capacitors, sensors and actuators. Composites with 0-3 connectivity, i.e. a continuous polymer matrix filled with a ceramic phase discontinuous in all directions, are particularly interesting because of their relative ease of fabrication and processing. The functionality of these composite materials is mostly due to the dielectric, ferroelectric and piezoelectric properties of the ceramic phase, which therefore often needs to constitute more than 50% in volume. On the other hand the possibility of integrating these composites as embedded devices in host structures, which are often polymer based, or using them as efficient actuators depends greatly on their thermomechanical properties. Most of the studies on ferroelectric ceramic-polymer composites, however, focus on their electrical properties, and relatively few systematic studies on their thermal and mechanical behaviour have been published so far. Furthermore the ceramic volume fractions considered are often much lower than those used in most applications [1, 2], studies of highly filled composites mainly being limited to lead-based ferroelectric materials [3].
In the present study 0-3 $BaTiO_3$ – polymer composites were prepared, containing up to 60% volume fraction of ceramic phase. $BaTiO_3$ was chosen as the ceramic filler as it is a common piezoelectric material with high dielectric constant, having the additional benefit from an environmental point of view of being lead-free. For the matrix, a low viscosity epoxy resin and a polyvinylidene fluoride based polymer were chosen. The first is a thermoset resin commonly used for several applications, and the second is a thermoplastic semicrystalline polymer which displays piezoelectric activity. A common route for achieving very high loading of ceramic filler is the use of solvents to reduce the viscosity during processing. However, as the materials prepared via the solvent route were found to have poor mechanical properties, attributed to the presence of residual solvent, most of the effort focused on obtaining high ceramic volume fractions via a solvent free process.
The thermomechanical, dielectric, ferroelectric and piezoelectric properties of the obtained composites were investigated, and discussed in the light of the properties of the basic components, the processing route and the resulting morphology. X-ray diffraction was carried out to determine the crystal structure of the $BaTiO_3$ in the pure powder and in the composites, confirming that processing did not alter the crystallographic structure of the ceramic phase. Scanning electron microscope observation of fracture surfaces of the composites evidenced that a satisfactorily homogeneous dispersion of $BaTiO_3$ in the matrix could be obtained, although aggregates with diameter of some micrometers and some porosity were detected. The thermal and mechanical behaviour of the composites was studied by differential scanning calorimetry and dynamic mechanical analysis. The glass transition temperature was found not to significantly depend on the amount of filler, while both the storage and loss moduli increased upon addition of $BaTiO_3$. Furthermore, all the composites displayed a region of linear stress-strain behaviour smaller than the pure matrices. Finally, experimental results also evidenced the possibility to obtain low leakage current and high breakdown voltage.

References

[1] Chandradass J.; Bae D.S,. *Mater. Manuf. Proces.* **2008**, *23,* 117.
[2] Fang F.; Yang W.; Zhang M.Z.; Wang Z. *Compos. Sci. Technol.* **2009,** 69, 602.
[3] Marra S.P.; Ramesh K.T.; Douglas A.S.; *Compos. Sci. Technol.***1999**, 59, 2163.

The effect of processing conditions on the morphology, thermomechanical, dielectric and piezoelectric properties of P(VDF-TrFE)/$BaTiO_3$ composites

Sara Dalle Vacche[a], Fabiane Oliveira[a], Yves Leterrier[a]*, Véronique Michaud[a],

Dragan Damjanovic[b], Jan-Anders E. Månson[a]

[a] Laboratoire de Technologie des Composites et Polymères (LTC),

Ecole Polytechnique Fédérale de Lausanne (EPFL), CH-1015 Lausanne, Switzerland

[b] Ceramics Laboratory (LC),

Ecole Polytechnique Fédérale de Lausanne (EPFL), CH-1015 Lausanne, Switzerland

(*) Corresponding author: Yves Leterrier, yves.leterrier@epfl.ch

Tel +41 21 693 4848; Fax +41 21 693 5880

ABSTRACT

In this study (0-3) P(VDF-TrFE)/$BaTiO_3$ composites containing up to 60 vol% of ceramic phase were prepared by solvent casting or compression molding. Their thermomechanical, dielectric, and piezoelectric properties were investigated, and discussed in the light of the properties of the basic components, the processing route and the resulting morphology. The crystalline structure of the P(VDF-TrFE) matrix was found to highly dependent on the processing route, while the structure of $BaTiO_3$ was not affected by any of the processing steps. The mechanical properties of the solvent cast materials showed a maximum at 30 vol% $BaTiO_3$, while they increased monotonically with $BaTiO_3$ content for compression molded materials. This difference was attributed to a higher amount of porosity and inhomogeneities in the solvent cast composites. Permittivity as high as 120 and piezoelectric coefficient d_{33} up to 32 pC/N were obtained for compression molded composites, and the observed decrease in d_{33} with aging time was attributed to the effect of mechanical stress release in the polymer matrix.

Keywords: Piezoelectric materials; Polymer composites; Thermomechanical properties; Electrical properties.

1. INTRODUCTION

Composites combining a piezoelectric ceramic phase and a polymer phase, either inactive or piezoelectric, have attracted great interest as they offer a unique combination of properties and design flexibility [1,2]. Piezoelectric and pyroelectric activity, a wide range of dielectric constants and high breakdown strength are combined with mechanical flexibility, formability and low acoustic impedance. Furthermore the properties of piezoelectric composites may be tailored by the judicious choice of the polymeric matrix and ceramic filler, of their volume fraction, and of the type of connectivity, making these materials very attractive for applications as sensors and actuators. Binary piezoelectric composites may have different connectivity patterns, which were classified by Newnham *et al.* [3] and designated by the notation (*m*-*n*), where *m* and *n* indicate the connectivity of each one of the two phases. According to this nomenclature, composites in which piezoelectric ceramic particles are completely surrounded by a three-dimensionally connected polymeric phase have (0-3) connectivity. As (0-3) composites are easier to manufacture and shape than composites with other connectivity patterns, a large research effort is taking place to improve their piezoelectric coefficient. Several polymers have been used as matrices for such composites, including e.g. epoxy resins [4,5], chloroprene [6], polyethylene oxide [7], and polyamides [8,9]. Polyvinylidene fluoride (PVDF) and its copolymer with trifluoroethylene, P(VDF-TrFE), have raised particular interest as they have large relative permittivity and high dielectric strength, and exhibit themselves a relatively large piezoelectric activity. It has been demonstrated for this type of composites that it is possible to polarize independently the polymeric matrix and/or the ceramic inclusions [10-13], therefore adding an additional degree of freedom to the tuning of the composite properties. Lead containing perovskites, and particularly PZT ($Pb(Zr,Ti)O_3$ - lead zirconium titanate), are at present the most widely used

materials for sensors, actuators and other electronic devices due to their excellent piezoelectric properties, ease of fabrication and low cost manufacturing [14]. Hence, most of the studies on piezoelectric ceramic – polymer composites with high piezoelectric activity deal with PZT based materials [15,12,13,7,16,17]. However for environmental and health concerns it is desirable to substitute PZT with a lead free piezoelectric ceramic and $BaTiO_3$ may offer a convenient alternative [18]. Although the piezoelectric coefficient d_{33} of conventional $BaTiO_3$ is lower than that of PZT, a large effort is lately taking place in fabricating high performance $BaTiO_3$ [19]. In addition to this, polymer/$BaTiO_3$ composites are also of great interest for the fabrication of high relative permittivity materials for e.g. embedded capacitors [20-24]. For polymer/$BaTiO_3$ composites the reported absolute values for d_{33} are usually between 1 and 30 pC/N [8,25,26,6] (the sign depending on the polarization conditions in the case of piezoelectric polymer matrices), although a d_{33} higher than 50 pC/N was reported for a PVDF/ $BaTiO_3$ composite [27].

The functionality of these composite materials is mostly due to the dielectric, ferroelectric and piezoelectric properties of the ceramic phase, which often needs to constitute more than 50% in volume. Thus, a challenge is to obtain homogeneous composites with a well dispersed ceramic phase. Furthermore piezoelectric ceramics, e.g. PZT or $BaTiO_3$, are hydrophilic, and dispersion in highly hydrophobic polymers as PVDF and its copolymers may favor their agglomeration. For example, although mechanical powder mixing has been sometimes used [27], most of the PVDF and P(VDF-TrFE) based composites reported in literature were prepared by first dispersing the polymer and ceramics in a solvent. Films were then obtained by solvent casting [28,29], spin coating [30], and/or hot pressing/compression molding under different conditions [26,31]. Annealing was also sometimes used to improve crystallinity of the polymeric matrix [32]. Highly filled (0-3) composites however present a complex

morphology due to the coexistence of several phases: not only the polymer matrix and the ceramic filler particles, but also, at high filler concentrations, filler aggregates and porosities (at microscopic and macroscopic level), as well as residual solvent may be present depending on the processing routes and conditions. As pointed out in a recent review [33], modification of the surface of the ceramic fillers, through chemical grafting or the production of core-shell structures is key to improve filler dispersion, reduce porosity, thereby improving the mechanical and electrical properties of the composites. Most of the existent studies focus on the dielectric [34-43] and electromechanical [4,17,13,7,15,44,25] properties of such composites and relatively few systematic studies on their thermal and mechanical behavior have been published so far. Furthermore the ceramic volume fractions considered are often much lower than those used in most applications [45], studies of highly filled composites mainly being limited to lead-based ferroelectric materials [46,47]. The aim of this work is therefore to study the effect of processing conditions on both the thermomechanical and the dielectric and piezoelectric properties of P(VDF-TrFE)/$BaTiO_3$ composites over a wide range of compositions.

2. EXPERIMENTAL

2.1. Materials and sample preparation

P(VDF-TrFE) (77/23 mol%) in powder form was provided by Solvay Solexis SpA (Italy). Two $BaTiO_3$ powders were used as piezoelectric ceramic fillers. The first one (BT-1) was a commercial powder (Barium titanate (IV), < 2 μm, 99.9 % from Sigma Aldrich, USA). The second one (BT-2) was an in house made $BaTiO_3$ powder, obtained by milling $BaCO_3$ and TiO_2 powders in stoichiometric ratio, performing calcination at 1100°C for 3 h and milling

again until the desired particle size was achieved. Methyl ethyl ketone (MEK) was used as solvent (Acros Organics, 2-butanone, 99+ %).

Solvent cast films were obtained by first dissolving P(VDF-TrFE) in MEK at 60°C in an oil bath on a magnetic stirrer for several minutes, until complete dissolution of the polymer. Then $BaTiO_3$ was added slowly to the stirred solution in order to avoid powder sedimentation or agglomeration. The solution was then placed in an ultrasound bath (Sonorex Super, Bandelin GmbH & Co. KG, Germany) for 1 h to further disagglomerate the powder [26,31]. Finally the solution was cast on glass and the solvent was evaporated at room temperature in vacuum for 12 h, and then at 70°C in vacuum for 2 h. The films obtained in this way were then divided in 3 sets. One set was tested without further treatment, one set was annealed at 135°C for 30 min prior to testing, and one set was used to produce compression molded films. Compression molding was performed in a TP50 hydraulic press (Fontijne Holland, Netherlands). Two layers of solvent cast films were superposed and then pressed with 5 MPa, while heating from 25 to 200°C in 20 min, then holding at 200°C for 10 min, and cooling to 25°C in 20 min. Materials containing 15, 30, 45 and 60 vol% of BT-1 powder, and 60 vol% of BT-2 powder were prepared. A concentration of 60 vol% was the limit for which solvent cast films did not disintegrate upon removal from the glass support and for which it was still possible to obtain a consolidated film by compression molding. Films of P(VDF-TrFE) were also prepared as references following the same procedures. In what follows solvent cast materials are indicated with the code SC-xx-y, solvent cast annealed materials with the code SCA-xx-y, and compression molded materials with the code CM-xx-y, where xx indicates the percent in volume of $BaTiO_3$ and y is equal to 1 or 2 for materials containing BT-1 or BT-2 particles respectively.

2.2. Methods

The particle size of the $BaTiO_3$ powders was measured with a Mastersizer particle size analyzer (Malvern Instruments Ltd., UK), after disagglomerating the particles with an ultrasound horn for 15 min in a solution of polyacrylic acid (PAA) at 0.01 wt% in water and NH_3, with an NH_3/PAA molar ratio of 1.5. X-ray diffraction was performed on the $BaTiO_3$ powders and on the films using CuKα radiation on a D8 Discover diffractometer (Bruker AXS, USA). The morphology of the nanocomposites was observed in a Philips XL30 FEG (Philips, The Netherlands) scanning electron microscope (SEM). The samples were prepared by cryo-fracture and carbon coated to prevent charging.

The thermal properties of the $BaTiO_3$ powders and of the films were studied by means of differential scanning calorimetry (DSC Q100, TA Instruments, USA). The measurements were carried out between -80°C and 200°C at a heating/cooling rate of 10 K/min under N_2 flow. Thermogravimetric analysis (Mettler Toledo TGA/SDTA 851) was performed between 30°C and 800°C at 10 K/min under N_2 flow in alumina crucibles. Dynamic mechanical analysis (Q800 DMA, TA Instruments, USA) was performed on the films in tensile configuration between -50°C and 150°C at a heating rate of 3 K/min. The excitation frequency was 1 Hz and the applied strain was 0.05% in order to stay within the linear viscoelastic region, which was smaller for the composites than for the pure polymer.

Gold electrodes were deposited on the films by sputtering. Capacitance and losses were measured as a function of frequency with an impedance/gain-phase analyzer HP4194A at room temperature between 100 Hz and 1 MHz and with AC voltage of 1 V_{rms}. Relative permittivity was then calculated from capacitance. Poling of the samples was performed in

silicone oil. The desired electric field was applied for 30 min at 110°C and then for further 30 min while cooling to 35°C. The piezoelectric coefficient d_{33} was measured with a Berlincourt-type d_{33}-meter. The first measurement was taken one hour after poling and then further measurements were performed in the following days in order to assess aging.

3. RESULTS AND DISCUSSION

3.1. Powder characterization

BT-1 powder was found to have a mean particle size of 1 μm and BT-2 of 0.7 μm. The XRD patterns of BT-1 and BT-2 reproduced in Figure 1 revealed higher tetragonality for the BT-2 powder as indicated by the better separation of the (200) and (002) peaks, visible between $2\theta = 44°$ and $2\theta = 46.5°$. The DSC measurements (Figure 2) showed for both powders a peak at 129°C upon heating (inset in the figure) and a peak at 120°C upon cooling, that can be attributed to the transition from the tetragonal piezoelectric phase to the cubic paraelectric phase and *vice versa* (Curie temperature, T_c) of $BaTiO_3$. The ΔH of the transition was greater for BT-2 (ΔH = 0.4 J/g) than for BT-1 (ΔH = 0.2 J/g), indicating higher amount of tetragonal phase in the BT-2 powder [48,49].

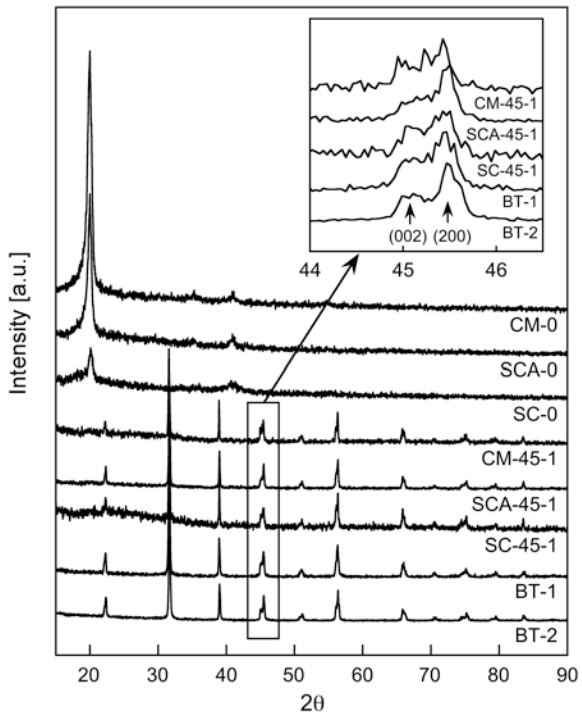

Figure 1. XRD patterns of BT-1 and BT-2 powders, P(VDF-TrFE) and composite films. In the inset is shown the $BaTiO_3$ double peak corresponding to the reflections of (200) and (002) planes.

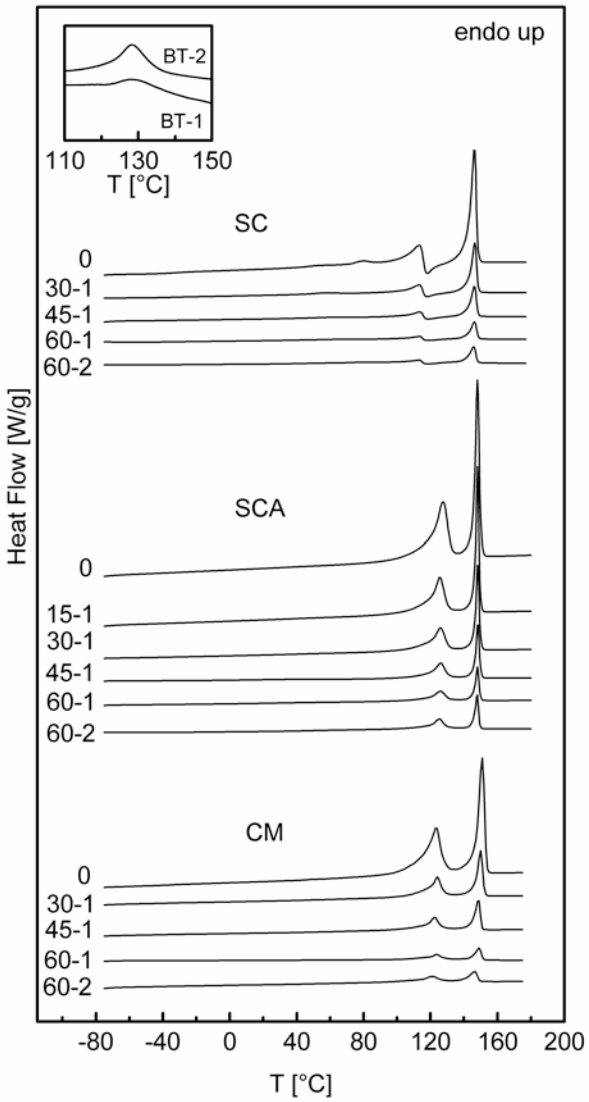

Figure 2. DSC heating thermograms of SC, SCA and CM films, and of BT-1 and BT-2 powders (inset). For legibility the scale of the heat flow of the BT powders is 50:1 with respect to that of the films.

3.2. Structure and morphology of the films

The XRD patterns of the pure P(VDF-TrFE) and composite films are shown in Figure 1. The SC-0 film showed a peak at 2θ = 20° corresponding to the piezoelectric all *trans* crystalline phase of P(VDF-TrFE) and a weak shoulder at lower 2θ attributed to the amorphous phase [50,51]. The shoulder of the amorphous phase disappeared for the SCA-0 and CM-0 films, and the peak at 2θ = 20° became narrower and more intense. This indicates that the SCA-0 and CM-0 films have a better-developed crystalline piezoelectric phase than the SC-0 films.

For all the composite films, the double peak corresponding to the reflections of the (200) and (002) planes of $BaTiO_3$ was equal to that of the pure BT-1 powder, indicating no change in the $BaTiO_3$ structure during processing, as expected since the tetragonal phase is stable at room temperature.

SEM micrographs of cryo-fractured surfaces of the SC and CM films are shown in Figure 3 and Figure 4, respectively. The solvent cast films prepared with BT-1 showed a relatively good through thickness distribution of the $BaTiO_3$ particles; however powder agglomerates and polymer rich areas were visible. The films prepared with BT-2 showed a better dispersion of the $BaTiO_3$ particles, with no polymer rich areas and fewer and smaller aggregates. The compression molding step helped to eliminate the polymer rich areas in the films, therefore obtaining more homogeneous materials. On the other hand, in the samples with higher amounts of ceramics the interface between the superposed layers was still visible in some areas, as highlighted *e.g.* in Figure 4a and 4c.

3.3. Thermal properties

Thermogravimetric analysis was performed on SC and CM materials. The results highlighted that the presence of $BaTiO_3$ increased the thermal stability of both SC and CM materials. The decomposition temperatures are reported in Table 1.

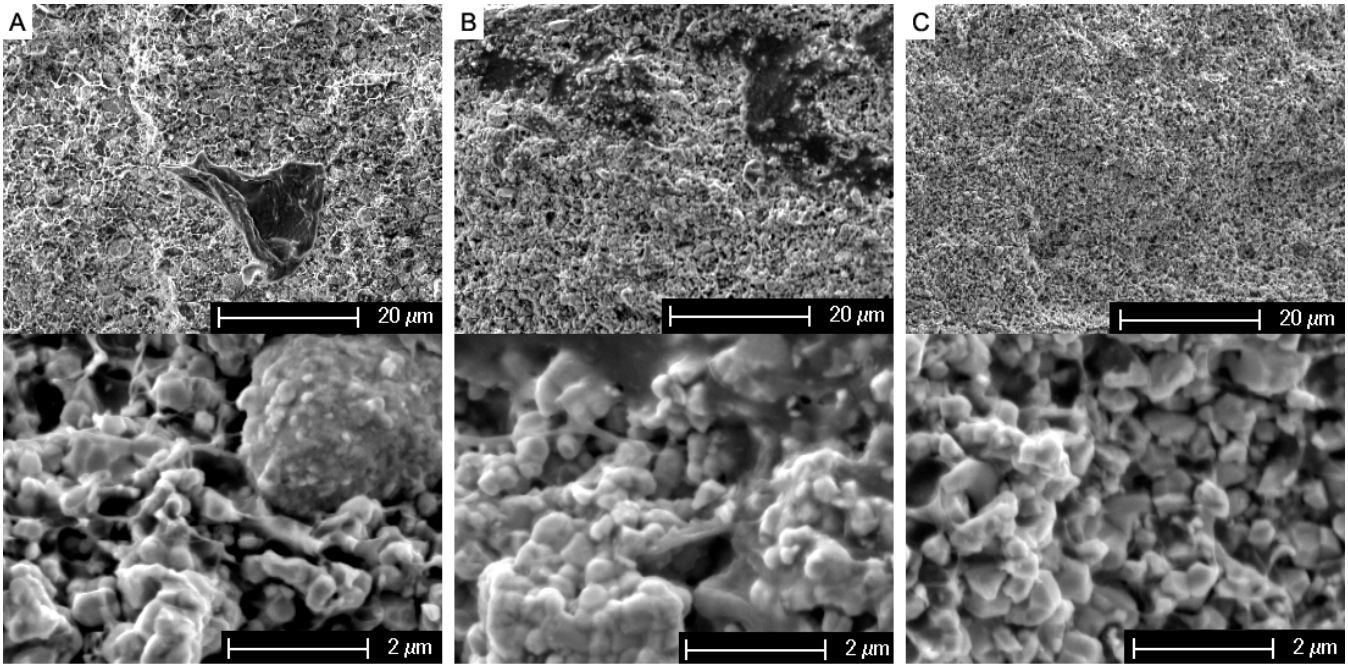

Figure 3. SEM micrographs of (a) SC-30-1 (b) SC-60-1 and (c) SC-60-2.

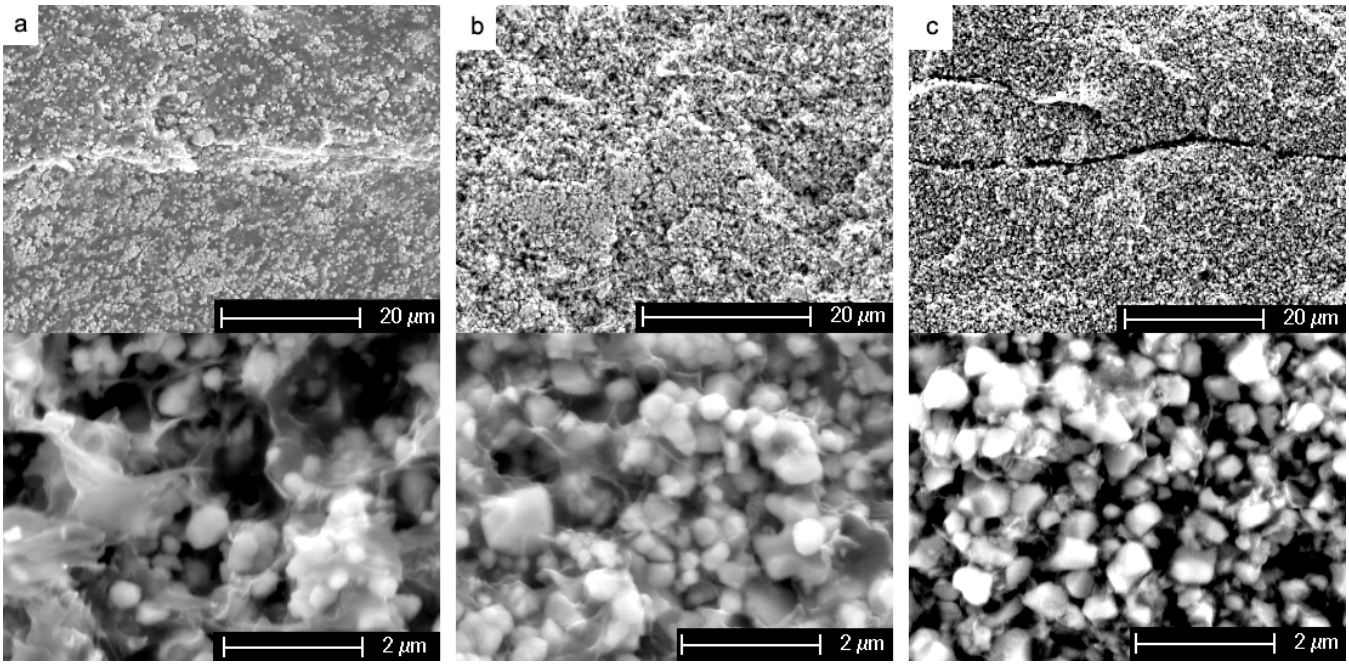

Figure 4. SEM micrographs of (a) CM-30-1 (b) CM-60-1 and (c) CM-60-2.

Table 1 – Decomposition temperatures T_d of SC and CM P(VDF-TrFE) and composites.

BaTiO3		T_d [°C]	
powder	vol%	SC	CM
BT-1	0	482	483
	30	495	496
	60	492	496
BT-2	60	489	490

DSC thermograms of SC, SCA and CM materials are shown in Figure 2. The heating thermograms of the SC films showed an endotherm peak corresponding to the Curie transition, partially overlapping with an exotherm peak attributed to recrystallization of the polymer. This behavior is documented for P(VDF-TrFE) copolymers crystallized at low temperatures [52]. The endotherm peak at 146.3 ± 0.2°C was attributed to melting of the crystalline phase of the polymer. It is clear that the ΔH_f measured for these films is related to their crystallinity after recrystallization. Therefore it is not representative of the amount of crystalline phase present in the as made films. The heat capacity step (ΔC_p) corresponding to the glass transition of the amorphous phase of P(VDF-TrFE) was detected at a temperature T_g = -32°C for SC-0, however T_g could not be detected for the composites due to the lower amount of polymer present in the materials. The heating thermograms of the SCA films showed two endotherm peaks corresponding to the Curie transition at T_c = 126.1 ± 0.7°C and to melting at 148.1 ± 0.1°C respectively. The melting peak was sharper and the ΔH_f slightly higher with respect to what observed for the SC films. This indicates that the annealing step not only allowed the recystallization, to an even slightly higher extent than observed during the DSC heating cycle of the SC films, but also that the crystallites obtained were more perfect and with a narrower size distribution. The heating thermograms of the CM films

showed two endhotherm peaks corresponding to the Curie transition at T_c = 123.1 ± 1.8°C and to melting at 148.5 ± 1.7°C. The melting peak, though, was broader and the ΔH_f was lower than for the SCA materials, indicating that the compression molding step resulted in a broader size distribution of the crystallites and lower crystallinity of the polymer.

In order to assess the effect of the addition of $BaTiO_3$ particles on the crystallinity of the polymer phase, the ΔH_f measured for the composites may be compared to the ΔH_f measured for the pure polymer. Theoretically the ΔH_f measured for the composites should scale proportionally to the P(VDF-TrFE) mass fraction, if the presence of $BaTiO_3$ does not affect the degree of crystallinity. The theoretical ΔH_f for the composites is calculated as:

$$\Delta H_f = \Delta H_f^m \cdot w_P = \Delta H_f^m \cdot \frac{\rho_P \phi_P}{\rho_P \phi_P + \rho_B \phi_B} \qquad \text{(eq. 1)}$$

where w_P indicates the mass fraction of P(VDF-TrFE) in the composites, ϕ_P and ϕ_B the volume fractions of P(VDF-TrFE) and $BaTiO_3$, respectively, and ρ_P and ρ_B their respective densities. The density of P(VDF-TrFE) has been taken equal to 1.9 g/cm^3 [53] and that of $BaTiO_3$ equal to 6.08 g/cm^3 according to the supplier's information. The comparison between the theoretical and experimental values is shown in Figure 5. The ΔH_f of the SC and SCA materials decreased proportionally to the weight fraction of the polymer in the composites, indicating that the presence of the BT did not modify the degree of crystallinity of the P(VDF-TrFE) matrix. Again, it must be remembered that the ΔH_f values reported for the SC films were measured after recrystallization. For the CM materials the decrease was slightly higher than the theoretical one, suggesting that in this case the addition of $BaTiO_3$ particles led to decreased crystallinity of the polymer matrix.

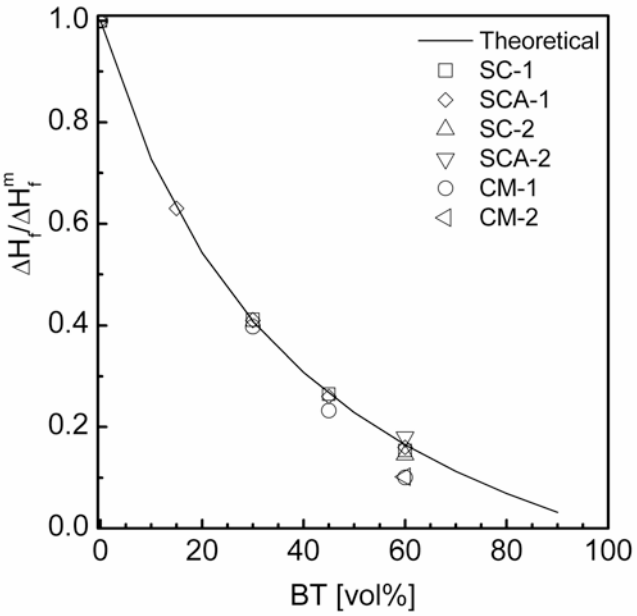

Figure 5. Theoretical and experimental values of the ratio between the heat of fusion of the composites (ΔH_f) and that of the pure polymer (ΔH_f^m)

3.4. Dynamic mechanical analysis

The storage moduli *E'* and ratio of the loss modulus E'' to the storage modulus E' (tan δ) of P(VDF-TrFE) and composite SC films are shown in Figure 6a and b. The modulus of SC-0 showed a marked decrease with temperature until about 100°C. Then it started to increase slightly, before leveling off and finally decreasing again approaching the melting temperature. The modulus increase around 100°C corresponds to the appearance of the exotherm peak in the DSC measurements and supports the hypothesis of a recrystallization. The modulus of SC-30-1 was higher than that of SC-0, and followed the same trends. The composites containing more than 30 vol% of $BaTiO_3$ failed between 100°C and 105°C under the small strain applied. It must be remarked here that if no strain is applied the materials do not fail at these temperatures for the only effect of thermal stress, which allows poling at high temperatures. SC-45-1 and SC-60-1 showed a lower *E'* than SC-30-1 at low temperatures.

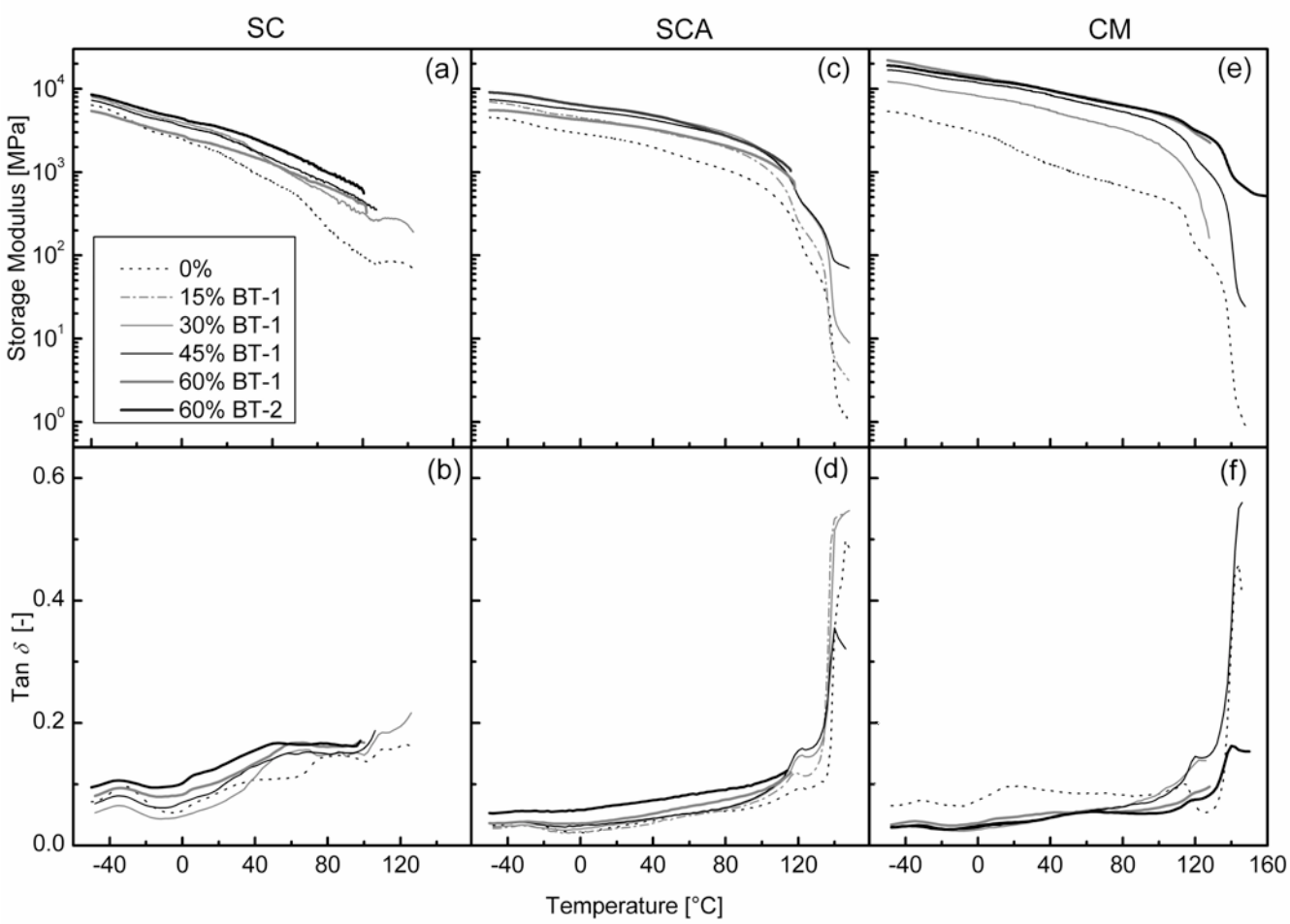

Figure 6 – Storage modulus and tanδ of (a and b) SC films (c and d) SCA films and (e and f) CM films.

The reduction in modulus with increasing filler content may be attributed to the increased inhomogeneity and porosity of the materials with high ceramics volume fraction. However their moduli decreased less steeply with temperature so that above 40-50°C the curves of SC-45-1 and SC-60-1 lied above that of SC-30-1. This may be attributed to the fact that above 40°C the polymer has a very low modulus; therefore the reinforcing effect of the filler has a much higher impact on the final modulus of the composite than at low temperature. SC-60-2 showed the highest modulus among the SC materials. This can be explained in the light of the better dispersion of the BT-2 particles, with smaller aggregates, as shown by the SEM images. The tan δ curves of all the SC materials showed a peak at -33 ± 2°C, corresponding to the segmental motions in the amorphous phase (β-relaxation). A second relaxation process,

named α-relaxation, the nature of which is still debated, appeared above 40°C [54-56]. For the pure P(VDF-TrFE) and for the composite filled with BT-2 the α-relaxation process started at lower temperature than for the composites filled with BT-1. The reason for this difference in temperature is not clearly understood. The tan δ of the materials increased with $BaTiO_3$ volume fraction, with the higher tan δ corresponding to SC-60-2. The only exception was SC-30-1, which had the lowest tan δ at temperatures below 50°C. This is opposite to what is expected upon addition of rigid filler in a polymer matrix and may be attributed to increased porosity in the specimens with higher amounts of $BaTiO_3$ particles.

The storage moduli *E'* and tan δ of SCA films are reported in Figure 6c and d. The storage modulus of the SCA-0 film showed a less marked decrease with temperature than that of the SC-0 film. A first small drop of E' was seen at about -30°C, corresponding to the β-relaxation. A steeper decrease in E' occurred after 110°C, attributable to the Curie transition of the P(VDF-TrFE). Then above 135°C a further drop in modulus was associated with the melting of the polymer. The storage moduli of the SCA composites containing BT-1 particles increased with $BaTiO_3$ concentration up to 30 vol%, and then decreased upon further BT-1 addition, similarly to what observed for SC films. The *E'* curves of SCA-15-1 and SCA-30-1 showed similar behavior to that of SCA-0. The E' of SCA-45-1 and SCA-60-1 on the other hand started at lower values but decreased at a smaller rate with temperature, as already observed for the SC films. The decrease in modulus above 30 vol% $BaTiO_3$ may again be explained by the poorer dispersion of the filler at high concentrations or higher porosity. Around 120°C the E' curve of SCA-45-1 crossed the E' curve of SCA-30-1, in correspondence with the drop in modulus associated with the Curie transition. SCA-60-1 failed at 115°C, temperature at which its modulus had become comparable to that of SCA-30-1. SCA-60-2 showed a modulus about 50% higher than that of SCA-60-1 and comparable

with that of SCA-30-1 up to 115°C, temperature at which SCA-60-2 failed under the applied strain. As for the SC composites the higher modulus of SCA-60-2 compared to the composites filled with BT-1 is attributed to the better dispersion of BT-2 in the polymer matrix. The tan δ curves of all SCA materials showed the peak at -30°C, associated with the β-relaxation, although with reduced intensity compared with the SC materials, in agreement with the DSC results showing higher crystallinity of the P(VDF-TrFE) in the annealed materials. The α-relaxation phenomenon weakly appeared for SCA-0 and was not visible for the SCA composites. A peak was visible at 120°C corresponding to the Curie transition of both P(VDF-TrFE) and $BaTiO_3$, before the sharp increase in tan δ at 140°C corresponding to melting of the polymer. Tan δ increased upon addition of $BaTiO_3$, except for SCA-15-1, which had the lowest tan δ at temperatures below 70°C. The higher tan δ was shown by SCA-60-2, similarly to what was observed for SC films.

The storage modulus E' and tan δ of the CM materials as a function of temperature are shown in Figure 6e and f. The E' of the CM-0 film was found to have at low temperatures a similar value to that of the SCA-0 films. Three drops in modulus were present before the final drop due to melting. The first drop was attributed to the β-relaxation and the drop at 115°C to the Curie transition. The decrease in modulus starting at 5°C may be attributed to the α-relaxation, which was more pronounced than for the SCA materials. The modulus of the composite materials increased with increasing $BaTiO_3$ concentration, but below 135°C this increase leveled off beyond 45 vol% $BaTiO_3$. At all $BaTiO_3$ concentrations the storage modulus E' steadily decreased with temperature between -50°C and 110°C, the drops in E' associated with the β and α relaxations being smaller than for the pure polymer. Then at about 110°C the drop in modulus associated with the Curie transition appeared, the magnitude of which decreased with increasing BT concentration, followed by a less steep decrease up to

about 135°C. Then another drop in E' happened due to melting of the polymer matrix, once again of smaller magnitude for the composites containing higher volume of $BaTiO_3$. The value of tan δ was lower for the composites than for the pure polymer as it would be expected upon addition of a rigid phase. This different behavior than for the SC and SCA materials may be attributed to the reduced inhomogeneities and porosity following the compression molding step. A tan δ peak was present for CM-0 at -30°C, and for the composites between -32°C and -35°C, attributed to the β-relaxation. The α-relaxation peak was visible at about 18°C for CM-0, but was not detected for the composites. The peak attributed to the Curie transition was present for all materials between 115°C and 120°C, before the sharp increase due to melting of the polymer at 140°C.

Lower and upper bounds for the modulus of a two-phase material may be calculated from the volume fractions and moduli of each phase using the Hashin and Shtrikman model [57]. According to this model the lower bounds for the bulk (K^L) and shear (G^L) moduli of a two-phase material are given by:

$$K^L = K_p + \frac{v_c}{\frac{1}{(K_c - K_p)} + \frac{3v_p}{(3K_p + 4G_p)}} \qquad \text{(eq. 2)}$$

$$G^L = G_p + \frac{v_c}{\frac{1}{G_p - G_c} + \frac{6(K_p + 2G_p)v_p}{5G_p(3K_p + 4G_p)}} \qquad \text{(eq. 3)}$$

where K, G and v indicate the bulk modulus, shear modulus and Poisson's coefficient, and the subscripts p and c indicate in our case the polymer and ceramic phase respectively. The upper bounds K^U and G^U are obtained by exchanging the subscripts p and c in the equations above.

The lower (E^L) and upper (E^U) bounds for the Young's modulus may be then be calculated from:

$$E^L = \frac{9K^L G^L}{3K^L + G^L} \quad \text{(eq. 4)}$$

$$E^U = \frac{9K^U G^U}{3K^U + G^U} \quad \text{(eq. 5)}$$

The Hashin and Shtrikman bounds were calculated for the modulus of the SC, SCA and CM materials at 25°C and compared to the experimental values in Figure 7. The Young's moduli of the matrices were taken to be equal to their E' measured by DMA in this work, and the Poisson's ratio was taken equal to 0.3. For the $BaTiO_3$ the Young's modulus was taken equal to 120 GPa and the Poisson's ratio equal to 0.35 [58]. The corresponding values of K and G to be introduced in the equations 2 and 3 were calculated from:

$$K_c = \frac{E_c}{3(1-2\nu_c)} \quad ; \quad K_p = \frac{E_p}{3(1-2\nu_p)} \quad \text{(eq. 6)}$$

$$G_c = \frac{E_c}{2(1+\nu_c)} \quad ; \quad G_p = \frac{E_p}{2(1+\nu_p)} \quad \text{(eq. 7)}$$

For the SC and SCA composites the experimental values of the modulus were coincident with the lower bound up to 30 vol% $BaTiO_3$, and below the lower bound for higher filler fractions. Such behavior is again consistent with a high porosity of these materials at high $BaTiO_3$ volume fractions. For the CM composites the experimental values of the modulus were slightly higher than the lower bound in the whole range of compositions. A similar result was obtained *e.g.* by Tessier-Doyen *et al.* [59] for a vitreous matrix containing spherical alumina particles.

Due to the shape and morphology of the materials, an experimental determination of the porosity was not straightforward. Therefore a rough estimate of the amount of porosity which would cause a decrease in modulus as seen for the SC materials containing more than 45% $BaTiO_3$ has been attempted theoretically. For simplicity it was assumed that all the porosity was in the polymer matrix, and therefore the matrix was considered as a foam, with a modulus that was lower than that of the non porous polymer. Then for the SC-45-1 and SC-60-1 the Hashin and Strickman's model was used to calculate the moduli of the matrix needed to have a lower bound corresponding with the experimental values of the moduli. These calculated matrix moduli were then considered as the moduli of a closed pores foam, for which:

$$\frac{E_f}{E_p} = 0.32\left[\left(1-\phi_v\right)^2 + \left(1-\phi_v\right)\right] \qquad \text{(eq. 8)}$$

where ϕ_v is the volume fraction of pores in the foam. Knowing ϕ_v it was possible to calculate the corresponding volume fraction of pores referred to the whole composite material, which for SC-45-1 and SC-60-1 resulted of 15% and 22% respectively.

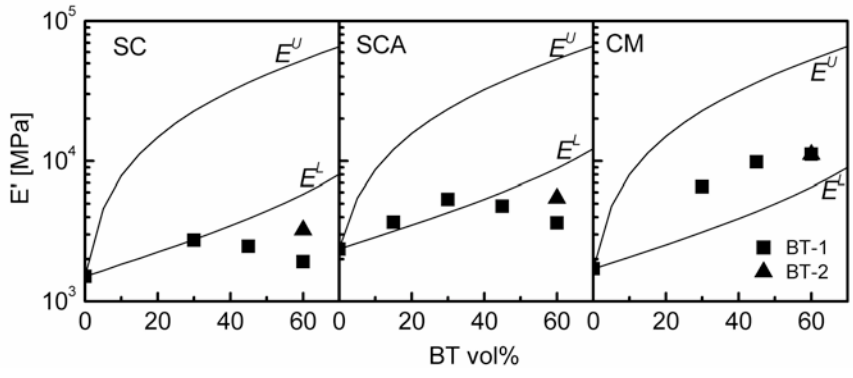

Figure 7. Hashin and Shtrikman bounds and experimental values for the storage modulus of SC, SCA and CM materials at 25°C.

3.5. Dielectric properties

The relative permittivity and losses as a function of frequency of films containing 60 vol% of BT-2 are shown in Figure 8. In the whole range of frequency SC and SCA materials showed a lower permittivity than CM ones. This may be attributed to higher porosity in the SC composites. In fact if we take for the SC-60-1 composite the calculated porosity value of 22%, and assuming that the value of permittivity measured for the CM-60-1 material (124) corresponded to 0% porosity, we can apply the logarithmic rule of mixtures to take porosity into account:

$$\log \varepsilon = \phi_s \log \varepsilon_s + \phi_v \log \varepsilon_v \qquad \text{(eq. 9)}$$

where ε, ε_s and ε_v are the permittivities of the porous composite, of the non porous composite and of the voids and ϕ_s and ϕ_v are the volume fractions of the solid composite phase and of the pores respectively. According to this calculation the permittivity of the non porous SC-60-1 composite would be equal to 63, which is close to the measured value for SC-60-2. As shown in Figure 8 the relative permittivity increased with $BaTiO_3$ content for the CM materials. At all $BaTiO_3$ concentrations the permittivity was nearly constant between 10^2 and 10^4 Hz then it decreased. The losses were low (loss tangent < 0.05) up to 10^4 Hz, then they rapidly increased at higher frequencies. This behavior is characteristic of the β-relaxation of P(VDF-TrFE) [56].

It must be noticed that the permittivity obtained with 60 vol% BT-1 was higher than that obtained with 60 vol% BT-2. This may be attributed to the dependence of the permittivity of $BaTiO_3$ on grain size, the permittivity showing a maximum for 1 μm grain size and decreasing at smaller grain sizes.

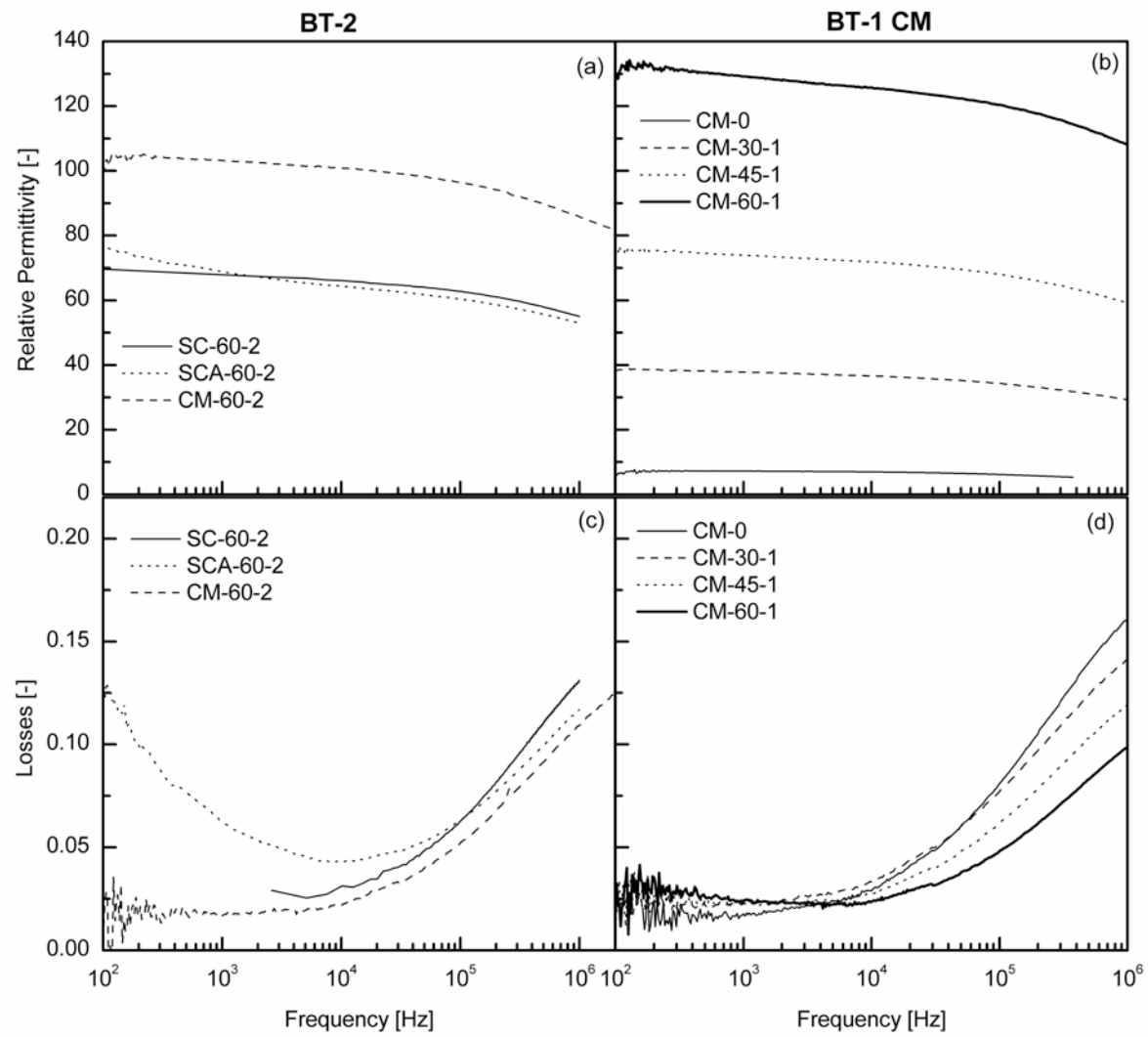

Figure 8. Relative permittivity and loss tangent for (a and c) SC, SCA and CM composites containing 60 vol% BT-2 and (b and d) CM P(VDF-TrFE) and composites filled with BT-1 particles.

A classical model for the relative permittivity as a function of the ceramic volume fraction is the Bruggeman's equation:

$$1-\phi_c = \frac{\varepsilon_c - \varepsilon}{\varepsilon_c - \varepsilon_p}\left(\frac{\varepsilon_p}{\varepsilon}\right)^{\frac{1}{3}} \qquad \text{(eq. 10)}$$

where ϕ_c is the volume fraction of the ceramic and ε_c, ε_p and ε are the relative permittivities of the ceramic, the polymer and the composites respectively. Another model was proposed by

Jayasundere [60], who modified the Kerner's equation [61] in order to take into account the interactions between neighboring dielectric particles:

$$\varepsilon = \frac{\varepsilon_p\phi_p + \varepsilon_c\phi_c\left[3\varepsilon_p/\left(\varepsilon_c+2\varepsilon_p\right)\right]\left[1+\phi_c\left(\varepsilon_c-\varepsilon_p\right)/\left(\varepsilon_c+2\varepsilon_p\right)\right]}{\phi_p + \phi_c\left(3\varepsilon_p\right)/\left(\varepsilon_c+2\varepsilon_p\right)\left[1+\phi_c\left(\varepsilon_c-\varepsilon_p\right)/\left(\varepsilon_c+2\varepsilon_p\right)\right]} \qquad \text{(eq. 11)}$$

The comparison of the experimental results for CM films at 10 kHz with those calculated assuming the permittivity of P(VDF-TrFE) equal to that measured for the pure polymer, and the permittivity of BT equal to 1500 are shown in Figure 9. The agreement between the experimental data and the Jayasundere model was excellent for the entire range of compositions, while the Bruggeman's model slightly underestimated the relative permittivity in the central part of the experimental range of compositions.

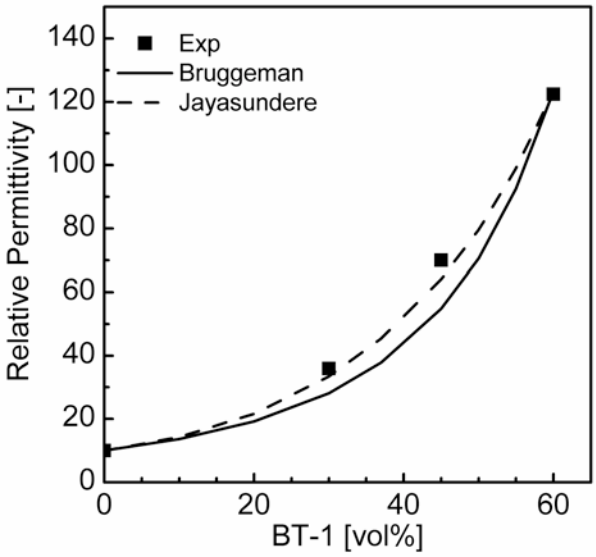

Figure 9. Calculated and experimental values for the relative permittivity of CM materials at 10 kHz as function of $BaTiO_3$ content.

3.6. Piezoelectric coefficient

In order to choose an optimum polarization field, a series of poling experiments with increasing electrical field were conducted on CM-60-2. When the polarization field was increased from 25 kV/cm to 100 kV/cm, the d_{33} increased initially with the applied field, and then started to level off, suggesting that full polarization was approached (see Figure 10). However it was not possible to verify by applying higher electric fields if full polarization was indeed reached, due to breakdown of the materials.

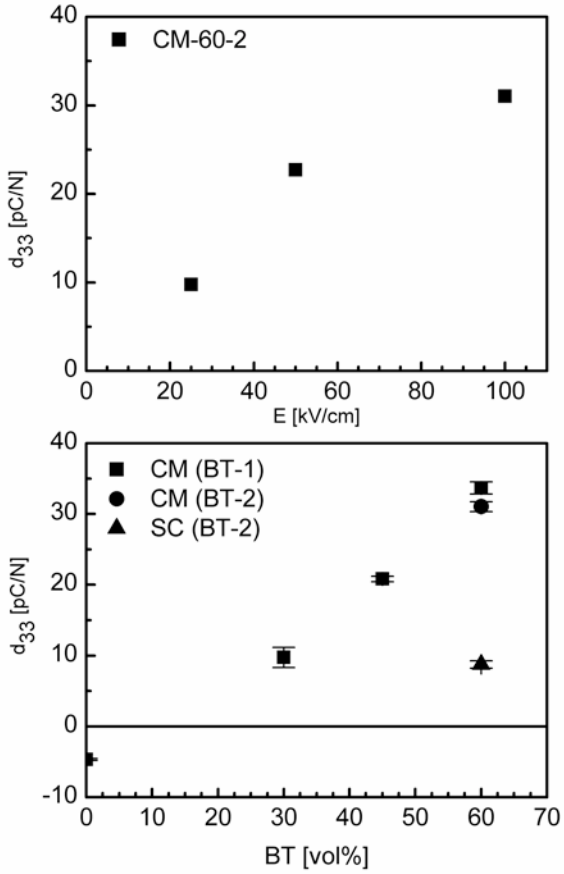

Figure 10. Piezoelectric coefficient of (a) CM-60-2 as a function of poling field and (b) CM and SC materials poled at 100 kV/cm as a function of $BaTiO_3$ content.

As all the materials with lower amounts of $BaTiO_3$ proved to be able to stand the applied field of 100 kV/cm without breakdown, this field was chosen for the study. The d_{33} of the CM materials tested 1 h after poling increased linearly with $BaTiO_3$ vol% from -5 pC/N for the pure polymer up to a value of 34 pC/N for 60 vol% $BaTiO_3$ (Figure 10). The d_{33} obtained for the pure polymer was low compared with the value achievable for this polymer, which is about -30 pC/N, however it must be remembered that such high values are usually obtained with poling fields of the order of 500 to 1000 kV/cm. The absolute value of the d_{33} obtained for the films containing 60% $BaTiO_3$ is comparable with the maximum value obtainable for the pure polymer (although in the opposite direction), but it was achieved applying a much lower poling field. The SC materials showed lower d_{33} than the CM ones. This may be related to the lower permittivity.

3.7. Aging

When d_{33} was measured as a function of time, a strong aging was observed for the composite materials, as highlighted in Figure 11a. The aging rate depended on the type of powder, BT-2 showing less severe aging than BT-1, and on the BT vol%, the aging rate increasing at lower BT concentrations. The aging was almost completely reversible, *i.e.* when an aged sample was poled again the d_{33} obtained was up to 92% of the d_{33} obtained with the first poling. A hypothesis on the cause of aging is stress release in the polymer. In fact during poling the domains of the ceramic phase are oriented in the direction of the field. This rotation creates a mechanical stress in the polymer. In time the polymer chains tend to release this stress and this may cause a partial loss of orientation of the domains ceramic phase. In order to support this hypothesis the permittivity of the samples was measured after poling and with aging time. The relative permittivity of the poled materials measured immediately after poling was lower

than that of the corresponding unpoled materials, as expected, and the piezoelectric resonance peaks appeared in the permittivity patterns (Figure 11b). Then an increase of the relative permittivity was observed for the poled samples with time after poling, which can be attributed to the loss of preferred orientations of some $BaTiO_3$ domains and to the consequent increased density of domain walls. As a consequence the amplitude of the resonance peaks decreased.

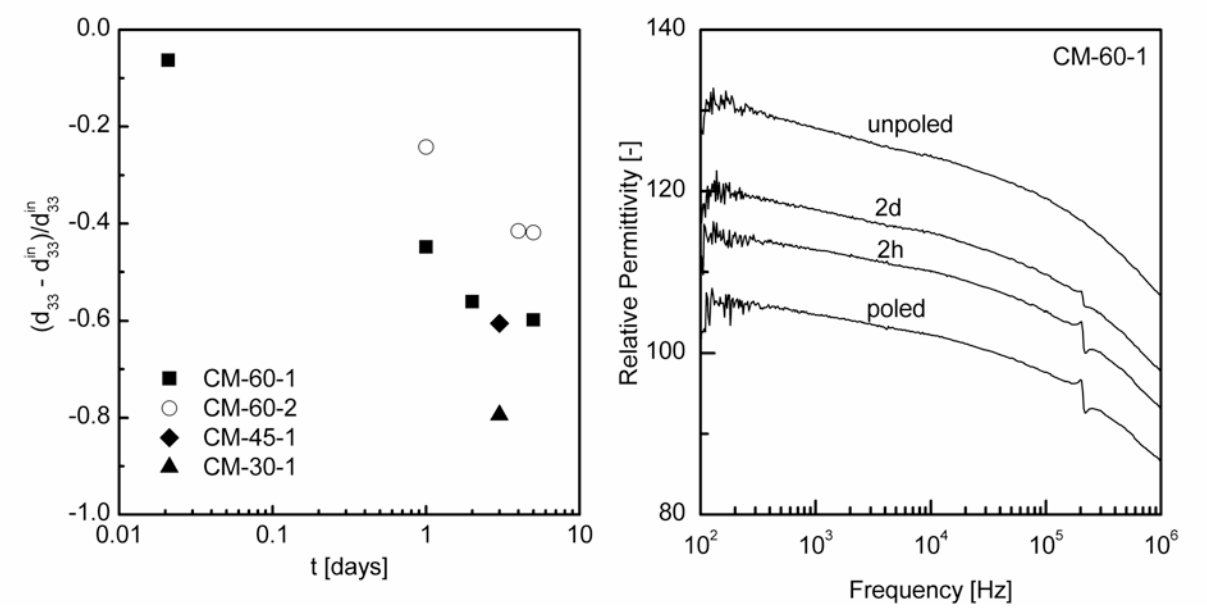

Figure 11. (a) Relative decrease of d33 with aging time and (b) relative permittivity of CM-60-1 unpoled, poled and aged for 2 h (2h) and 2 days (2d) after poling.

3.8. Summary

According to the results of the structural and morphological characterization, the (0-3) $BaTiO_3$/P(VDF-TrFE) composites may be schematized as in Figure 12. The amount of particle aggregates and porosity was found to be dependent on the volume percent and on the type of $BaTiO_3$ powder, with porosity being also highly affected by the processing route. The crystalline structure of the polymeric matrix was mainly influenced by the processing route.

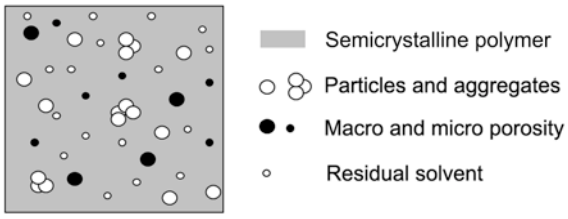

Figure 12. Model of the morphology of highly filled polymer/ceramic composites.

It was also evident from the results reported above that the differences in the dispersion state of the $BaTiO_3$ particles, as well as in the degree of crystallinity of the polymer matrix, depending on the powder characteristics and on the processing route, were reflected in differences in the mechanical, dielectric and piezoelectric properties of the materials. The annealed solvent cast and compression molded P(VDF-TrFE) films showed a better developed crystalline structure than the not annealed solvent cast films, resulting in lower tan δ and higher modulus in the range of temperatures between 0 and 100°C. However for the SCA composite films the inhomogeneity in particle dispersion caused a degradation of the mechanical properties with increasing $BaTiO_3$ content. The dielectric and piezoelectric properties of compression molded films were also superior to those of solvent cast and annealed films. For CM composites the relative permittivity increased according to models and the d_{33} increased linearly with $BaTiO_3$ vol%.

4. CONCLUSIONS

The morphology, structure and properties of (0-3) piezoelectric P(VDF-TrFE)/$BaTiO_3$ composites were found to be highly dependent on the volume fraction of $BaTiO_3$ particles and on the processing route. The compression molding step was found to give the best results for the mechanical, piezoelectric and dielectric properties of highly filled composites when compared to only solvent casting and annealing, with the CM composites containing 60%

$BaTiO_3$ showing a 7-fold increase of the storage modulus, a high permittivity up to 120, and a d_{33} up to 32 pC/N. The improvement in properties due to compression molding was mainly attributed to the reduction of inhomogeneities and porosity. Other methods to improve the compatibility between the hydrophilic $BaTiO_3$ particles and the hydrophobic P(VDF-TrFE) matrix may lead to an improvement in the quality and properties of the solvent cast films. The observed reduction of d_{33} with aging time was found to be reversible, and was attributed to the viscoelastic behavior of the polymer. For practical applications the aging phenomenon will need to be further understood and drastically reduced. Work aiming at addressing these two points is currently ongoing, exploring the effects of the surface modification of the $BaTiO_3$ particles with silanes and the effect of aging on the morphology and structure of P(VDF-TrFE)/$BaTiO_3$ composites.

ACKNOWLEDGMENTS

The authors would like to thank the Swiss Federal Office of Energy (OFEN) and Swiss National Science Foundation (SNF) for funding, Solvay Solexis SpA for kindly providing P(VDF-TrFE) and for fruitful discussion, Li Jin for preparing the in house made $BaTiO_3$ powder and Arthur Aebersold for technical support. The Laboratory of Powder Technology (LTP) and the Interdisciplinary Centre for Electron Microscopy (CIME) at EPFL are also acknowledged for support and access to their equipment.

REFERENCES

1. Dias CJ, Dasgupta DK (1994) Piezoelectricity and pyroelectricity in ferroelectric ceramic-polymer composites. In: Ferroelectric Polymers and Ceramic-Polymer Composites, vol 92-9. Key Engineering Materials. Trans Tech Publications, Clausthal Zellerfe, pp 217-247

2. Akdogan EK, Allahverdi M, Safari A (2005) Piezoelectric composites for sensor and actuator applications. IEEE Trans Ultrason Ferroelectr Freq Control 52 (5):746-775

3. Newnham RE, Skinner DP, Cross LE (1978) Connectivity and piezoelectric-pyroelectric composites. Materials Research Bulletin 13 (5):525-536

4. Han KH, Safari A, Riman RE (1991) Colloidal processing for improved piezoelectric properties of flexible 0-3 ceramic polymer composites. Journal of the American Ceramic Society 74 (7):1699-1702

5. Sa-Gong C, Safari A, Newnham RE Poling study of $PbTiO_3$ polymer composites. In: IEEE Proceedings of the 6th International Symposium on Applications of Ferroelectrics, 1986 1986. pp 281-284. doi:10.1109/ISAF.1986.201142

6. Yamamoto T, Urabe K, Banno H (1993) BaTiO3 particle-size dependence of ferroelectricity in BaTiO3 polymer composites. Japanese Journal of Applied Physics 32:4272-4276

7. Chau KH, Wong YW, Shin FG (2007) Enhancement of piezoelectric and pyroelectric properties of composite films using polymer electrolyte matrix. Applied Physics Letters 91 (25):3. doi:10.1063/1.2827571

8. Capsal JF, Dantras E, Dandurand J, Lacabanne C (2006) Electroactive influence of ferroelectric nanofillers on polyamide 11 matrix properties. Journal of Non-Crystalline Solids 353:4437-4442. doi:10.1016/j.jnoncrysol.2007.01.097

9. Petchsuk A, Supmak W, Thanaboonsombut A (2009) A series of 0-3 composites of lead zirconate titanate and ferroelectric nylon 77: preparation and electrical properties. Journal of Applied Polymer Science 114 (2):1048-1054. doi:10.1002/app.30636

10. Ploss B, Ng W-Y, Chan HL-W, Ploss B, Choy C-L (2001) Poling study of PZT/P(VDF-TrFE) composites. Composites Science and Technology 61 (7):957-962

11. Ploss B, Shin FG, Chan HLW, Choy CL (2000) Pyroelectric activity of ferroelectric PT/PVDF-TRFE. IEEE Transactions on Dielectrics and Electrical Insulation 7 (4):517-522

12. Chan HLW, Ng PKL, Choy CL (1999) Effect of poling procedure on the properties of lead zirconate titanate vinylidene fluoride-trifluoroethylene composites. Applied Physics Letters 74 (20):3029-3031

13. Zeng R, Kwok KW, Chan HLW, Choy CL (2002) Longitudinal and transverse piezoelectric coefficients of lead zirconate titanate/vinylidene fluoride-trifluoroethylene composites with different polarization states. Journal of Applied Physics 92 (5):2674-2679. doi:10.1063/1.1497699

14. Helke G, Lubitz K (2008) Piezoelectric PZT Ceramics. In: Heywang W, Lubitz K, Wersing W (eds) Piezoelectricity. Evolution and Future of a Technology. Springer Series in Materials Science, vol 114. Springer, Berlin Heidelberg, pp 89-130

15. Chen XD, Yang DB, Jiang YD, Wu ZM, Li D, Gou FJ, Yang JD (1998) 0-3 Piezoelectric composite film with high d(33) coefficient. Sensors and Actuators a-Physical 65 (2-3):194-196

16. Yao JL, Xiong CX, Dong LJ, Chen C, Lei YA, Chen L, Li R, Zhu QM, Liu XF (2009) Enhancement of dielectric constant and piezoelectric coefficient of ceramic-polymer composites by interface chelation. Journal of Materials Chemistry 19 (18):2817-2821. doi:10.1039/b819910h

17. Kerimov MK, Kurbanov MA, Musaeva SN, Geidarov GM, Aliev GG (2009) New technology of polymer-piezoceramic composites with high piezoelectric and electromechanical properties. Technical Physics Letters 35 (2):166-169. doi:10.1134/s1063785009020205

18. Panda PK (2009) Review: environmental friendly lead-free piezoelectric materials. Journal of Materials Science 44 (19):5049-5062. doi:10.1007/s10853-009-3643-0

19. Karaki T, Yan K, Miyamoto T, Adachi M (2007) Lead-free piezoelectric ceramics with large dielectric and piezoelectric constants manufactured from BaTiO3 nano-powder. Japanese Journal of Applied Physics Part 2-Letters & Express Letters 46 (4-7):L97-L98. doi:10.1143/jjap.46.l97

20. Xu JW, Moon KS, Pramanik P, Bhattacharya S, Wong CP (2007) Optimization of epoxy-barium titanate nanocomposites for high performance embedded capacitor components. IEEE Trans Compon Packaging Technol 30 (2):248-253. doi:10.1109/tcapt.2007.898352

21. Dang ZM, Wang HY, Xu HP (2006) Influence of silane coupling agent on morphology and dielectric property in BaTiO3/polyvinylidene fluoride composites. Applied Physics Letters 89 (11):3. doi:112902 10.1063/1.2338529

22. Dang ZM, Xu HP, Wang HY (2007) Significantly enhanced low-frequency dielectric permittivity in the BaTiO3/poly(vinylidene fluoride) nanocomposite. Applied Physics Letters 90 (1):3. doi:012901 10.1063/1.2393150

23. Dang Z-M, Yu Y-F, Xu H-P, Bai J (2008) Study on microstructure and dielectric property of the BaTiO3/epoxy resin composites. Composites Science and Technology 68 (1):171-177

24. Kim P, Doss NM, Tillotson JP, Hotchkiss PJ, Pan MJ, Marder SR, Li JY, Calame JP, Perry JW (2009) High energy density nanocomposites based on surface-modified BaTiO3 and a ferroelectric polymer. ACS Nano 3 (9):2581-2592. doi:10.1021/nn9006412

25. Luo XT, Chen LF, Chen XJ, Huang QJ (2004) Preparation and electromechanical properties of PVDF matrix piezo-electric composites containing highly oriented BaTiO3 whiskers. Journal of Materials Science & Technology 20 (4):441-444

26. Chan HLW, Cheung MC, Choy CL (1999) Study on BaTiO3/P(VDF-TrFE) 0-3 composites. Ferroelectrics 224 (1-4):541-548

27. Patil R, Ashwin A, Radhakrishnan S (2007) Novel polyaniline/PVDF/BaTiO3 hybrid composites with high piezo-sensitivity. Sensors and Actuators a-Physical 138 (2):361-365. doi:10.1016/j.sna.2007.05.025

28. Muralidhar C, Pillai PKC (1986) Pyroelectric behavior in barium-titanate polyvinylidene fluoride composites. IEEE Transactions on Electrical Insulation 21 (3):501-504

29. Venkatragavaraj E, Satish B, Vinod PR, Vijaya MS (2001) Piezoelectric properties of ferroelectric PZT-polymer composites. Journal of Physics D-Applied Physics 34 (4):487-492

30. Dietze M, Krause J, Solterbeck CH, Es-Souni M (2007) Thick film polymer-ceramic composites for pyroelectric applications. Journal of Applied Physics 101 (5). doi:10.1063/1.2653978

31. Mao YP, Mao SY, Ye ZG, Xie ZX, Zheng LS (2010) Size-dependences of the dielectric and ferroelectric properties of BaTiO3/polyvinylidene fluoride nanocomposites. Journal of Applied Physics 108 (1). doi:10.1063/1.3443582

32. Lam KH, Wang XX, Chan HLW (2005) Piezoelectric and pyroelectric properties of (Bi0.5Na0.5)(0.94)Ba0.06TiO3/P(VDF-TrFE) 0-3 composites. Composites Part A: Applied Science and Manufacturing 36 (11):1595-1599. doi:10.1016/j.compositesa.2005.03.007

33. Dang ZM, Yuan JK, Zha JW, Zhou T, Li ST, Hu GH (2012) Fundamentals, processes and applications of high-permittivity polymer–matrix composites. Progress in Materials Science 57 (4):660-723

34. Chanmal CV, Jog JP (2008) Dielectric relaxations in PVDF/BaTiO3 nanocomposites. Express Polymer Letters 2 (4):294-301. doi:10.3144/expresspolymlett.2008.35

35. Cheung MC, Chan HLW, Choy CL (2001) Dielectric relaxation in barium titanate/polyvinylidene fluoride-trifluoroethylene composites. Ferroelectrics 264 (1-4):1721-1726

36. Dang ZM, Zheng Y, Xu HP (2008) Effect of the Ceramic Particle Size on the Microstructure and Dielectric Properties of Barium Titanate/Polystyrene Composites. Journal of Applied Polymer Science 110 (6):3473-3479. doi:10.1002/app.28856

37. Gregorio R, Cestari M, Bernardino FE (1996) Dielectric behaviour of thin films of beta-PVDF/PZT and beta-PVDF/BaTiO3 composites. Journal of Materials Science 31 (11):2925-2930

38. Iijima M, Sato N, Wuled Lenggoro I, Kamiya H (2009) Surface modification of BaTiO3 particles by silane coupling agents in different solvents and their effect on dielectric properties of BaTiO3/epoxy composites. Colloids and Surfaces A: Physicochemical and Engineering Aspects 352 (1-3):88-93

39. Muralidhar C, Pillai PKC (1989) Matrix filler interactions and its influence on barium-titanate (BaTiO3)/polyvinylidene fluoride (PVDF) composite. Ferroelectrics 89:17-26

40. Muralidhar C, Pillai PKC (1987) Dielectric behavior of barium-titanate (BaTiO3) polyvinylidene fluoride (PVDF) composite. Journal of Materials Science Letters 6 (3):346-348

41. Patsidis A, Psarras GC (2008) Dielectric behaviour and functionality of polymer matrix - ceramic BaTiO3 composites. Express Polymer Letters 2 (10):718-726. doi:10.3144/expresspolymlett.2008.85

42. Ramajo L, Castro MS, Reboredo MM (2007) Effect of silane as coupling agent on the dielectric properties of BaTiO3-epoxy composites. Composites Part A: Applied Science and Manufacturing 38 (8):1852-1859

43. Ramajo L, Reboredo M, Castro M (2005) Dielectric response and relaxation phenomena in composites of epoxy resin with BaTiO3 particles. Composites Part A: Applied Science and Manufacturing 36 (9):1267-1274. doi:10.1016/j.compositesa.2005.01.026

44. Kar-Gupta R, Venkatesh TA (2008) Electromechanical response of piezoelectric composites: Effects of geometric connectivity and grain size. Acta Materialia 56 (15):3810-3823

45. Chandradass J, Bae DS (2008) Preparation and properties of barium titanate nanopowder/epoxy composites. Materials and Manufacturing Processes 23 (2):117-123. doi:10.1080/10426910701774320

46. Marra SP, Ramesh KT, Douglas AS (1999) The mechanical properties of lead-titanate/polymer 0-3 composites. Composites Science and Technology 59 (14):2163-2173

47. Marra SP, Ramesh KT, Douglas AS (1999) The mechanical and electromechanical properties of calcium-modified lead titanate/poly(vinylidene fluoride-trifluoroethylene) 0-3 composites. Smart Materials & Structures 8 (1):57-63

48. Dutta PK, Asiaie R, Akbar SA, Zhu W (1994) Hydrothermal Synthesis and Dielectric Properties of Tetragonal BaTiO3. Chemistry of Materials 6 (9):1542-1548. doi:10.1021/cm00045a011

49. Baeten F, Derks B, Coppens W, van Kleef E (2006) Barium titanate characterization by differential scanning calorimetry. Journal of the European Ceramic Society 26 (4-5):589-592

50. Lovinger AJ, Furukawa T, Davis GT, Broadhurst MG (1983) Crystallographic changes characterizing the Curie transition in three ferroelectric copolymers of vinylidene fluoride and trifluoroethylene: 1. As-crystallized samples. Polymer 24 (10):1225-1232

51. Kodama H, Takahashi Y, Furukawa T (1997) Effects of annealing on the structure and switching characteristics of VDF/TrFE copolymers. Ferroelectrics 203 (1):433 - 455

52. Gregorio RJ, Botta MM (1998) Effect of crystallization temperature on the phase transitions of P(VDF/TrFE) copolymers. Journal of Polymer Science Part B: Polymer Physics 36 (3):403-414

53. Simoes R, Rodriguez-Perez M, De Saja J, Constantino C (2009) Tailoring the structural properties of PVDF and P(VDF-TrFE) by using natural polymers as additives. Polymer Engineering & Science 49 (11):2150-2157. doi:10.1002/pen.21455

54. Yagi T, Tatemoto M, Sako J (1980) Transition behavior and dielectric-properties in trifluoroethylene and vinylidene fluoride co-polymers. Polymer Journal 12 (4):209-223

55. Sencadas V, Lanceros-Méndez S, Mano JF (2006) Thermal characterization of a vinylidene fluoride-trifluorethylene (75-25) (%mol) copolymer film. Journal of Non-Crystalline Solids 352 (50-51):5376-5381

56. Zhang SH, Klein RJ, Ren KL, Chu BJ, Zhang X, Runt J, Zhang QM (2006) Normal ferroelectric to ferroelectric relaxor conversion in fluorinated polymers and the relaxor dynamics. Journal of Materials Science 41 (1):271-280. doi:10.1007/s10853-006-6081-2

57. Hashin Z, Shtrikman S (1963) A variational approach to the theory of the elastic behaviour of multiphase materials. Journal of the Mechanics and Physics of Solids 11 (2):127-140

58. Dent AC, Bowen CR, Stevens R, Cain MG, Stewart M (2007) Effective elastic properties for unpoled barium titanate. Journal of the European Ceramic Society 27 (13-15):3739-3743. doi:10.1016/j.jeurceramsoc.2007.02.031

59. Tessier-Doyen N, Glandus JC, Huger M (2007) Experimental and numerical study of elastic behavior of heterogeneous model materials with spherical inclusions. Journal of Materials Science 42 (14):5826-5834. doi:10.1007/s10853-006-1386-8

60. Jayasundere N, Smith BV (1993) Dielectric-constant for binary piezoelectric 0-3 composites. Journal of Applied Physics 73 (5):2462-2466

61. Kerner EH (1956) The Electrical Conductivity of Composite Media. Proceedings of the Physical Society Section B 69 (8):802

Motion Planning & Collision Avoidance within the mc3 Project

Martin Ruffli, ASL-ETH

February 6, 2012

1 Introduction

Within the framework of the mc3 project, lightweight robotic platforms are envisioned to safely navigate through cluttered, dynamic, unstructured inner-city as well as structured highway environments. Our contribution lies in a navigation approach, which performs motion planning and collision avoidance during regular vehicle operation, i.e. well within the limits of stable wheel traction. On the motion planning side, this calls for collision-aware systems, which respect vehicle and environmental constraints and which are able to plan and perform highly complex maneuvers in constrained areas. In order to guarantee responsive vehicle behavior in dynamic environments, the time spent computing such maneuvers needs to be low.

Navigation approaches are usually classified into global and local methods: *Local approaches*, which perform short-term reasoning by considering the local vicinity of an environment only, have traditionally been employed to enforce fast and safe planning in presence of unmapped and moving obstacles. They often incorporate a (dynamic) model of the robotic platform, which is then used to generate inherently executable commands. The main issue with these approaches lies in a susceptibility to local minima (such as dead ends), which are due to the limited planning horizon. This may be overcome by merging the local with a global planning approach.

Global planner construct a motion from the robot's current position all the way to its desired goal (or vice versa), potentially kilometers away. Approaches, which provide solution optimality guarantees (based on i.e. shortest path or time measures) tend to be far from real-time capable. Other approaches compromise in different areas to achieve real-time planning and re-planning capability (i.e. deterministic low-dimensional search [1], randomized search [2]). Thus, despite the large body of existing work on long-range navigation, real-time global planning in high dimensional spaces (required for smooth and safe navigation) remains very challenging.

It is therefore not surprising that navigation systems are usually still equipped with a local planner complementing the global one, guaranteeing smooth local behavior while biasing movement based on the global plan. Within the mc3 project, we adopt this approach of hierarchical decomposition: a global (waypoint based) navigation module will provide rough intermediate goals, whereas a local collision avoidance module will be used to enforce local motion feasibility and safety.

This final deliverable presents the status of the motion planning and collision avoidance module at the end of the project and extends on the intermediate deliverable from October 2010. The remainder of this report is organized as follows: in Section 2 we review state-of-the-art local motion planning approaches and then continue to describe our own

implementation in Section 3. We report on experiments conducted in Section 4. Finally, we draw conclusions and sketch future work (Section 5).

2 Collision Avoidance: A Short Review

The problem of planning shortest paths has obtained significant attention in the theoretic motion planning literature. With the advent of physical robots, applied real-time capable solutions needed to be devised, however.

One of the earliest and simplest collision avoidance approaches, the bug algorithm (described in [3]) follows static obstacles (identified via instantaneous sensor readings only) until a direct path towards the goal becomes feasible. One of this method's main shortcomings lies in the lack of maintaining a history of sensor readings, which prevents it from generating a local map. Such a map would allow to select better instantaneous decisions, however.

The Vector Field Histogram method by Borenstein *et al.* (VFH, see [4]) and its variants (VFH+ [5], VFH* [6] and similarly, although more recently, the Nearness Diagram [7]) address this concern by employing an occupancy grid representation to model the robot's vicinity. All of these methods transform the occupancy information into a polar histogram describing free space around the robot. Among unoccupied slots, a preferable motion direction is chosen according to goal direction and current robot orientation. A velocity is then computed which moves the robot into the chosen direction. One of the issues related to VFH (which was later on treated in its extensions) arises due to the presence of kinematic and dynamic vehicle constraints: VFH does not guarantee that a selected velocity is actually attainable.

A solution to this problem is offered by the Dynamic Window Approach (DWA) [8]. In this method, motion segments are assumed to be composed of piecewise circular arcs. Velocities can thus be described by (v, w)-values in a two-dimensional velocity space. Kinematic constraints are respected by employing a vehicle model and by restricting subsequent velocities to lie within a rectangular window of the current ones. Velocity values which will result in a collision with a static obstacle in the future are pruned. A (v, w) pair is then selected among the feasible velocities, which optimizes a objective function including heading difference to the goal, forward speed, and distance to obstacles.

Soon thereafter, Fiorini *et al.* introduced the concept of Velocity Obstacles (VO) [9], a method that also operates in velocity space but in its basic form assumes a holonomic vehicle platform. Their method allows to treat dynamic obstacles in a principled manner: moving objects are geometrically mapped into the robot's velocity space according to their current position and speed. The method then computes a collision-free motion by assuming that dynamic obstacles proceed on a linearly extrapolated profile. Similarly to DWA, a window in velocity-space constrains the change in velocity from one planning step to the next. This approximates adherence to kinematic and dynamic vehicle constraints. Extensions to VO include a change to non-linear velocity obstacles, where other obstacles' motion can assume any trajectory (although robot-robot interaction is still not considered) [10], and the introduction of reciprocal velocity obstacles, which assume that all agents have the same obstacle avoidance algorithm implemented. The task of collision avoidance is then distributed in part to each participating agent [11].

3 Our Approach to Motion Planning & Collision Avoidance

Contrary to the methods reviewed in Sec. 2, we believe that there is much more to be learnt from the environment than a simple snapshot of the current scene could possibly offer. In fact, we may make use of recently developed methods that identify and then predict the future states of dynamic objects based on current and past observations (see [12]). Particularly, we may be able to produce better motions by optimizing a cost function all the way to the goal rather than over a single time-step only. But as Planning time is typically exponential in the number of time-steps considered, finding a global solution becomes intractable for long planning horizons T_p. Due to the recent work of Kushleyev *et al.* [13] it suffices to consider small T_p, however: they introduce the horizon time $T_h = T_{\text{cur}} + \Delta_t$ (with T_{cur} the current time) after which the certainty of predicted motions of nearby dynamic objects decreases below a certain threshold. For time steps larger than T_h, dynamic objects can thus safely be neglected in the planning query, as little to no additional knowledge can be further extracted. Search may then be reduced to a much lower-dimensional representation, such as a 2D grid which only grows with the square of the environment's size.

3.1 Overview

Our motion planning and collision avoidance module is designed for a robotic vehicle's autonomous operation during regular driving conditions, i.e. well within the limits of stable wheel traction. It consists of several parts, which will be described in the Sec. 3.3 - 3.8. Interfacing to and from other modules (within and outside of the mc3 project) is specified in Sec. 3.2.

In a nutshell, our approach receives motion targets, so-called waypoints, from a global navigation system. Optionally, a (partial) global map including a localization estimate may be provided. In case a global map is available, we compute on it a 2D Dijkstra [14] search from the next waypoint outward. This is used as a heuristic for the local high-dimensional planner. From the robot's proprioceptive sensors a local map is built. Dynamic obstacles are identified and tracked via the approach developed by Ess *et al.* [15] (camera-based, external to mc3) and their future motion is predicted. This information is stored in a risk map. The local planner then expands a tree of feasible, model based, edges out to a predefined horizon (which is a function of motion prediction fidelity or hardware constraints). A minimum-cost edge sequence is determined via an appropriate cost function. The module then sends commands to the vehicle velocity controller according to the first edge of the solution, and the loop starts anew. In the event of an emergency situation arising (e.g. driving conditions do not fall inside the well-behaved limits required by our model-based approach anymore), control is given to the emergency collision avoidance module developed by S. Pleines (IDSC-ETH part of the mc3 project).

3.2 Interfaces

The outbound part of this module's interface provides the low-level control to the robot (not part of mc3) in the form of model-based velocity commands. The other part (inbound) receives high-level motion commands via GPS waypoint coordinates or direct user input (not part of mc3). A map of the environment is assumed to be available. In the case of an emergency situation arising, control is handed to the emergency collision avoidance module developed by S. Pleines at IDSC.

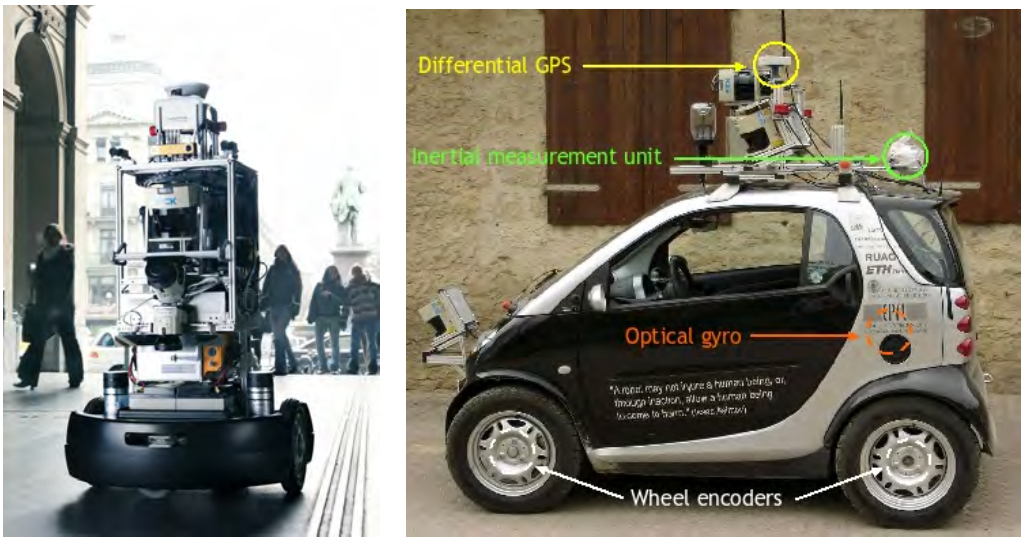

Figure 1: *Left,* differential-drive demonstrator. *Right,* robotic car envisioned to run our system in the future.

3.3 Robotic System Model

In this section we describe the mathematical modeling of the robot. In absence of a real car, we selected a differential-drive tourguide robot as our demonstrator. For control and planning purposes, it is important to model the capabilities of the robotic platform accurately, as the fidelity of the planning solution directly depends on the feasibility of its underlying motion segments.

To this end we employ a simplified dynamic vehicle model: purely kinematic differential-drive models have been successfully employed in many static, low velocity applications. In dynamically changing environments, however, it becomes desirable to more accurately model the dynamic capabilities of the robotic platform (i.e. for safety maneuvers, or for smoother navigation performance). We account for this by adding an integrator in front of the kinematic model inputs. Assuming piecewise constant accelerations at the left and right wheel (a_l, a_r), respectively, the corresponding velocities integrate to

$$v_l(t) = a_l t + v_{l0} \quad , \quad v_r(t) = a_r t + v_{r0}. \tag{1}$$

Forward speed and rotational velocity of the platform are then computed as

$$v(t) = \tfrac{v_r(t)+v_l(t)}{2} \quad , \quad \omega(t) = \tfrac{v_r(t)-v_l(t)}{l}, \tag{2}$$

from which a closed form solution for heading can be derived:

$$\theta(t) = \int \omega(t)dt = \tfrac{(a_r-a_l)t^2}{2l} + \tfrac{(v_{r0}-v_{l0})t}{l} + \theta_0 \tag{3}$$

Due to Fresnel integrals appearing in Eqn. 4, no such solution is known for the position (x, y).

$$\begin{array}{rcl} x(t) & = & \int v(t) \cdot \cos(\theta(t))dt \\ y(t) & = & \int v(t) \cdot \sin(\theta(t))dt \end{array} \tag{4}$$

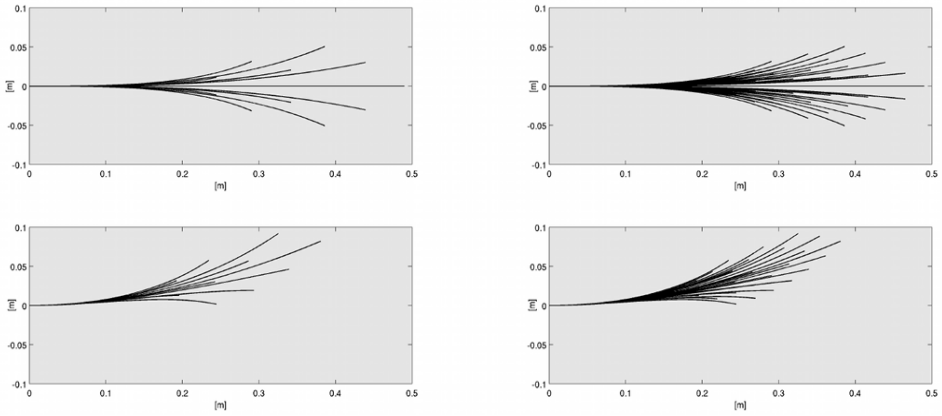

Figure 2: *Left,* 32-directional approx. lattice, shown for two initial curvatures. *Right,* 64-directional approx. lattice, displayed for the same initial conditions.

3.4 Construction of Motion Segments

In the context of the mc3 project we designed an approximately input-sampled lattice, i.e. a repetitive graph structure), by first constructing a 4D lattice manifold in the 6D (2D position, heading, 2D velocity, time) state-space using the robotic system model described above, and then applying an approximation to attach the remaining two dimensions onto a grid. The simplest feasible inputs to System 1-4 take the form of piecewise constant accelerations. Under the weak imposition that these acceleration levels only assume values at integer multiples of an underlying discretization a_s, we propose an algorithm which generates input-sampled lattices in a 4D heading-curvature-velocity-time manifold of the 6D state-space. The resulting edges exhibit several desirable characteristics, including C^2 continuity and equal execution time. The algorithm proceeds as follows:

1. Select a desired sampling time T_s in accordance with vehicle dynamic response. For the special case of $T_s = 1.0$, the parameter t disappears in Eqn. 3.

2. Select the desired number of headings in accordance with environmental constraints. Heading levels become equally distributed over $[0, 2\pi]$ in state-space. By this choice, a discretization on the acceleration a_s is imposed (via Eqn. 1&2).

Through the application of the algorithm, a discrete manifold spanning time t, forward velocity v, rotational velocity ω, and heading θ emerges. (x, y) remain continuous, as Eqn. 4 is not integrable in closed form.

The graph created by the above method assumes continuous values in the (x, y) dimensions. Methods to obtain an approximate discretization exist, however. Towards this end we first *select* a 2D grid discretization in agreement with the graph's minimal edge length and deform all edges to shift segments' end position to the closest (x, y) discretization level. We employ a (x, y) discretization of 0.05 m for 64-directional lattices and 0.1 m for 32-directional ones, as displayed in Fig. 2.

3.5 Dynamic Obstacle Motion Prediction

Motion prediction is a result of object detection, tracking and extrapolation. The tracking sub-part relies on a dynamic model to predict the object's location from its past trajectory.

In crowded scenarios an accurate dynamic motion model is particularly important, as more accurate predictions allow for smaller search regions, which greatly simplifies data association. For this purpose, Ess *et al.* [15] introduced a model of dynamic social behavior, inspired by models developed for crowd simulation. The model is trained with videos recorded from birds-eye view at busy locations, and applied as a motion model for multi-people tracking from a vehicle-mounted camera.

For our purpose, the output of this approach, a deterministic (or stochastic) 3D risk map, is of relevance: it encodes the model-based probability that a given position in (x, y) space will be occupied at a certain time in the (near) future. The collision avoidance module may then make use of this knowledge and compute save motions in spite the presence of dynamic obstacles.

3.6 Safety Considerations

Safety considerations are of highest importance, as our platform is expected to navigate in densely populated human environments. We adopt two well established safety norms, *Passive Safety*, and *Passive Friendly Safety*, as defined below (both compiled from [16]):

Definition 1 (Passive Safety): a state s is safe under Passive Safety (or p-safe) iff there exists at least one braking maneuver starting at s that is collision-free until T_b, with T_b the time where the robot is at rest (the braking time).

Definition 2 (Passive Friendly Safety): a state s is safe under Passive Friendly Safety (or pf-safe) iff there exists at least one braking manoeuvre starting at s that is collision-free until $\max(T_b + T_{ob})$, with T_b the braking time of the robotic platform, and T_{ob} the maximal braking time of any moving object present in the local environment.

Several observations are in place: first, Passive Safety and Passive Friendly Safety are identical in both of our typical applications: in inncer city-environemnts, humans are the predominant dynamic obstacle, whereas on highways it is other cars. Their deceleration and evasion capabilities are comparable to or surpass the ones of the robotic platform. Second, safety guarantees critically depend on the knowledge of the evolution of the dynamic environment. In presence of decision-making individuals we may thus never be completely certain about our predictions. Hence, a stochastic approach to modelling the future evolution of the robot's local environment seems to be the only option.

3.7 Optimization Constraints & Criteria

In the light of the above elaboration, we incorporate an optimization criterion which performs a tradeoff between deterministic solution optimality (i.e. based on shortest path, time or comfort measures) and collision risk.

3.8 Local Planner

The local planner consists of a method inside an infinite loop which is executed at roughly 10 Hz. It first updates new sensor inputs, and receives a local robot-centered occupancy grid representation of the environment as well as a predicted dynamic obstacle map (risk map). The method then expands motion primitives (edges), starting from the robot's present configuration, for as long as deliberation time permits. Finally, the best partial motion sequence is selected according to the selected optimization criterion.

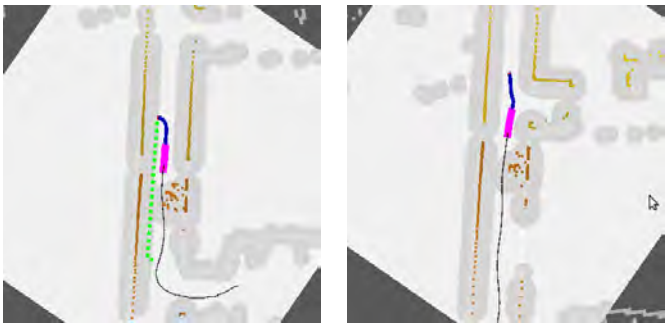

Figure 3: Structured environment where the robot follows a narrow hallway.

4 Performance Evaluation

We implmented the trajectory planner described in this report (including auxiliary parts) on the robotic demonstrator, depicted in Figure 1, left. The evaluation is separated into two parts, namely static environments, and dynamic scenes.

4.1 Static Environments

In this scenario, the robot is expected to behave correctly in unstructured environments as well as in narrow, lane-like surroundings. Both of these are found in our laboratory, where the robot has performed numerous hours of autonomous operation with minimal human intervention. Our method is able to negotiate narrow openings (such as doors) where clearance to each side is less than 5cm. Furthermore, the robot operates smoothly along long and narrow hallways (see Figure 3).

4.2 Dynamic Environments

In this scenario, the robot is expected to predict the future motion of other dynamic objects in the environment and react appropriately. In numerous tests with humans we observed reasonable robot behavior, where our motion planning algorithm reacts to possible future collisions early and plans an avoidance maneouver accordingly. In particular, by using our mehtod an avoidance manoeuvre is initiated earlier than by a comparable algorithm lacking the predictive component. This is illustrated in Figure 4, left. However, during interaction our method occasionally tends to switch between avoidance maneouvers to either side of the obstacle, leading to stalls (see Figure 4, center and right). This behavior is well known between human-human interaction, where it is coined reciprocal dances [11]. Note, that safety can still be guaranteed according to the passive safety definition if the robot decelerates in such situations, although traffic throughput is reduced. While this is a reasonable choice for human-robot interaction at low speeds, it is rarely an option during high-speed operation. An immediate workaround is to apply a histeresis-like element in the planning process, but in that case safety can no longer be guaranteed. Devising a solution to this important issue represents current research and future work.

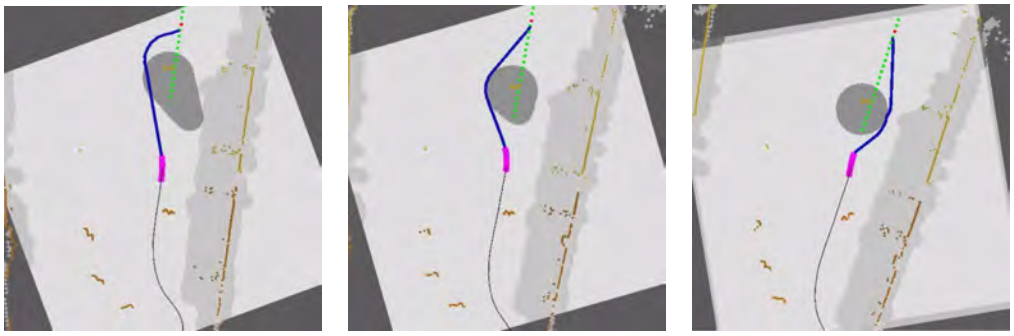

Figure 4: Unstructured scene where the robot follows the wall to the right and moves upwards. Several pedestrians are present in the scene (yellow laser points reflected off their legs), but only one of them is in the field of view of the robot's cameras. *Left,* avoidance of the detected pedestrian which is walking towards the robot. *Center & right,* switching behavior between an avoidance manoeuvre to the left and one to the right emerges as the pedestrian moves closer.

5 Conclusions and Future Work

Within the mc3 project we developed a novel local planning and collision avoidance method based on discrete graph search. The novelty of our method is twofold: first, the generated solution trajectory is model based and can thus be directly executed by the robot with minimal control interference. Second, we successfully employed motion prediction to actively foresee and prevent dangerous situations before they arise. Tests on a differential-drive demonstrator robot confirm the superior theoretical properties in practice.

Nonetheless, we also observed our algorithm is prone to switching behaviors between different avoidance maneouvers. This effect, which is also regularly encountered between humans, can lead to dangerous situations. In the future, we will further investigate to which extent these situations can be avoided or mitigated through the use of appropriate algorithms. In this regard, the concept of Velocity Obstacles [11] – mentioned in the review – seems most promising.

6 Published Research within mc3

- M. Rufli and R. Siegwart. On the Application of the D* Search Algorithm to Time-Based Planning on Lattice Graphs. In *Proceedings of the European Conference on Mobile Robots (ECMR)*, 2009.
- M. Rufli and R. Siegwart. On the Design of Deformable Input- / State-Lattice Graphs. In *Proceedings of the IEEE International Conference on Robotics and Automation (ICRA)*, 2010.

References

[1] P. E. Hart, N. J. Nilsson, and B. Raphael. A formal basis for the heuristic determination of minimum cost paths. In *Autonomous Mobile Robots: Perception, Mapping, and Navigation (Vol. 1)*, pages 375–382, Los Alamitos, CA, 1991.

[2] Steven M. LaValle. Planning algorithms. *Cambridge University Press, New York*, 2004.

[3] V. J. Lumelsky and T. Skewis. Incorporating range sensing in the robot navigation function. *IEEE Transactions on Systems, Man, & Cybernetics*, 20(5):1058–1069, 1990.

[4] J. Borenstein and Y. Koren. The vector field histogram - fast obstacle avoidance for mobile robots. *IEEE Journal of Robotics and Automation*, 7:278–288, 1991.

[5] I. Ulrich and J. Borenstein. VFH+: Reliable obstacle avoidance for fast mobile robots. In *Proceedings of the IEEE International Conference on Robotics and Automation (ICRA)*, 1998.

[6] I. Ulrich and J. Borenstein. VFH*: Local obstacle avoidance with look-ahead verification. In *Proceedings of the IEEE International Conference on Robotics and Automation (ICRA)*, 2000.

[7] J. Minguez and L. Montano. Nearness diagram (ND) navigation: Collision avoidance in troublesome scenarios. *IEEE Transactions on Robotics and Automation*, 20:2004, 2004.

[8] D. Fox, W. Burgard, and S. Thrun. The dynamic window approach to collision avoidance. *IEEE Robotics & Automation Magazine*, 1997.

[9] P. Fiorini and Z. Shiller. Motion planning in dynamic environments using velocity obstacles. *International Journal of Robotics Research*, 17:760–772, 1998.

[10] F. Large, S. Sckhavat, Z. Shiller, and C. Laugier. Using non-linear velocity obstacles to plan motions in a dynamic environment. In *Proceedings of the IEEE International Conference on Control, Automation, Robotics and Vision (ICARCV)*, 2002.

[11] J. van den Berg, M. Lin, and D. Manocha. Reciprocal velocity obstacles for real-time multi-agent navigation. In *Proceedings of the IEEE International Conference on Robotics and Automation (ICRA)*, 2008.

[12] S. Pellegrini, A. Ess, K. Schindler, and L. van Gool. You'll never walk alone: Modeling social behavior for multi-target tracking. In *Proceedings of the International Conference on Computer Vision (ICCV)*, 2009.

[13] A. Kushleyev and M. Likhachev. Time-bounded lattice for efficient planning in dynamic environments. In *Proceedings of the IEEE International Conference on Robotics and Automation (ICRA)*, 2009.

[14] E. W. Dijkstra. A note on two problems in connexion with graphs. *Numerische Mathematik*, 1:269–271, 1959.

[15] A. Ess, R. Benenson, L. van Gool, and B. Leibe. EUROPA deliverable D2.3: Tracking system, 2010.

[16] T. Fraichard. A short paper about motion safety. In *Proceedings of the IEEE International Conference on Robotics and Automation (ICRA)*, 2007.

On the Design of Deformable Input- / State-Lattice Graphs

Martin Rufli Roland Siegwart

Autonomous Systems Lab, Institute for Robotics and Intelligent Systems, ETH Zurich
Tannenstrasse 3, CH-8092 Zurich, Switzerland

martin.rufli@mavt.ethz.ch rsiegwart@ethz.ch

***Abstract*— In this paper we describe a novel and simple to implement yet effective lattice design algorithm, which simultaneously produces input *and* state-space sampled lattice graphs. The presented method is an extension to the ideas suggested by Bicchi *et al.* on input lattices and is applicable to systems which can be brought into (2,n) chained form, such as kinematic models of unicycles, bicycles, differential-drive robots and car-like vehicles (pulling several trailers).**

We further show that a transformation from chained form to path coordinates allows the resulting lattice to be bent along any C^1 continuous path. We exploit this fact by shaping it along the skeleton of arbitrary structured environments, such as the center of road lanes and corridors. In our experiments in both structured (i.e. on-road) and unstructured (i.e. parking lot) scenarios, we successfully demonstrate for the first time the applicability of lattice-based planning approaches to search queries in arbitrary environments.

***Index Terms*— Non-holonomic motion planning, deformable input- / state-lattice**

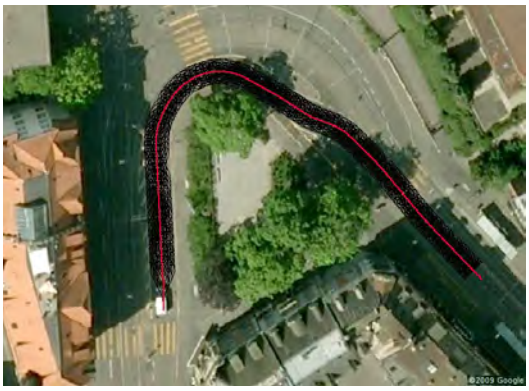

Fig. 1. Google maps view of Haldenegg curve, Zurich. Our novel lattice is bent along the centerline of the right lane. Using this approach, solutions on the lattice are naturally aligned with the road's direction.

I. INTRODUCTION

Global real-time trajectory planning has traditionally been achieved by reducing the high-dimensional state-space to a simpler more approachable one, such as a 2D grid. While moving obstacles and arbitrary robot shape can be treated within the reduced-dimensional planning setup (i.e. via frequent re-planning [1], [2] or motion prediction [3], and conservative obstacle inflation, convolution approaches [1], [4], respectively), the resulting plan's violation of (nonholonomic) vehicle constraints either necessitates the addition of a path smoothing layer, which negates any previously obtained optimality guarantees, or an exceedingly robust and consequently slow controller implementation.

Recently it has thus been realized, that by incorporating vehicle kinematic (and dynamic) constraints into the planning stage, the load on the path following and controller modules may be reduced dramatically, and impassable and / or potentially dangerous (dynamic) regions may be identified and avoided before encountering them directly. Unfortunately, the incorporation of such constraints increases the complexity of the motion planning problem dramatically (for a kinematic car-like vehicle this would amount to the addition of heading, steering angle, velocity and time dimensions in addition to 2D position), resulting both in a substantially larger and more complex search space.

At the same time, applications in dynamic urban environments demand real-time planning and re-planning capability (i.e. at 10Hz). The tradeoff between higher-dimensional (and thus more precise) search queries and low execution times is thus a delicate one, that has led to several environment and application specific approaches. Primarily we distinguish between cases where the structure can be deduced from the environment (such as on-road, and in-door), and cases, where such structure is largely lacking (off-road, parking lots).

In the former case, Dolgov *et al.* employ a low-dimensional search followed by a smoothing step, where the smoothing minimizes the orientation mismatch between the path and the external structure [5]. They argue that the low-dimensional solution typically returns a motion close to the optimal high-dimensional one, so that the smoothing step then finds the local high-dimensional optimum in the vicinity (which is often the global one). While this approach may work well in static cases, it fails in dynamic scenes where the low-dimensional search ignores vital non-convex elements of the high-dimensional cost map. Howard *et al.* solve two-point boundary problems between the current vehicle position and a point some fixed distance ahead along the structured environment (such as a road) [1]. In areas where such structure is lacking, it is difficult to assess whether a potential goal state lies along the globally optimal trajectory, however.

In the latter case, lattice based planner have emerged as the solution of choice, as they may yield (sub-) optimality guarantees on the underlying lattice graph at a low compu-

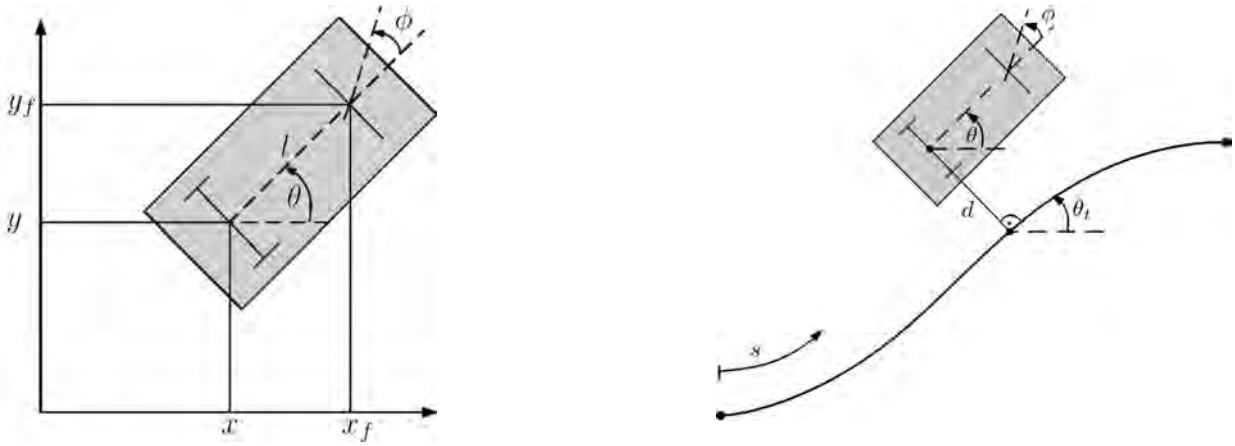

Fig. 2. **Left:** Vehicle kinematics in *physical form*. (x, y) denote the 2D position of the rear- and $(x_\mathrm{f}, y_\mathrm{f})$ of the front-axle center. Heading (θ) is measured counter-clockwise with respect to the x-axis and steering angle (ϕ) with respect to the vehicle orientation. The wheelbase of the vehicle is described with l. **Right:** Vehicle kinematics in *path form*. The reference path s is fully defined trough its curvature $c(s)$. (s, d) denote the distance along, and perpendicular to the path, respectively. $\theta_\mathrm{p} = \theta - \theta_\mathrm{t}$ marks the difference in heading between path and vehicle and ϕ is the steering angle.

tational cost. Bicchi *et al.* suggest an input sampled lattice, which is obtainable for a wide range of vehicle models via a coordinate transformation into chained form coordinates [6]. For certain input sets they prove that the transformed state space spans a lattice. Later, Pivtoraiko *et al.* developed an algorithm to generate lattices in state space directly [7]. Their method is more involved but generates a minimal edge-representation for the chosen state space discretization. Nonetheless, the globally fixed state-space discretization (in heading dimension) has so far prohibited the employment of lattices in structured environments.

This concern is resolved by our main contribution. It has its foundation in a principled yet simple method for the simultaneous generation of an input *and* state lattice that is applicable to vehicle models which can be brought into (2,n) chained form (such as the kinematic model of a car). A coordinate transformation from chained form into so called path coordinates then allows for the bending of this lattice along arbitrary C^1 continuous paths and thus for the first time enables its use in structured environments.

The remainder of this paper is organized as follows: in Sections II & III we review the kinematic model of a car-like vehicle, and then analyze its reachable set. Section IV details our novel lattice generation algorithm. Finally, in Section V we provide a comparison between regular and shaped lattices in hybrid structured-unstructured environments, where previously lattice planners could not be employed.

II. KINEMATIC MODEL OF A CAR-LIKE VEHICLE

In this section we review the kinematics of a slowly-steered car-like vehicle consisting of four states that span the configuration space: 2D position (x, y), heading (θ) and steering angle (ϕ). These kinematics may be described in various equivalent coordinate frames (treated in Sec. II-B & II-C) to facilitate some of the arguments in Sec. III & IV.

When referring to a *system*, throughout this paper we mean it in the context of control theory and modelling [6].

Definition 1. *"A* system *is a quintuple* (X, T, U, Ω, A)*, where* X *denotes the configuration set,* T *an ordered time set,* U *a set of admissible (possibly configuration dependent) input symbols,* Ω *a set of admissible input words formed by symbols in* U *and* A *a state transition map* $A : T \times \Omega \times X \to X$*" [6].*

A. Physical Form Coordinate Frame

An easily approachable way of deriving the kinematic representation of a (rear-wheel driven) car-like vehicle involves the four states (x, y, θ, ϕ) as introduced in Fig. 2, left. We will henceforth refer to this representation as *physical form*. The vehicle is subject to two non-holonomic constraints, one each for the lumped together front $(x_\mathrm{f}, y_\mathrm{f})$ and rear (x, y) wheels. They specify that the velocity of each wheel must never have any lateral component (roll and no-slip condition).

$$\begin{aligned} 0 &= \dot{x}_\mathrm{f} \sin(\theta + \phi) - \dot{y}_\mathrm{f} \cos(\theta + \phi) \\ 0 &= \dot{x} \sin\theta - \dot{y} \cos\theta \end{aligned} \tag{1}$$

Furthermore, the front axle coordinate and velocity components are related to their rear axle counterparts through the rigid body assumption (with l the vehicle wheelbase)

$$\begin{aligned} x_\mathrm{f} &= x + l\cos\theta \\ y_\mathrm{f} &= y + l\sin\theta \end{aligned} \quad \Longrightarrow \quad \begin{aligned} \dot{x}_\mathrm{f} &= \dot{x} - \dot{\theta}\, l \sin\theta \\ \dot{y}_\mathrm{f} &= \dot{y} + \dot{\theta}\, l \cos\theta \end{aligned} \tag{2}$$

Finally, the means by which we act on the vehicle are specified via forward speed v_car (throttle) and the front wheels' steering velocity $\dot{\phi}$ (through the steering wheel). We refer to these inputs as

$$\begin{aligned} v_1 &= v_\mathrm{car} = \sqrt{\dot{x}^2 + \dot{y}^2} \\ v_2 &= \dot{\phi} \end{aligned} \tag{3}$$

By combining Eqns. 1-3 and solving for the state variables $[x, y, \theta, \phi]^T$, the kinematic state-space representation in physical form is obtained (System 1).

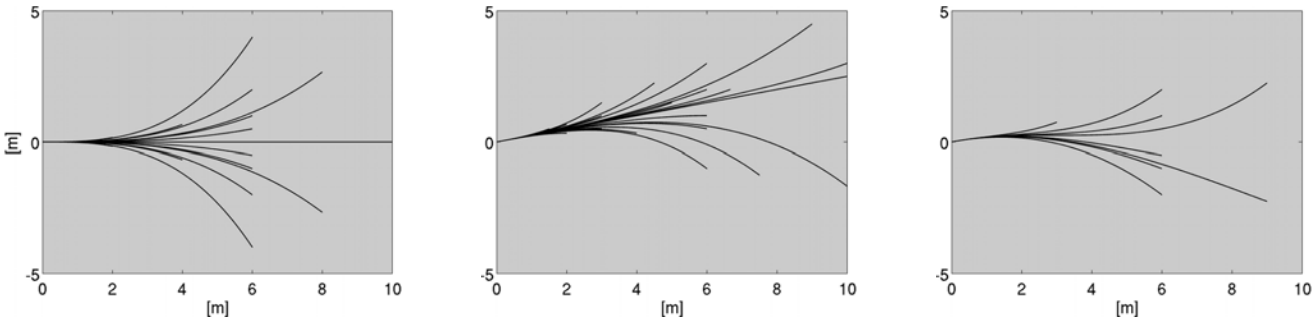

Fig. 3. 24-directional input and state lattice displayed for several initial conditions. Heading levels are unevenly spaced. Steering angle discretization is heading dependent. $(.)_\mathrm{i}$ denotes initial values. **Left:** $(\theta_\mathrm{i}, \phi_\mathrm{i}) = (0, 0)$, **Center:** $(\theta_\mathrm{i}, \phi_\mathrm{i}) = (\mathrm{atan}\,0.25, 0)$, **Right:** $(\theta_\mathrm{i}, \phi_\mathrm{i}) = (\mathrm{atan}\,0.25, -0.39)$.

System 1 (Physical Form)**.**

$$\begin{bmatrix} \dot{x} \\ \dot{y} \\ \dot{\theta} \\ \dot{\phi} \end{bmatrix} = \begin{bmatrix} \cos\theta \\ \sin\theta \\ \tan\phi/l \\ 0 \end{bmatrix} v_1 + \begin{bmatrix} 0 \\ 0 \\ 0 \\ 1 \end{bmatrix} v_2$$

B. Chained Form Coordinate Frame

The (2,4) single chain form (as given in System 2) describes the kinematics of of a car-like vehicle in an alternate coordinate frame, whose states x_2 and x_3 do not exhibit direct physical meaning. The representation's usefulness is mainly predicated on its close to linear structure (which renders it interesting for controller design), and the existence of a coordinate transformation to System 1. It was first introduced by Murray *et al.* [8] as a tool to steer vehicles.

System 2 (2,4 Chained Form - Continuous Time Notation)**.**

$$\begin{aligned} \dot{x}_1 &= u_1 \\ \dot{x}_2 &= u_2 \\ \dot{x}_3 &= x_2\, u_1 \\ \dot{x}_4 &= x_3\, u_1 \end{aligned}$$

We readily verify that System 1 may be brought into $(2, 4)$ chained form using the change of coordinates and input transformations given in Eqn. 4 [8].

$$\begin{aligned} x_1 &= x \\ x_2 &= \tfrac{1}{l}\sec^3\theta\tan\phi \\ x_3 &= \tan\theta \\ x_4 &= y \\ v_1 &= u_1/\cos\theta \\ v_2 &= u_2\, l\,\cos^3\theta\cos^2\phi\, - \\ &\quad\; 3\,\tfrac{u_1}{l}\sin\theta\sin^2\phi\cos^2\theta \end{aligned} \tag{4}$$

C. Path Coordinate Frame

The third coordinate frame relevant to this paper, commonly referred to as path coordinate frame (consult System 3 and Fig. 2, right for a description of the variables used), has been popular in vehicle control applications (see i.e. [9]). In this formulation, the problem of stabilizing a robot onto a reference path s (which is fully defined through its curvature $c(s)$) is reduced to the regulation of the states $[d, \theta_p, \phi]^T$ to zero, irrespective of the path's shape.

System 3 (Path Form)**.**

$$\begin{bmatrix} \dot{s} \\ \dot{d} \\ \dot{\theta}_\mathrm{p} \\ \dot{\phi} \end{bmatrix} = \begin{bmatrix} \frac{\cos\theta_\mathrm{p}}{1-d\,c(s)} \\ \sin\theta_\mathrm{p} \\ \frac{\tan\phi}{l} - \frac{c(s)\cos\theta_\mathrm{p}}{1-d\,c(s)} \\ 0 \end{bmatrix} \cdot v_1 + \begin{bmatrix} 0 \\ 0 \\ 0 \\ 1 \end{bmatrix} \cdot v_2$$

The inputs (v_1, v_2) of System 3 again take the form of $(v_\mathrm{car}, \dot{\phi})$. Similar to the case with physical coordinates, path coordinates may also be transformed into (2,4) chained form via the state and input transformations given in Eqn. 5 [9].

$$\begin{aligned} x_1 &= s \\ x_2 &= \tfrac{(1-d\,c(s))^2\tan\phi}{l\cos^3\theta_\mathrm{p}} - c'(s)\,d\tan\theta_\mathrm{p}\, - \\ &\quad\; c(s)\,(1-d\,c(s))\tfrac{1+\sin^2\theta_\mathrm{p}}{\cos^2\theta_\mathrm{p}} \\ x_3 &= (1-d\,c(s))\tan\theta_\mathrm{p} \\ x_4 &= d \\ v_1 &= \tfrac{1-d\,c(s)}{\cos\theta_\mathrm{p}}\,u_1 \\ v_2 &= \alpha_2(u_2 - \alpha_1 u_1) \\ \alpha_1 &= \tfrac{\delta x_2}{\delta s} + \tfrac{\delta x_2}{\delta d}(1-d\,c(s))\tan\theta_\mathrm{p}\, + \\ &\quad\; \tfrac{\delta x_2}{\delta\theta_p}\left(\tfrac{\tan\phi\,(1-d\,c(s))}{l\cos\theta_\mathrm{p}} - c(s)\right) \\ \alpha_2 &= \tfrac{l\cos^3\theta_p\cos^2\phi}{(1-d\,c(s))^2} \end{aligned} \tag{5}$$

Note that Eqn. 5 strongly depends on the selected path and its derivative. c(s) is thus required to be at least C^1 continuous.

III. REACHABLE SETS OF THE KINEMATIC SYSTEMS IN CHAINED AND PHYSICAL FORM

The starting point of this section is constituted by the work of Bicchi *et al.* on input lattices [6]: specifically, we draw on their important findings that the reachable set of the chained form System 2 is discrete and forms a lattice in state-space iff the input set fulfills certain conditions (detailled in Theorem 1). By computing the systems's reachable set explicitly, we obtain a relation between the innput set's sampling levels and the chained form system's state-space discretization (Sec. III-A). Further, by applying the transformation between chained and physical form coordinates from the preceding section (Eqn. 4), we arrive at a mapping between discretization levels in physical form state-space and sampling levels in chained form input space (Sec. III-B). Our lattice design algorithm (Sec. IV) builds on this result.

Fig. 4. **Top Left:** Google Street View scene close to Bellevue, Zurich. **Bottom Left:** corresponding Google Maps image. Impassable areas are shaded gray. **Bottom Center:** 2D heuristic map. Color indicates cost to goal. **Right:** plan from start- (green) to goal-configuration (black). The lattice shape (at $d = 0$) is displayed in red. Note that the curvature is set to zero in the parking lot area due of lack of structure in close vicinity. Instead, the direction is aligned with the dominant orientation of the lot area. The solution on the deformable lattice is represented in blue, the one on the fixed lattice in yellow.

A. Reachability of the Chained Form System 2

Definition 2. *The* reachable set *of a system S at initial configuration q_i is comprised of the set of configurations $q \in \mathcal{Q}$ which are attained by incrementally applying a set of allowable inputs $u \in \mathcal{U}$ to q_i and its successor configurations. The reachable set may form a tree (continuous) or a lattice (discrete) in the state-space of S.*

Theorem 1. *The reachable set of System 2 is discrete and forms a lattice in state-space iff the input set $\mathcal{U}$, with $u = [u_1, u_2]^T \in \mathcal{U}$ piecewise constant, is selected as*

$$\mathcal{U} = \{diag(\lambda)\, Ws,\ s \in S\} \subset \mathbb{R}^2$$

with $W \in \mathbb{Q}^{2x2}$ an invertible matrix, $\lambda \in \mathbb{R}^2$ and $S \subset \mathbb{Z}^2$.

Compiled from [6], Theorem 9, Defs. 4 & 8.

The reachable set of System 2 may therefore only form a lattice, if all control inputs $[u_1, u_2]^T$ assume piecewise constant values. Hence, we may restate System 2 in discrete, exact unit-time sampled notation [6].

System 4 (2,4 Chained Form - Discrete Time Notation)**.**

$$\begin{aligned} x_1^+ &= x_1 + u_1 \\ x_2^+ &= x_2 + u_2 \\ x_3^+ &= x_3 + x_2 u_1 + \tfrac{u_1 u_2}{2} \\ x_4^+ &= x_4 + x_3 u_1 + \tfrac{x_2 u_1^2}{2} + \tfrac{u_1^2 u_2}{6} \end{aligned}$$

Incremental step size in the reachable set of System 4 turns out to be a function of the greatest common divisor of all $u \in \mathcal{U}$, which we denote as u_d. We may thus specify $u_\mathrm{d} = [u_{1\mathrm{d}}, u_{2\mathrm{d}}]^T$ directly by selecting λ, W, and S

$$\lambda = \begin{bmatrix} u_{1\mathrm{d}} \\ u_{2\mathrm{d}} \end{bmatrix}, \qquad W = \begin{bmatrix} 1 & 0 \\ 0 & 1 \end{bmatrix}, \qquad S = \mathbb{Z}^2,$$

so that u_d is itself part of the set $\mathcal{U}$. The reachable set of System 4 is then easily computed (Eqn. 6).

B. Reachability of the Physical Form System 1

Through Eqn. 4 we are able to relate the reachable set in chained form (Eqn. 6)

$$\begin{bmatrix} x_1 \\ x_2 \\ x_3 \\ x_4 \end{bmatrix} \in \begin{bmatrix} \mathcal{X}_1 \\ \mathcal{X}_2 \\ \mathcal{X}_3 \\ \mathcal{X}_4 \end{bmatrix} \subset \begin{bmatrix} k_1\, u_{1\mathrm{d}} \\ k_2\, u_{2\mathrm{d}} \\ k_3\, \frac{u_{1\mathrm{d}}\, u_{2\mathrm{d}}}{2} \\ k_4\, \frac{u_{1\mathrm{d}}^2\, u_{2\mathrm{d}}}{6} \end{bmatrix} \forall k_i \in \mathbb{Z} \qquad (6)$$

to the much more complex reachable set in physical coordinates, given by Eqn. 7.

$$\begin{bmatrix} x \\ y \\ \theta \\ \phi \end{bmatrix} \in \begin{bmatrix} \mathcal{X} \\ \mathcal{Y} \\ \mathcal{T} \\ \mathcal{P} \end{bmatrix} \subset \begin{bmatrix} k_1\, u_{1\mathrm{d}} \\ k_4\, \frac{u_{1\mathrm{d}}^2\, u_{2\mathrm{d}}}{6} \\ \mathrm{atan}(k_3\, \frac{u_{1\mathrm{d}}\, u_{2\mathrm{d}}}{2}) \\ \mathrm{atan}(k_2\, u_{2\mathrm{d}}\, l \cos^3\theta) \end{bmatrix} \qquad (7)$$

Unfortunately, the transformation between physical coordinates and chained form (Eqn. 4) is subject to some restrictions: for uniformly sampled x_3 in chained form (System 2), the heading discretization in physical coordinates (System 1) becomes denser towards $\pm\pi/2$, where the transformation is not defined due to a singularity. Previous work with chained form systems has therefore been limited to problems where the heading could be constrained to the interval $(-\pi/2, \pi/2)$, as in autonomous vehicle parking applications [10], [11]. For generic motion planning problems, such a restriction cannot be imposed, however.

In order to overcome this issue, and thus expand the reachable set of Eqn. 7 to heading levels outside the interval $(-\pi/2, \pi/2)$, we introduce a second *physical form* coordinate system, rotated counter-clockwise by $\pi/2$ with respect to the original one. Variables in the rotated frame are denoted with $(.)_\mathrm{rot}$. The challenge then lies in *merging* the two distinct reachable sets via mutually reachable states. For the heading levels, this is enforced via Eqn. 8 for some $m, n \in \mathbb{Z}$.

$$\theta \stackrel{!}{=} \tfrac{\pi}{2} - \theta_\mathrm{rot} \Rightarrow \mathrm{atan}(m\, \tfrac{u_{1\mathrm{d}} u_{2\mathrm{d}}}{2}) \stackrel{!}{=} \tfrac{\pi}{2} - \mathrm{atan}(n\, \tfrac{u_{1\mathrm{d}} u_{2\mathrm{d}}}{2}) \qquad (8)$$

Lemma 2. $\operatorname{atan}\kappa + \operatorname{atan}(1/\kappa) = \pi/2 \;\; \forall \kappa > 0$
Proof : $\frac{d\operatorname{atan}\kappa}{d\kappa} + \frac{d\operatorname{atan}(1/\kappa)}{d\kappa} = \frac{1}{\kappa^2+1} - \frac{1}{(\kappa^{-2}+1)\,\kappa^2} \equiv 0$
$\pi/2$ *is obtained through insertion.*

By rearranging Eqn. 8 appropriately, the same structure as in Lemma 2 is obtained. We conclude that $\forall\theta \neq 0,\ \theta \in \mathcal{T}$ iff $\frac{n\,u_{1\mathrm{d}}u_{2\mathrm{d}}}{2} = \frac{2}{m\,u_{1\mathrm{d}}u_{2\mathrm{d}}}$ for some $m, n \in \mathbb{Z}$ and artificially construct a merged reachable set which is comprised of states that are mutually reachable from both coordinate frames only. It follows from Eqn. 7 that the number of heading levels in this merged reachable set is a function of $u_{1\mathrm{d}}\,u_{2\mathrm{d}} = u_{\mathrm{comb}}$.

A similar argument holds for the number of mutual steering angles ϕ: likewise to heading, the discretization in steering angle ϕ is more densely sampled towards $\theta = \pm\pi/2$, and thus becomes configuration dependent. In cases where steering angle saturation needs to be considered, it is thus of interest to compute the minimal number of discrete values obtainable over all heading levels. By inserting the largest attainable steering angle $\phi_{\max}$ into Eqn. 4:

$$\phi_{\max} \overset{!}{\geq} \operatorname{atan}\left(x_2\, l \cos^3\theta\right), \tag{9}$$

it can be shown that this number always occurs at $\theta = 0$.

IV. DEFORMABLE INPUT- / STATE-LATTICE DESIGN PROCEDURE

Now that we have introduced all essential auxiliary parts, let us focus on the development of our main contribution, an algorithm for the simple yet effective design of deformable input- and state-sampled lattice graphs. The procedure draws heavily from the preceding sections: it builds on the work of Bicchi *et al.* [6] on input sampled lattices for chained form systems (Theorem 1) and on Eqn. 7 which relates the reachable set in physical coordinates to the design parameters u_{d} in chained form. Essentially, we add an additional layer on top of the approach of Bicchi *et al.* [6], so that their algorithm allows us to build a lattice in physical form coordinates based on physical form specifications directly.

A. Lattice Design Algorithm

In Bicchi's method [6], a lattice spanning the four-dimensional chained form configuration space is constructed by specifying a two-dimensional input set $\mathcal{U}$ only. The approach is thus clearly overconstrained with respect to the obtainable state space discretization: in fact we are restricted to the direct specification of two states' discretization levels in chained form only. The resolution of the remaining two states emerges from the design procedure.

For practical reasons, we are typically interested in specifying a discretization in physical coordinates directly, however. To this end we apply Eqn. 7 to specify $\mathcal{U}$ based on a desired physical form state-space discretization. This forms the starting point of our lattice design algorithm.

As a means of illustration, we specify a discretization in heading (θ) and steering angle (ϕ) directly, although any other combination of two states is equally feasible. (x, y)-discretization then emerges from the design procedure, and needs to be verified a posteriori.

$\mathbf{u}_{\mathrm{comb}}$	**# Head.**	**Heading Discr. Lvls in 1^{st} Octant**
2	8	$\{0, \operatorname{atan}1\}$
1	16	$\{0, \operatorname{atan}\frac{1}{2}, \operatorname{atan}1\}$
1/2	24	$\{0, \operatorname{atan}\frac{1}{4}, \operatorname{atan}\frac{1}{2}, \operatorname{atan}1\}$
1/3	32	$\{0, \operatorname{atan}\frac{1}{6}, \operatorname{atan}\frac{1}{3}, \operatorname{atan}\frac{1}{2}, \operatorname{atan}1\}$

TABLE I
HEADING LEVELS AS A FUNCTION OF THE PARAMETER $\mathrm{u}_{\mathrm{comb}}$

Algorithm 1 (Input- and State-Lattice Design)**.**

1) *Gather vehicle specific information, notably vehicle wheelbase (l) and maximal steering angle ($\phi_{\max}$).*
2) *Decide on a desired number of heading levels θ in physical coordinates and consult Table I or Eqn. 8 to obtain the corresponding value of $u_{\mathrm{comb}} = u_{1\mathrm{d}}\,u_{2\mathrm{d}}$.*
3) *Decide on a minimal number of steering angle levels. As shown above, this value will be encountered at $\theta = n\,\pi/2,\ \forall n \in \mathbb{Z}$. Through Eqn. 9, a discretization in x_2, and thus in u_2 is obtained.*
4) *The discretization of x_1 is obtained by inserting u_2 into u_{comb} and solving for u_1. The discretization in x_4 results from Eqn. 6.*
5) *For each initial chained form state of the chosen discretization $[x_{1\mathrm{i}}, x_{2\mathrm{i}}, x_{3\mathrm{i}}, x_{4\mathrm{i}}]^T \in [\mathcal{X}_1, \mathcal{X}_2, \mathcal{X}_3, \mathcal{X}_4]^T$ (with $(x_{1\mathrm{i}}, x_{4\mathrm{i}}) = (0, 0)$ due to translational invariance), apply all inputs $u \in \mathcal{U}$ that are part of the input sampling to arrive at a set of configuration dependent outgoing edges. They form the lattice.*
6) *Remove edges from the lattice which start or end at heading / steering angle levels, that are not part of both the original and the rotated coordinate frame.*

Via Algorithm 1 we designed a 24-directional lattice with at least seven discrete steering angles (occurring at $\theta = 0$), and an (x,y)-discretization of $\frac{1}{12}$m for a 2008 Toyota Prius ($l = 2.7\,\mathrm{m}$, $\phi_{\max} = 0.6\,\mathrm{rad}$, displayed in Fig. 3).

Despite the apparent focus on car-like vehicles, it should be noted that the theory developed in this paper equally applies to all other systems which can be transformed into (2,n) chained form. A sufficient algorithm is described in [8].

B. Geometrical Properties of the Lattice

Our lattice design procedure requires piecewise constant inputs (u_1, u_2) in chained form. Thus x_1 assumes piecewise linear and x_4 piecewise cubic values. By referring to the transformation between chained form and physical form coordinates (Eqn. 4), we observe an equivalence between (x_1, x_4) and (x, y). It follows trivially that lattice segments in physical coordinates are composed of piecewise cubic polynomials.

$$y(x) = ax^3 + bx^2 + cx + d$$

Remarkably, Algorithm 1 manages to generate lattice segments which satisfy the six constraints (difference in 2D position, initial and final heading and curvature) imposed through System 2 by using cubic polynomials alone.

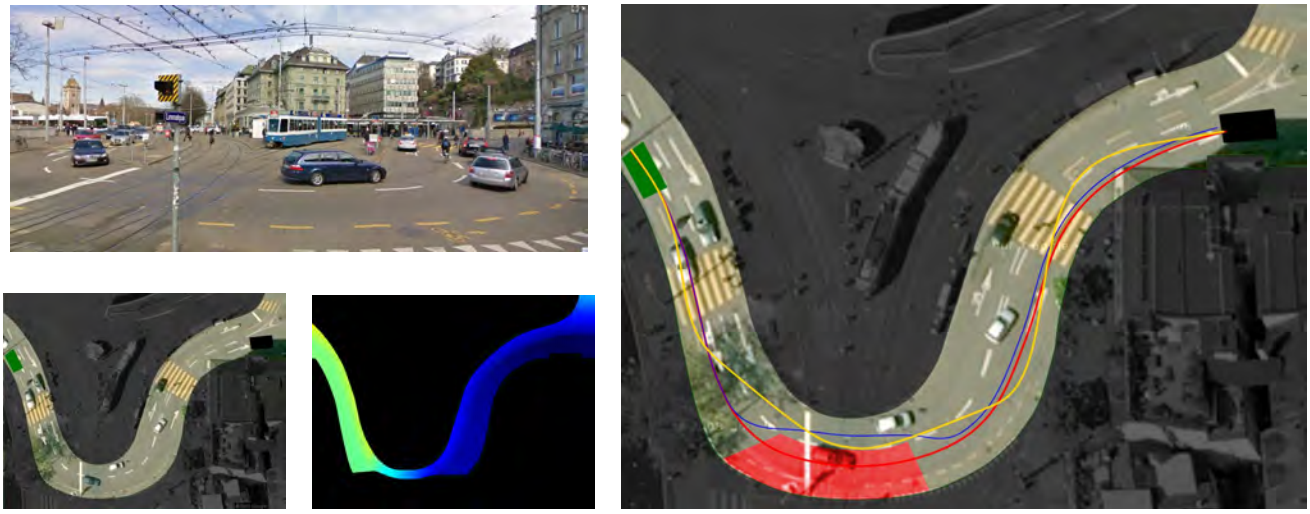

Fig. 5. **Top Left:** Google Street View scene of Central, Zurich. **Bottom Left:** corresponding Google Maps image. Impassable areas are shaded gray. **Bottom Center:** 2D heuristic map. Color indicates cost to goal. Note, that moving along the left lane is costlier. **Right:** plan from start- (green) to goal-configuration (black). A vehicle with break-down (shaded red) needs to be overtaken. The lattice shape (at $d = 0$) is displayed in red, the optimal solution on the deformable lattice in blue, and on the globally fixed lattice in yellow.

C. Lattice Deformation along Path c(s)

It is well known that lattice graphs are ill suited to applications in structured environments, as their heading discretization remains globally fixed. Rather small heading discretization levels are thus required to avoid the typical swerves in directions that are not part of the lattice. These additional heading levels affect search speed dramatically.

The concept of path coordinates (as compiled in Sec. II) is easily misappropriated to solve the above mentioned issue, however. Lattice segments (constructed with Algorithm 1) may be transformed from chained form into path coordinates via Eqn. 5, and the *specification of a reference path c(s)*. The key point is then to shape c(s) along the local structure of the environment. Notably, this result allows us for the first time to freely align the orientation of the graph's *heading* levels with the environment (provided such information can be extracted). In structured environments, sensible choices include the center lines along road lanes and corridors. In unstructured environments, the scene's local principal directions could be chosen. Once designated, the reference path $c(s)$ then constructs the lattice segments with $d \equiv 0$. Segments with $d \neq 0$ are constructed so that d remains perpendicular on the path (illustrated in Fig. 2, right).

As a consequence to the liberty in choosing $c(s)$, several auxiliary steps need to be performed during graph search in order to ensure compliance with vehicle constraints, however.

- During edge expansion, every successor edge is required to be checked for maximal curvature violation (corresponding to the maximal allowed steering angle $\phi_{\max}$). If a violation occurs, the edge may not be expanded.
- During expansion, any edges with distance from path $d(s) > 1/c(s)$ may not be expanded (degenerate case).
- Due to distortion effects $c(s)$ imposes on lattice edges, cost-map cells traversed by edges cannot be precomputed. Their calculation in real-time is thus required.

V. EXPERIMENTAL RESULTS

In this section we apply our novel deformable lattice to two difficult outdoor environments: the Zurich *Bellevue* scene contains both structured (road) and unstructured (parking lot) parts, the *Central* scene is comprised of a curved double lane segment, where a lane change needs to be performed due to an immobile car (see Fig. 5). Both scenes have been prepared manually from Google Maps images: static obstacle areas are shaded dark, lane-centers are marked in red. In both scenarios we compare our deformable lattice to the same lattice with globally fixed heading discretization. We employ an adapted version of the A* graph search algorithm to return minimal cost paths on the lattice graph. The underlying cost function attains low values on driveable terrain with slowly growing values towards the road boundaries. Obstacle areas are assigned infinite cost, and are thus impassable.

A. Bellevue Environment

Fig. 4 shows an overview of a scene close to Bellevue, Zurich and describes the different steps taken before planning: masking of obstacles and untraversable areas, generation of a 2D heuristic, labeling of unstructured environments (the parking lot is shaded in red) and centerline extraction. In blue color, the solution obtained via our novel deformable lattice is displayed. During on-road operation, we shape the lattice along the center of the lane. Once the parking lot is reached, it is shaped along the lot's dominant direction. On the road segment, the solution follows the lane center perfectly, as no obstacles need to be avoided. In the parking lot, it eventually departs the lattice centerline to park the vehicle safely in the designated spot. Contrary to that, the solution obtained with the globally anchored lattice (in yellow color) produces an excessively curved path which is typically not well aligned with nearby structures.

B. Central Environment

Fig. 5 provides an overview for the experiment at Central, Zurich. This scenario exemplifies how our deformable lattice performs on-road, where the preferred lane needs to be departed (in the present case due to a vehicle with breakdown, shaded red in Fig. 5, right). The robot is thus required to move to the left lane, overtake the stationnary vehicle and then eventually return to the right lane. The time of change, and the duration spent on the left lane is not chosen by the lattice shaping a priori, but rather by the graph search through a minimal cost solution. In the same environment, we performed a search using the globally fixed lattice. The result is a meandering path, which just barely manages to remain within the lane boundaries.

C. Discussion

With the Bellevue and Central experiments we confirmed that in curved structured environments, and in narrow environments where the orientation is not well aligned to a lattice heading, globally anchored lattices perform poorly: failure to compute a solution or, in case of success, excessively curved paths tend to emerge. By contrast, we were able to demonstrate that deformable lattices can not only be employed in unstructured environments, but in virtually any scenario (provided that, through i.e. distance transforms, the local structure or general orientation can be gathered), as they allow for the dynamic adaptation of the heading dimension during search. Compared to an anchored lattice, superior performance can thus be achieved with far fewer discrete heading levels, thereby reducing the graph's branching factor and increasing search speed. We believe it to be the first time, that high-dimensional graph search on a state lattice was employed as a universally applicable planning algorithm. Through our contribution the need for a higher-level reasoning and switching module thus vanishes. By removing the superfluous host of disparate, environment specific planning solutions, the navigation system becomes simpler, more robust and easier to optimize and operate.

VI. CONCLUSIONS AND FUTURE WORK

In this paper, we presented a novel algorithm to generate input-/state-lattices comprised of cubic splines with a user specified discretization in state space. The method is applicable to vehicles whose kinematic model is mathematically equivalent to the (2,n) chained form, and thus includes unicycles, bicycles, differential-drive robots and cars. Furthermore we presented a solution to bend such lattices along any C^1 smooth path, thereby allowing us to align the heading discretization of the lattice dynamically along the skeleton of arbitrary structured environments. We then demonstrated for the first time the applicability of this planning approach to both structured and unstructured environments.

In the future, we would like to investigate whether our lattice design approach could be extended to dynamic vehicle models and non-planar environments.

ACKNOWLEDGMENT

This work has been partially supported by the Swiss National Science Foundation NCCR 'MC3' and by the European Project 'EUROPA' under contract number FP7-231888.

REFERENCES

[1] D. Ferguson, T. Howard, and M. Likhachev. Motion Planning in Urban Environments: Part I. In *Proceedings of the IEEE/RSJ International Conference on Intelligent Robots and Systems (IROS)*, 2008.

[2] T. Howard D. Ferguson and M. Likhachev. Motion Planning in Urban Environments: Part II. In *Proceedings of the IEEE/RSJ International Conference on Intelligent Robots and Systems (IROS)*, 2008.

[3] A. Kushleyev and M. Likhachev. Time-bounded lattice for efficient planning in dynamic environments. In *Proceedings of the IEEE International Conference on Robotics and Automation (ICRA)*, 2009.

[4] M. Likhachev and D. Ferguson. Planning long dynamically-feasible maneuvers for autonomous vehicles. In *Proceedings of the Robotics: Science and Systems Conference (RSS)*, 2008.

[5] D. Dolgov and S. Thrun. Detection of principal directions in unknown environments for autonomous navigation. In *Proceedings of the Robotics: Science and Systems Conference (RSS)*, 2008.

[6] A. Bicchi, A. Marigo, and B. Piccoli. On the reachability of quantized control systems. *IEEE Transactions on Automatic Control*, 4(47):546–563, April 2002.

[7] R. A. Knepper M. Pivtoraiko and A. Kelly. Differentially constrained mobile robot motion planning in state lattices. *Journal of Field Robotics*, 26(1):308–333, March 2009.

[8] R. Murray and S. S. Sastry. Nonholonomic motion planning: Steering using sinusoids. *IEEE Transactions on Automatic Control*, 38:700–716, 1993.

[9] A. De Luca, G. Oriolo, and C. Samson. Feedback control of a nonholonomic car-like robot. *Springer, Berlin*, 1998.

[10] S. Pancanti, L. Pallottino, D. Salvadorini, and A. Bicchi. Motion planning through symbols and lattices. In *Proceedings of the IEEE International Conference on Robotics and Automation (ICRA)*, 2004.

[11] M. Rufli. Driver-in-the-loop path control for a non-holonomic vehicle. *Bachelor Thesis, ETH Zurich*, 2006.

On the Application of the D* Search Algorithm to Time-Based Planning on Lattice Graphs

Martin Rufli Roland Siegwart
Autonomous Systems Lab, ETH Zurich, Tannenstrasse 3, CH-8092 Zurich, Switzerland
martin.rufli@mavt.ethz.ch rsiegwart@ethz.ch

***Abstract*— In this paper we present a multi-resolution state lattice, which operates in four dimensions, namely 2D position, heading, and velocity. The generation of such a lattice is described, resulting in an efficient (in terms of branching factor) and feasible (i.e. directly executable) set of edges, which can be searched on using any standard graph based planner.**

Furthermore, we introduce a novel heuristic, the *time-viable heuristic* with horizon T_n, which exploits the limited (but nonetheless extremely large) number of feasible motion combinations in a state lattice of bounded time and stores them in a look-up table. This heuristic then enables recently developed incremental planning algorithms, which typically start node expansion at the goal state (such as the various D* variants [1]) to be employed in time-based search, where the time of arrival is generally unknown a priori. We show, that by employing this technique, on average a comparable number of expanded states are to be expected for a given *initial planning* problem as when using forward searching algorithms (such as A* and variants [2, 3]), thus speeding up *re-planning* by up to two orders of magnitude as reported in [4].

***Index Terms*— Non-holonomic, time-based, motion planning, state lattice, time-viable heuristic**

I. Introduction

State lattices (applied to motion planning) have recently seen much attention in scenarios, where a preferable motion cannot be easily inferred from the environment (such as in planetary exploration [5, 6], off-road navigation, or in large-scale parking lots [7, 8, 9]). They are typically constructed by pruning an extremely large set of trajectory segments (generated with a suitably complex vehicle model via input or state-space sampling), down to a manageable subset. The underlying assumption is that through a sensible pruning policy, every single original trajectory segment is reconstructable by combining motion primitives from the subset alone, yielding a maximal deviation along the trajectory no larger than e_{max}. This error bound, and thus the state-space discretization, is justified by generally non-negligible sensor and actuator uncertainties present on robotic platforms. The resulting lattice is dependent on all assumptions made during vehicle modeling. Typically it is thus not portable between different vehicles, as it is based on the robot's steering configuration, actuator capabilities, and, if modeled, tire-road interaction. Poor portability and a long offline design phase are rewarded on-line with inherent executability of each lattice segment (see Fig. 1), and competitive search speed (for the case of a 3D lattice vs. a 2D grid based planner, see [10]). In the light of the above exposition it thus seems unclear why not more autonomous robots are equipped with lattice based planners.

Most literature on planning algorithms incorporating a state lattice is restricted to static, or quasi-static environments, where the lattice typically operates in a three-dimensional state-space (2D position and heading). Dynamic obstacles are typically treated in the same way as static obstacles, except for an inflated outline. Dynamic obstacle avoidance is then guaranteed via frequent re-planning (see i.e. [9]). These approaches work well in relatively slow, or open environments, but face issues in scenarios where some participants have a much higher maximal velocity, or where dynamic obstacles may block entire routes to the goal.

In general, more information than just the current pose of a dynamic obstacle can be extracted, however. Depending on the environment, predictions of variable quality can be deduced from an object's present and past motion. Approaches, which model the physics of the obstacle (see i.e. [12, 13]) typically achieve very precise short term predictions. On the other hand, approaches which model the intention of an agent fare better in the long term [14, 15, 16]. This additional information can be implemented into the planning stage, but requires the augmentation of the lattice with a velocity dimension (as was i.e. demonstrated in outdoor scenarios [9] and in indoor environments [11] to produce time-optimal as opposed to path length optimal solutions) and the addition of time to the state space (see [17]).

Full-range planning in nD (2D position, heading, steering angle, velocities, time, ...) is computationally intensive, however, and neither justified due to the uncertainty in motion prediction growing unbounded over time. Kushleyev et al. [17] recently presented a solution to this problem by introducing the time bounded lattice, a multi-resolution lattice, where all but two dimensions (2D position) are dropped as soon as motion prediction fidelity decreases below a certain threshold. In this paper we extend on this idea and enable the application of incremental re-planning algorithms to time-bounded lattices.

The remainder of this paper is organized as follows: section II reviews heuristic search applied to time-based planning on lattice graphs with a special emphasis on the introduction of our new time-viable heuristic. In Section III we demonstrate the effectiveness of our approach both by theoretical considerations and in simulated increasingly populated (and thus complex) scenarios. Finally, in Section IV we draw conclusions and sketch future work.

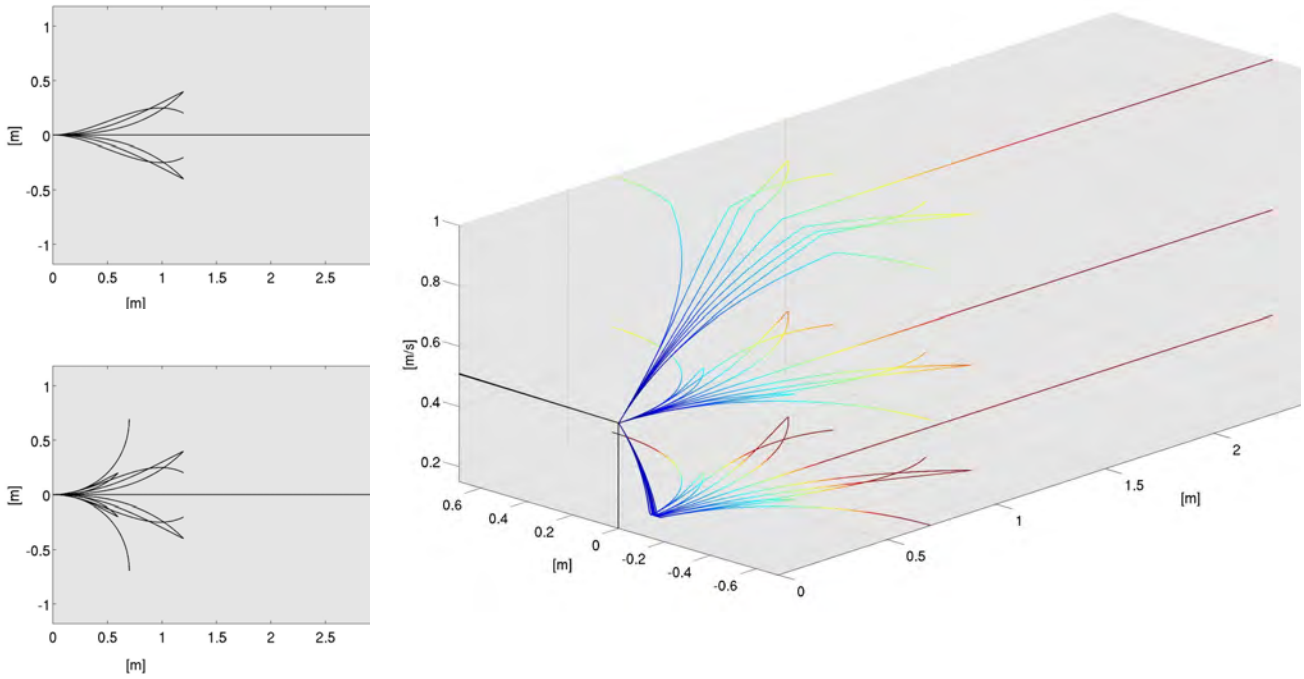

Fig. 1. 16-directional multi-resolution lattice (one of the 16 initial headings shown), as developed in [11]. Top Left: lattice low-resolution part. Bottom Left: high-resolution part. Some of the short straight segments are occluded. Right: full 4D (x, y, θ, v) view for one initial heading starting at a velocity of 0.5 m/s. Note that deceleration is higher than acceleration capability.

II. Applying D* in Combination with Motion Predictions

The efficiency by which D* repairs previously generated solutions (in many cases one to two orders of magnitude faster than re-planning from scratch [4]) renders it highly desirable for many deterministic graph search applications; especially so, as ever increasing computing power allows for higher-dimensional (and thus more complex) searches which better cope with various system and environmental constraints. By adding time to the state-space, the resulting motion is time-parametrized, and thus renders it impossible to initialize the goal state with the correct time of arrival, as this property is only known *after* computing the solution. A naive implementation would therefore estimate a time of arrival, plan, update the estimate, and continue until the estimate is confirmed. Such an implementation looses the speed boost over A* however. In this section, we present a solution to this problem in the form of a novel heuristic, the *time-viable heuristic*. We also describe the various components of our planner, with a special emphasis on adaptations due to the addition of motion predictions.

A. Graph

In [11], we developed a 4D multi-resolution lattice, where the resolution is adapted based on environmental (i.e. narrowness) and task characteristics (i.e. distance from the robot). It is generated by employing Catmul-Rom parametrized cubic splines and therefore allows for the control of end position, start and end heading, and, to some extent, maximal curvature along each segment. In the future we would like to incorporate quintic splines in order to specify curvature at edge boundaries and add rotational velocity to the state space. The lattice operates on a 0.1 m (high-res.) to 0.2 m (low-res.) grid, at 16 directions and with 6 velocities (0.0, 0.15, 0.5, 1.0 m/s, two rotational velocities). It has an average outdegree of close to 40. All successor edges of a single heading-velocity configuration are depicted in Fig. 1.

B. Heuristics

Heuristic based planner rely on a heuristic to guide them towards the goal state of the search. Well informed heuristics reduce planning time, as fewer states need to be expanded. The development of accurate heuristics is generally harder for higher-dimensional search spaces. We employ three complimentary heuristics, the combination of which is provably also a heuristic and generally very well informed.

1) 2D Heuristic: For a robot with nonholonomic constraints, a simple 2D Dijkstra search [18] on the lattice's underlying 2D grid yields accurate heuristic values far away from the robot position and in cases where environmental constraints severely limit robot mobility. As it relies on the environment, it cannot be precomputed offline. Depending on the environment size, such a computation can take several seconds, but only needs to be performed once per fixed goal state. For D* searches, this goal state (namely the current robot pose) changes continuously as the vehicle moves, however. We thus limit computation to a tunnel around a 2D A* search.

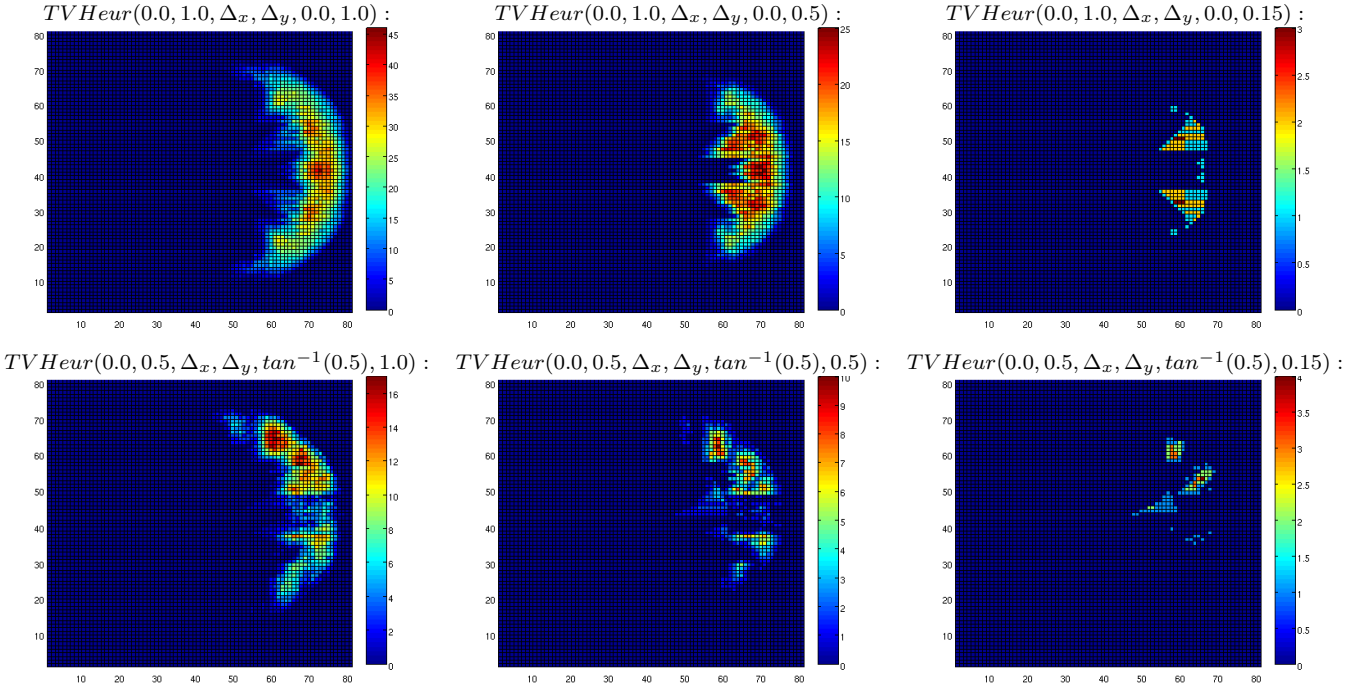

Fig. 2. Time-viable heuristic for a time horizon of $T_{max} = 4.0\,\text{s}$. Displayed are 6 initial-final-state combinations (represented as a subspace of the 6D time-viable heuristic: $TVHeur(a_{start}[rad], v_{start}[m/s], \Delta_x[m/10], \Delta_y[m/10], a_{query}[rad], v_{query}[m/s])$, where 'a' stands for heading, 'v' for velocity, and $\Delta_{x,y}$ for 2D translation between start and query state), with the vehicle origin in the center of the figure facing to the right ($a_{start} = 0.0\,\text{rad}$, $x_{start} = y_{start} = 4.0\,m$). The value of each cell corresponds to the number of time and edge distinct arrivals below T_{max} at that cell's state. The average number of such arrivals increases for larger time horizons.

2) Freespace Heuristic: The freespace heuristic returns the actual constrained cost (i.e time of traversal) of moving between two states in absence of any obstacles, and is generated by performing a Dijkstra search on the state lattice to a finite time horizon. It is thus often highly accurate in the robot vicinity, but becomes less useful further away where obstacles are likely to invalidate it. We precompute it offline and store it in a look-up table. For memory space considerations, the notion of a *trim ratio* was introduced in [19], which specifies the cost ratio between the 2D heuristic and the freespace heuristic. This ratio should be selected as close to 1.0 as memory allows.

3) The Time-Viable Heuristic: The concept of the state lattice postulates that through combination of a (small) finite set of motion primitives, essentially the whole space of feasible motions is described. This implies that the robot can only reach a finite set of states via a limited number of transitions, in bounded time. The time-viable heuristic stores this finite set of states and their predecessor edges in a look-up table. Let us denote the branching factor (a state's average number of successor edges) with BF, and the execution time of the shortest edge (0.1 m) at highest velocity (1.0 m/s) with $t_{shortest}$. The combinatorial number of non-identical trajectories is then computed to be of complexity $BF^{t_{max}/t_{shortest}}$. It thus becomes intractable for large time horizons t_{max}. The limited fidelity of motion predictions bounds this horizon, however, and allows thus for the implementation of such a heuristic in practice. In particular, we precompute offline a 5D Dijkstra search (2D position, heading, velocity, time) on our 4D lattice for every initial state (resulting in queries for heading-velocity combinations only, due to complete invariance in 2D translation, and partial invariance due to rotation). Edges surpassing a fixed time horizon (t_{max}, linked to the fidelity of motion predictions) are discarded. Expansion continues until there are no valid edges left on the queue. As a post-processing step, we perform an optimization to reduce memory usage: due to the lattice's discretization in position (0.1 m) and the robot's maximal velocity (1.0 m/s), a minimal uncertainty in time of 0.1 s results. We exploit this fact and *a posteriori* discretize the time dimension in 0.1 s intervals in order to merge states with identical rounded arrival times and identical predecessor edges together. We then arrive at a reduced size 6D look-up table of time-edge distinct states (see Fig. 2 for an illustration with $t_{max} = 4\,\text{s}$). This heuristic look-up table enables the planning algorithm to determine during search, whether a given expanded state is possibly within range of t_{max} of the search goal state, and if so, with which time instances it needs to be initialized so that it can reach the goal state at $t = 0.0\,\text{s}$.

C. MotionPredictions of Dynamic Obstacles

Predictions concerning the future motion of dynamic obstacles are challenging, as errors in the applied model unfavorably propagate through time. Nonetheless, in the future we would like to add prediction functionality to our model-based pedestrian detection and tracking module [20]. For the remainder of this paper we will assume perfect knowledge of the future motion of dynamic objects (up to t_{max}), however. This allows for a performance analysis in exclusion of artifacts due to motion prediction.

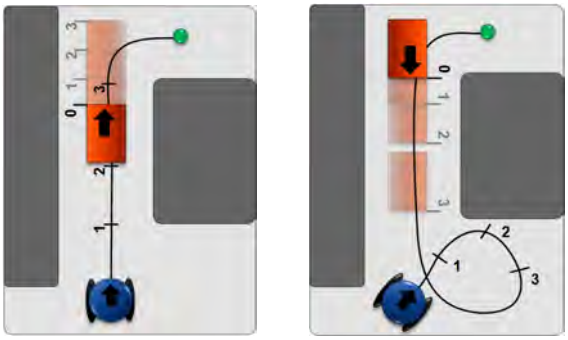

Fig. 3. Schematic of two dynamic scenes (left: scenario II, right: scenario III), where the 2D heuristic and the freespace heuristic are highly inaccurate. The number of state expansions required to find an optimal solution explodes.

D. Selected D* Function Annotations

The D* planning algorithm does not rely on any assumptions concerning the underlying graph but is commonly employed on a 2D grid. In this section we therefore describe adaptations to key functions necessary when planning with motion predictions on a state lattice (see Table II).

1) getTraversalCost(state pred, state succ): In our implementation, the total cost of motion between two states is comprised of a combination of *time of traversal* and *risk of collision* with dynamic obstacles (defined as impact · likelyhood of occupation). Online, risk is stored in a three-dimensional cost map (2D position, time), and updated by combining motion prediction with object labeling.

2) getHeuristicCost(state current): As described in Section II-B, we employ three complimentary heuristics. The heuristic estimate from a state *current* to the goal is then computed as the *maximal* value of the three individual heuristics.

3) getPred(state current): This function returns a list of predecessors of the current state, where predecessors are defined in a graph of directed edges between start and goal location. The introduction of bounded time into the state-space results in two classes of states: these with no time assigned (which signifies that they are not yet within t_{max} of the start configuration), and these associated with a time ε $[0, t_{max}]$. Predecessor expansion is thus divided into three cases:
Case 1: the current state has no time associated with it, and has no predecessors in the range of the time-viable heuristic. In this case, the number of predecessors is equal to the branching factor of the current state. Predecessors are assigned no time.
Case 2: the current state has no time associated with it, but some predecessors are in range of the time-viable heuristic, and thus of t_{max}. This is the most expensive case, as every predecessor in range of the time-viable heuristic is expanded with every stored arrival time at that state. The max. number of arrival times for different configurations is shown in Fig. 2.
Case 3: the current state has a time associated with it. This is the cheapest case, as then *at most* as many edges as the branching factor of the current state are returned.

4) getSucc(state current): This function returns a list of successors of the current state. Successors are assigned an arrival time if and only if the current state also has one assigned and it is lower than t_{max}.

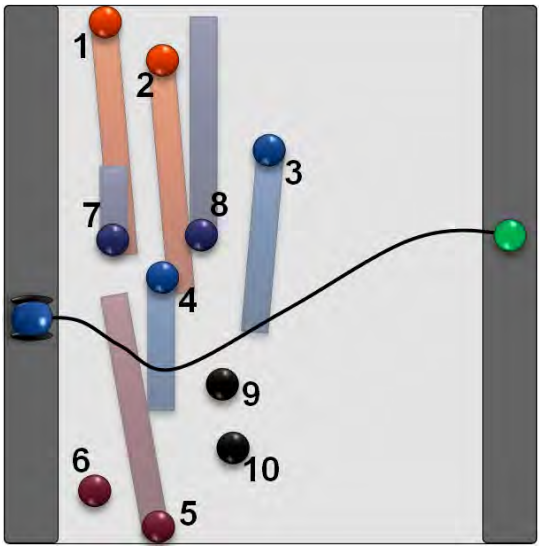

Fig. 4. Schematic of scenario I. An open, but dynamic space of 8x10 m is to be crossed by the robot.

III. Results

A. Complexity Analysis

In Section II-D we described three predecessor expansion cases, where the most expensive one is encountered while crossing the time-viable heuristic's border. In this situation, states with every possible arrival time below t_{max} are put on the priority queue, where they are collision checked against static and dynamic obstacles. These checks (see Table II.A) typically constitute the most costly part of the algorithm. It is thus of great interest to determine the average number of additional states placed on the priority queue relative to a forward searching implementation. Table I summarizes these results for time-viable heuristics of horizon 3.0 s, 3.5 s and 4.0 s, where the search is operated in freespace. It should be noted that in heuristic adverse scenarios, potentially many more crossings (and thus states pushed on the queue) are to be expected (see Section III-B, and Table III below).

B. Simulated Dynamic Scenarios

In this section we compare our high-dimensional D* algorithm to A* in several cluttered and dynamic scenarios. Both algorithms operate on the lattice presented in this paper, and perform cost checks in a dynamic cost field which is based on perfect motion predictions of dynamic objects up to a fixed time horizon (t_{max}). This approach allows us to analyze performance without potentially introducing bias due to inaccurate motion predictions. On the other hand, effects of interaction cannot be analyzed.

1) Scenario I: Scenario I is comprised of an open environment, where the only inaccuracies to the heuristics are due to pedestrians cluttering the scene. The same simulation is run with an increasingly higher number of pedestrians crossing the scene, thus increasing the complexity of the queries: for each query, pedestrians with numbers $n <=$sceneI.n are taken into account (for numbering, see Table IV and Fig. 4). The

t_{max} $[s]$:	3.0	3.5	4.0
mean	5.2	9.5	16.7
min	1	1	1
max	18	37	62

TABLE I
COMPLEXITY ANALYSIS: AVG. NO. OF ADDITIONAL STATES PLACED ON QUEUE PER EXPANDED NODE UNDER FREE-SPACE ASSUMPTION

robot is required to plan several motions from a random start configuration on the left border to a random goal state on the right border. Table IV shows, that for various prediction horizons and scene complexities, our D* implementation expands a similar number of states to reach the solution as A*. On the other hand, for harder problems, more states are placed on the heap, corresponding to many crossings of the time-viable heuristic's border. These heap placements are costly, as they go along with cost checks and priority queue percolates. In the future, we will attempt to approach this issue through parallelization.

2) Scenarios II & III: Scenarios II and especially III illustrate the need for accurate heuristics when employing high-dimensional heuristic search. Scene II is located in a complex narrow environment, where another (autonomous) vehicle is moving towards the top at a constant velocity of 0.5 m/s (see Fig. 3), and thus blocks the direct path to the goal (green dot). The freespace heuristic is inaccurate due to environmental constraints (walls). The 2D heuristic neglects dynamic obstacles and thus dramatically underestimates the cost to reach the goal. Nonetheless our planner is able to find a solution in fewer than 100 expansion steps.

Scene III is located in the same environment as scene II, except that a dynamic object now moves towards to bottom of the scene at variable speed. The resulting motion requires our vehicle to perform an extra loop to let the obstacle pass, and only then proceed to the goal (see Fig. 3). This extra loop results in many expanded states close to the start position, as the planner believes it is close to the solution, just to discover that at these arrival times, the start state is expected to be blocked by the dynamic object. With our current heuristics, computation of a solution requires > 10000 expansions, and is thus far from real-time. It should be noted that while D* completely fails in such a hard environment, a forward searching algorithm could potentially start executing *partial motions*, combined with frequent re-planning.

getTraversalCost(pred, succ)

```
01 cost = 0;
02 for(tIdx = pred.t; tIdx < succ.t; ++tIdx){
03    (xIdx,yIdx) ← getPosition(pred,succ,tIdx);
04    cost += risk(xIdx,yIdx,tIdx);
05 }
06 cost += timeOfTraversal(pred, succ);
07 return cost;
```

getHeuristicCost(s)

```
01 cost = max(2DHeur(s), freeSpaceHeur(s), timeViableHeur(s));
02 return cost;
```

getPred(s)

```
01 vector<state> allPred;
02 for(predIdx = 0; predIdx<predecessor(s.a,s.v).size(); ++predIdx){
03    pred = predecessor(s.a,s.v,predIdx); {
04    if (s.t == -1 && timeViableHeur(pred).size() != 0){
05       for(tvIdx = 0; tvIdx < timeViableHeur(pred).size(); ++tvIdx)
06          pred.t = timeViableHeur(pred,tvIdx);
07          allPred.push_back(pred);
08       }
09       pred.t = -1;
10       allPred.push_back(pred);
11    } else if (s.t == -1){
12       pred.t = -1;
13       allPred.push_back(pred);
14    } else{
15       pred.t = s.t-pred.tEdge;
16       if (pred.t ε timeViableHeur(pred)){
17          allPred.push_back(pred);
18       }
19    }
20 }
21 return allPred;
```

getSucc(s)

```
01 vector<state> allSucc;
02 for(succIdx = 0; succIdx<successor(s.a, s.v).size(); ++succIdx){
03    succ = successor(s.a,s.v,succIdx);{
04    if (s.t == -1){
05       succ.t = -1;
06       allSucc.push_back(succ);
07    } else{
08       succ.t = s.t + succ.tEdge;
09       allSucc.push_back(succ);
10    }
11 }
12 return allSucc;
```

TABLE II
SELECTED D* FUNCTION ANNOTATIONS

IV. CONCLUSIONS AND FUTURE WORK

In this paper we introduced a novel heuristic, the *time-viable heuristic*. It enables deterministic incremental planning algorithms to be employed in conjunction with motion predictions of dynamic obstacles which are thought to be necessary for planning better solutions in cluttered and dynamic scenes.

We have shown in scenarios of increasing complexity, that for our D* implementation the average number of expanded states is comparable to a forward searching A* query, despite the introduction of the time-viable heuristic. On the other hand, the number of states placed on the priority queue (resulting in priority queue percolates and cost checks, both of them costly operations) grows for our implementation substantially faster with environment complexity.

Future work will thus investigate two directions: first, we will attempt to further increase planning and re-planning speed through parallelization. Second, we will focus on designing more informed, environment aware heuristics in both static and dynamic constrained scenarios.

ACKNOWLEDGMENT

This work has been partially supported by the Swiss National Science Foundation NCCR MC3 and by the European Project EUROPA under contract number FP7-231888.

Scene	I.00		I.02		I.04		I.06		I.08		I.10	
Planner	A^*	D^*	A^*	D^*	A^*	D^*	A^*	D^*	A^*	D^*	A^*	D^*
Motion Prediction Time Bound: 4.0 s												
expansions												
mean	11	17	48	50	61	80	103	97	96	199	107	225
min	9	9	9	9	9	10	15	12	15	18	15	18
max	14	21	290	237	290	361	290	361	300	1684	300	1684
states on heap												
mean	248	145	457	426	601	1044	901	1160	915	3402	989	4782
Motion Prediction Time Bound: 3.5 s												
expansions												
mean	11	11	33	24	44	26	78	39	85	51	95	48
min	9	8	9	8	9	8	15	15	15	15	15	16
max	14	16	270	134	270	134	270	134	300	131	300	131
states on heap												
mean	248	207	416	267	579	284	917	486	976	512	1058	506
Motion Prediction Time Bound: 3.0 s												
expansions												
mean	11	11	30	29	37	29	44	33	50	47	50	47
min	9	8	9	8	9	8	9	8	9	8	9	8
max	14	16	270	261	270	261	270	261	247	233	247	233
states on heap												
mean	248	126	405	227	564	243	593	292	628	378	630	381

TABLE III

SCENARIO I: PERFORMANCE OVERVIEW

REFERENCES

[1] D. Ferguson, M. Likhachev, and A. Stentz. A guide to heuristic-based path planning. In *International Conference on Automated Planning and Scheduling (ICAPS)*, 2005.

[2] P. E. Hart, N. J. Nilsson, and B. Raphael. A formal basis for the heuristic determination of minimum cost paths. In *Autonomous Mobile Robots: Perception, Mapping, and Navigation (Vol. 1)*, pages 375–382, Los Alamitos, CA, 1991.

[3] M. Likhachev, G. Gordon, and S. Thrun. Ara*: Anytime a* with provable bound son sub-optimality. In *Advances in Neural Information Processing Systems, MIT Press*, 2003.

[4] S. Koenig and M. Likhachev. Improved fast replanning for robot navigation in unknown terrain. volume 1, pages 968–975 vol.1, 2002.

[5] I. Nesnas M. Pivtoraiko, T. Howard and A. Kelly. Field experiments in rover navigation via model-based trajectory generation and non-holonomic motion planning in state lattices. In *Proceedings of the 9th International Symposium on Artificial Intelligence, Robotics, and Automation in Space (i-SAIRAS '08)*, February 2008.

[6] R. A. Knepper M. Pivtoraiko and A. Kelly. *Differentially constrained mobile robot motion planning in state lattices*, 26(CMU-RI-TR-):308–333, March 2009.

[7] M. Likhachev and D. Ferguson. Planning long dynamically-feasible maneuvers for autonomous vehicles. In *Proceedings of the Robotics: Science and Systems Conference (RSS)*, 2008.

[8] D. Ferguson, T. Howard, and M. Likhachev. Motion Planning in Urban Environments: Part I. In *Proceedings of the IEEE/RSJ 2008 International Conference on Intelligent Robots and Systems*, September 2008.

[9] T. Howard D. Ferguson and M. Likhachev. Motion Planning in Urban Environments: Part II. In *Proceedings of the IEEE/RSJ 2008 International Conference on Intelligent Robots and Systems*, September 2008.

[10] M. Pivtoraiko and A. Kelly. Generating near minimal spanning control sets for constrained motion planning in discrete state spaces. In *Proceedings of the 2005 IEEE/RSJ International Conference on Intelligent Robots and Systems (IROS '05)*, pages 3231 – 3237, August 2005.

[11] M. Rufli, D. Ferguson, and R. Siegwart. Smooth path planning in constrained environments. In *Proceedings of the IEEE International Conference on Robotics and Automation (ICRA)*, 2009.

[12] R. Rosales and S. Sclaroff. Improved tracking of multiple humans with trajectory prediction and occlusion modeling. In *IEEE CVPR Workshop on the Interpretation of Visual Motion*, 1998.

[13] K. Han and M. Veloso. Physical model based multi-objects tracking and prediction in robosoccer. In *Working notes of the AAAI 1997 Fall Symposium on Model-directed Autonomous Systems*, Boston (US), November 1997.

[14] M. Bennewitz, W. Burgard, G. Cielniak, and S. Thrun. Learning motion patterns of people for compliant robot motion. *Internationl Journal of Robotics Research*, 24(1):31–48, January 2005.

[15] W. Hu, X. Xiao, Z. Fu, D. Xie, T. Tan, and S. Maybank. A system for learning statistical motion patterns. *IEEE Transactions on Pattern Analysis and Machine Intelligence*, 28(9):1450–1464, September 2006.

[16] L. Liao, D. Fox, and H. Kautz. Learning and inferring transportation routines. In *Proc. of the National Conf. on Artificial Intelligence AAAI-04*, 2004.

[17] A. Kushleyev and M. Likhachev. Time-bounded lattice for efcient planning in dynamic environments. In *Proceedings of the IEEE International Conference on Robotics and Automation (ICRA)*, 2009.

[18] E. W. Dijkstra. A note on two problems in connexion with graphs. *Numerische Mathematik*, 1:269–271, 1959.

[19] R. A. Knepper and A. Kelly. High performance state lattice planning using heuristic look-up tables. In *2006 IEEE/RSJ International Conference on Intelligent Robots and Systems*, pages 3375 – 3380, October 2006.

[20] L. Spinello, R. Triebel, and R. Siegwart. Multimodal detection and tracking of pedestrians in urban environments with explicit ground plane extraction. In *Proc. of The IEEE/RSJ International Conference on Intelligent Robots and Systems (IROS)*, 2008.

Eidgenössische Technische Hochschule Zürich
Swiss Federal Institute of Technology Zurich

Institute for
Dynamic Systems and Control
IDSC
Institut für Dynamische Systeme
und Regelungstechnik

Stephan Pleines

Report

Institute for Dynamic Systems and Control
Eidgenössische Technische Hochschule (ETH) Zürich

January 25, 2011

Contents

Chapter 1

Introduction

This report presents extensions to the optimal emergency maneuvers investigated in [1]. Those can be split into the following categories: Improvements in terms of solving the problems numerically, increased insight into the problems from a mathematical point of view, investigations on the influence of the characteristics of the tire, investigations on the influence of active tires.

The reader is assumed to be familiar with [1], as terms used in this work will be used here without explanation.

1.1 Additions to the Problem Definitions

For some emergency maneuvers, the definitions of the corresponding optimal control problems were incomplete. Additions are made where necessary. See Chapter 2.

1.2 Solving the Optimal Control Problems Numerically

All problems were originally solved numerically. While some can now be solved analytically, the majority is extremely hard if not impossible to solve analytically. Some improvements were made on the numerical solution. See Chapter 3.

1.3 Analytical Solution for the Obstacle Avoidance Maneuver

The problem obstacle avoidance maneuver was solved analytically for the vehicle with rear wheel steering. It confirms the previously found numerical solution. See Chapter 4.

1.4 Influence of Tire Characteristics

For the example of the obstacle avoidance maneuver, it was investigated how a change for the tire characteristics influences the maneuverability. Changing the maximum coefficient of friction has a big influence as can be expected, changing the cornering stiffness however has almost no influence. See Chapter 5.

1.5 Influence of Active Tires

For the example of the obstacle avoidance maneuver, it was investigated how changing the cornering stiffness during the maneuver influence the maneuverability. There is almost on influence. See Chapter 6.

Chapter 2

Additions to the Problem Definitions

All optimal control problems presented in [1] suffer from a common problem: There are no state constraints. An intuitive example is the obstacle avoidance maneuver. The final lateral displacement could be reached by performing the following maneuver: Turn right until the vehicle is going in negative x direction, keep going for an infinite amount of time, then turn right again to reach the desired displacement. The optimization criterion now is $-\infty$.

Correct problem definitions using the notation of [2] are presented below. It should be pointed out that the solutions presented in [1] are the solutions to the below problems, they are respecting the state constraints. In [1], they are however not mentioned.

2.1 Obstacle Avoidance

Pro memoria:

$$x = \begin{bmatrix} x & y & \varphi & \dot{x} & \dot{y} & \dot{\varphi} \end{bmatrix}^{\mathrm{T}}.$$

Find a piecewise continuous control $u : [0, t_{\mathrm{f}}] \to \Omega \subseteq \mathbb{R}^m$, such that the constraints

$$\begin{aligned} x(0) &= \begin{bmatrix} 0 & 0 & 0 & v & 0 & 0 \end{bmatrix}^{\mathrm{T}} \\ \dot{x}(t) &= f\big(x(t), u(t)\big) \qquad \forall\, t \in [0, t_{\mathrm{f}}] \\ x(t) &\in \Omega_x \qquad \forall\, t \in [0, t_{\mathrm{f}}] \\ x(t_{\mathrm{f}}) &\in S \end{aligned}$$

are satisfied and such that the cost functional

$$J(u) = x_1(t_{\mathrm{f}})$$

is minimized and the final time t_f is free. The subset containing the final state is

$$S = \{\, x \mid x_2 = y_\mathrm{f} > 0 \,\}.$$

The subset containing the state at all times is

$$\Omega_x = \{\, x \mid x_2 \gneqq 0,\ x_4 > 0 \,\}. \tag{2.1}$$

The function $f(x, u)$ depends on the vehicle investigated, as does the dimension of the input signal m and the subset of allowed inputs Ω.

2.1.1 Remarks on the State Constraints

The effect of the newly introduced state constraint Equation (2.1) is the following: The vehicle cannot stop in longitudinal direction ($x_4 > 0$) or (turn around) and go backwards in longitudinal direction. Would the vehicle be allowed to stop, it could stop for an undefined amount of time, then travel laterally until it reaches the final state in any which way. The problem would not be well defined. Would the vehicle in addition be allowed to turn around, it could reach the final state at any longitudinal position, making the cost criterion tend towards negative infinity. Even more scenarios can thought of when the vehicle is allowed to enter the second quadrant.

Also, y_f may not exceed a certain critical maximum value for the problem to be meaningful. If the vehicle would turn around to the left with maximum effort and turn so far that it reaches a longitudinal velocity just greater than zero, the problem might be well defined – but meaningless.

The constraint on x_4 ($\gneqq$, not $\geq$) cannot be respected with the optimal control theory known to the author, should x_4 ever reach the boundary of the permissible subset – the subset is open, not closed.

Requiring that $x_4(t) > 0\ \forall\, t \in [0, t_\mathrm{f}]$ will cause $x_1(t_f) > 0$.

2.2 Lane Change

Find a piecewise continuous control $u : [0, t_\mathrm{f}] \to \Omega \subseteq \mathbb{R}^m$, such that the constraints

$$\begin{aligned} x(0) &= \begin{bmatrix} 0 & 0 & 0 & v & 0 & 0 \end{bmatrix}^\mathrm{T} \\ \dot{x}(t) &= f\big(x(t), u(t)\big) \qquad \forall\, t \in [0, t_\mathrm{f}] \\ x(t) &\in \Omega_x \qquad \forall\, t \in [0, t_\mathrm{f}] \\ x(t_\mathrm{f}) &\in S \end{aligned}$$

are satisfied and such that the cost functional

$$J(u) = x_1(t_\mathrm{f})$$

is minimized and the final time t_f is free. The subset containing the final state is

$$S = \{\, x \mid x_2 = y_\mathrm{f} > 0,\ x_3 = x_5 = x_6 = 0 \,\}\,.$$

The subset containing the state at all times is

$$\Omega_x = \{\, x \mid x_2 \geqslant 0,\ x_4 > 0 \,\}\,. \tag{2.2}$$

The function $f(x, u)$ depends on the vehicle investigated, as does the dimension of the input signal m and the subset of allowed inputs Ω.

The remarks from Chapter 2.1.1 apply to this problem as well.

2.3 Barrier Avoidance

The problem as state in [1] is meaningful only if the vehicle is initially traveling in direction of the barrier.

2.4 Recovery

There could be multiple solutions depending on the initial conditions.

2.5 Full Avoidance Maneuver

The cost criterion mixes different units.

Chapter 3

Solving the Optimal Control Problems Numerically

Various changes were made to the MATLAB code that accompanied [1]. The ones with the biggest impact were:

- Automated saving of results in `.mat` files without danger of overwriting previous results. Automated loading of previous results for refining.
- For some maneuvers, guessing both the final time and initial costates is unnecessary. For some choice of initial costates, the system will reach the final state. One can just run the simulation until the final state is reached, then see what the final time is. This increases the convergence speed.
- Only one file is used to compute the evolution of the equations of motion. Originally, multiple files were used in different situations. The convenience for the user is increased while the speed of the simulation is kept constant.
- Multiple unnecessary calculation steps are omitted, other calculations are sped up by simplifying especially long terms.

Chapter 4

Analytical Solution for the Obstacle Avoidance Maneuver

This chapter presents an analytical solution for the barrier avoidance problem for a vehicle with rear wheel steering, with and without weight shift effect.

4.1 Original Optimal Control Problem

The problem can be described as follows: For a single track model of a car with front and rear wheel steering (we can pick the longitudinal and lateral forces within the limits of friction) which includes weight shift, find the input that makes the vehicle travel laterally a distance d ($d = y_\mathrm{f}$ in Chapter 2) such that the distance traveled longitudinally by the time it reaches the desired lateral displacement is minimized, while making sure that we always travel forwards longitudinally.

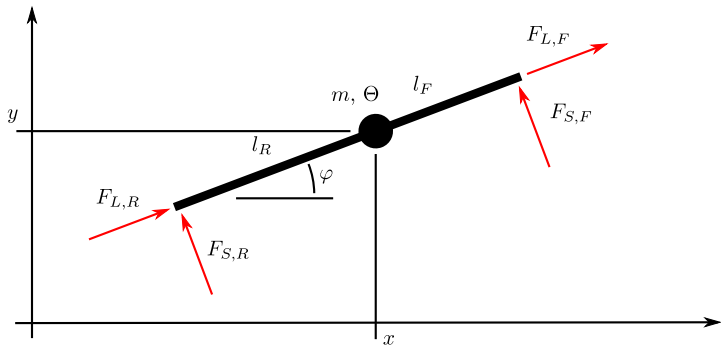

Figure 4.1: Sketch of the original problem.

A sketch of the problem can be seen in Figure 4.1. In the following, the state is defined

$$x = \begin{bmatrix} x & y & \varphi & \dot{x} & \dot{y} & \dot{\varphi} \end{bmatrix}^{\mathrm{T}},$$

and the input

$$u = \begin{bmatrix} F_{\mathrm{L,F}} \\ F_{\mathrm{S,F}} \\ F_{\mathrm{L,R}} \\ F_{\mathrm{S,R}} \end{bmatrix}.$$

Where L means longitudinal, S sideways or lateral, F front and R rear.

The problem can now be stated as: Find a piecewise continuous control

$$u : [0, t_{\mathrm{f}}] \to \Omega \subseteq \mathbb{R}^2$$

where the final time t_{f} is free and $\mu = 1$ f.t.s.o.s. and

$$\Omega = \Big\{ u \;\Big|\; \sqrt{u_1^2 + u_2^2} \leqslant \frac{1}{l_{\mathrm{R}} + l_{\mathrm{F}}} \big(g\, l_{\mathrm{R}}\, m - h\,(u_1 + u_3) \big), \\ \sqrt{u_3^2 + u_4^2} \leqslant \frac{1}{l_{\mathrm{R}} + l_{\mathrm{F}}} \big(g\, l_{\mathrm{F}}\, m + h\,(u_1 + u_3) \big) \Big\},$$

such that the constraints

$$x(0) = \begin{bmatrix} 0 & 0 & 0 & v & 0 & 0 \end{bmatrix}^{\mathrm{T}},$$

$$\dot{x}(t) = \begin{bmatrix} x_4(t)\, \cos x_3(t) - x_5\, \sin x_3(t) \\ x_4(t)\, \sin x_3(t) - x_5\, \cos x_3(t) \\ x_6(t) \\ \big(u_1(t) + u_3(t)\big)\, m^{-1} + x_5(t)\, x_6(t) \\ \big(u_2(t) + u_4(t)\big)\, m^{-1} - x_4(t)\, x_6(t) \\ \big(l_{\mathrm{F}}\, u_2(t) - l_{\mathrm{R}}\, u_4(t)\big)\, \Theta^{-1} \end{bmatrix} \quad \forall\, t \in [0, t_{\mathrm{f}}],$$

$$x(t_{\mathrm{f}}) \in S, \quad S = \{\, x \mid x_2 = d \,\},$$

$$x(t) \in \Omega_x, \quad \Omega_x = \{\, x \mid x_2 \geqslant 0,\ x_4 > 0 \,\},$$

are satisfied and the cost functional

$$J(u) = K\big(x(t_{\mathrm{f}})\big) = x_1(t_{\mathrm{f}})$$

is minimized.

Note: The following holds: $m > 0$, $\Theta > 0$, $l_{\mathrm{R}} > 0$, $l_{\mathrm{F}} > 0$.

Ω_x makes sure that we evade to the left and do not "turn around". Compare Chapter 2.1.1.

The Hamiltonian for this problem is:

$$H\big(x(t), \lambda(t), u(t)\big) = (x_4\, \cos x_3 - x_5\, \sin x_3)\, \lambda_1 + (x_4\, \sin x_3 + x_5\, \cos x_3)\, \lambda_2 \\ + x_6\, \lambda_3 + \left(\frac{u_1 + u_3}{m} + x_5\, x_6 \right) \lambda_4 + \left(\frac{u_2 + u_4}{m} - x_4\, x_6 \right) \lambda_5 + \frac{l_{\mathrm{F}}\, u_2 - l_{\mathrm{R}}\, u_4}{\Theta}\, \lambda_6.$$

The costate satisfies

$$\begin{aligned}\dot{\lambda}(t) &= -\nabla_x H\big(x(t), \lambda(t), u(t)\big) \\ &= \begin{bmatrix} 0 \\ 0 \\ (x_4 \sin x_3 + x_5 \cos x_3)\,\lambda_1 - (x_4 \cos x_3 - x_5 \sin x_3)\,\lambda_2 \\ -\lambda_1 \cos x_3 - \lambda_2 \sin x_3 + x_6\,\lambda_5 \\ \lambda_1 \sin x_3 - \lambda_2 \cos x_3 - x_6\,\lambda_4 \\ -\lambda_3 - x_5\,\lambda_4 + x_4\,\lambda_5 \end{bmatrix}\end{aligned}$$

with final condition

$$\lambda(t_\mathrm{f}) = \nabla_x K\big(x(t_\mathrm{f})\big) + q,$$

where

$$q \in T^*\big(S, x(t_\mathrm{f})\big),$$

and T^* is the normal cone of the tangent cone of S at $x(t_\mathrm{f})$:

$$T^*\big(S, x(t_\mathrm{f})\big) = \{\, \lambda \mid \lambda_1 = 0,\ \lambda_2 \neq 0,\ \lambda_3 = 0,\ \lambda_4 = 0,\ \lambda_5 = 0,\ \lambda_6 = 0 \,\},$$

so

$$\lambda(t_f) = \begin{bmatrix} 1 & k & 0 & 0 & 0 & 0 \end{bmatrix}^\mathrm{T}$$

with $k \in \mathbb{R}$, $k \neq 0$.

Therefore $\lambda_1(t) \equiv 1$, $\lambda_2(t) \equiv k$.

4.2 Simplified Optimal Control Problem

The problem stated above can be simplified to the following simpler problem: A body with mass m and some inertia, with forces F_x and F_y acting on the center of mass in x and y direction of the inertial coordinate system, as well

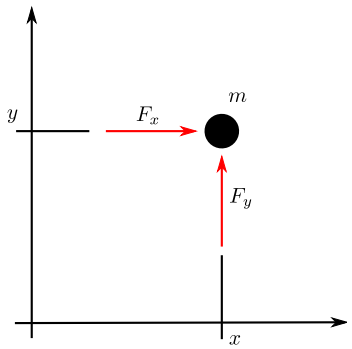

Figure 4.2: Sketch of the simplified problem.

as some torque. A sketch of the problem can be seen in Figure 4.2. The forces F_x, F_y relate to the forces u of the above problem as follows:

$$\begin{bmatrix} F_x \\ F_y \end{bmatrix} = \begin{bmatrix} \cos\varphi & -\sin\varphi \\ \sin\varphi & \cos\varphi \end{bmatrix} \left(\begin{bmatrix} u_1 \\ u_2 \end{bmatrix} + \begin{bmatrix} u_3 \\ u_4 \end{bmatrix} \right),$$

therefore

$$\left|\left| \begin{bmatrix} F_x \\ F_y \end{bmatrix} \right|\right| = \left|\left| \begin{bmatrix} u_1 \\ u_2 \end{bmatrix} + \begin{bmatrix} u_3 \\ u_4 \end{bmatrix} \right|\right|,$$

so the magnitude of the total force $\sqrt{F_x^2 + F_y^2}$ is bounded to $m\,g$ since

$$\begin{aligned} \sqrt{u_1^2 + u_2^2} + \sqrt{u_3^2 + u_4^2} \leqslant \frac{1}{l_\mathrm{R} + l_\mathrm{F}} \left(g\, l_\mathrm{R}\, m - h\,(u_1 + u_3) \right) \\ + \frac{1}{l_\mathrm{R} + l_\mathrm{F}} \left(g\, l_\mathrm{F}\, m + h\,(u_1 + u_3) \right) = m\, g \end{aligned}$$

There is also some torque $(u_2\, l_\mathrm{F} - u_4\, l_\mathrm{R})$, resulting in some evolution of φ. However, we do not care about φ and can produce any forces F_x, F_y independent of φ. The mapping from F_x, F_y to u exists, but is far too space consuming to be included in this document. It can be found in [3]. It is interesting to note that (at least for some problems) the vehicle with weight shift effect can generate the same resulting force as the vehicle without weight shift effect, although the momentum will be different.

The state is defined

$$\bar{x}(t) = \begin{bmatrix} x(t) & y(t) & \dot{x}(t) & \dot{y}(t) \end{bmatrix}^\mathrm{T}.$$

Therefore, the following equivalent problem can be formulated: Find

$$\bar{u} : [0, t_\mathrm{f}] \to \Omega \subseteq \mathbb{R}^2$$

where the final time t_f is free and

$$\Omega = \left\{ \bar{u} \;\middle|\; \bar{u}_1^2 + \bar{u}_2^2 \leqslant g^2 \right\},$$

such that the constraints

$$\begin{aligned} \bar{x}(0) &= \begin{bmatrix} 0 & 0 & v & 0 \end{bmatrix}^\mathrm{T}, \\ \dot{\bar{x}}(t) &= \begin{bmatrix} \bar{x}_3(t) & \bar{x}_4(t) & \bar{u}_1(t) & \bar{u}_2(t) \end{bmatrix}^\mathrm{T}, \\ \bar{x}(t) \in \Omega_{\bar{x}}, &\quad \Omega_{\bar{x}} = \left\{ \bar{x} \mid \bar{x}_2 \geqslant 0,\ \bar{x}_3 > 0 \right\}, \\ \bar{x}(t_\mathrm{f}) \in S, &\quad S = \left\{ \bar{x} \mid \bar{x}_2(t_\mathrm{f}) = d \right\}, \end{aligned}$$

are satisfied and the cost functional

$$J = K\big(\bar{x}(t_\mathrm{f})\big) = \bar{x}_1(t_\mathrm{f})$$

is minimized.

4.2.1 Solution

The Hamiltonian is

$$\bar{H}(\bar{x}(t), \bar{\lambda}(t), \bar{u}(t)) = \bar{\lambda}_1(t)\,\bar{x}_3(t) + \bar{\lambda}_2(t)\,\bar{x}_4(t) + \bar{\lambda}_3(t)\,\bar{u}_1(t) + \bar{\lambda}_4(t)\,\bar{u}_2(t).$$

The costate satisfies

$$\dot{\bar{\lambda}}(t) = -\nabla_{\bar{x}}\bar{H}\big(\bar{x}(t), \bar{\lambda}(t), \bar{u}(t)\big) = \begin{bmatrix} 0 \\ 0 \\ -\bar{\lambda}_1(t) \\ -\bar{\lambda}_2(t) \end{bmatrix},$$

and

$$\bar{\lambda}(t_\mathrm{f}) = \nabla_{\bar{x}} K\big(\bar{x}(t_\mathrm{f})\big) + q,$$

where

$$q \in T^*\big(S, \bar{x}(t_\mathrm{f})\big),$$

and T^* is the normal cone of the tangent cone of S at $\bar{x}(t_\mathrm{f})$:

$$T^*\big(S, \bar{x}(t_\mathrm{f})\big) = \left\{\, \bar{\lambda} \mid \bar{\lambda}_1 = 0,\, \bar{\lambda}_2 \neq 0,\, \bar{\lambda}_3 = 0,\, \bar{\lambda}_4 = 0 \,\right\}.$$

Therefore

$$\bar{\lambda}(t_\mathrm{f}) = \begin{bmatrix} 1 & c & 0 & 0 \end{bmatrix},$$

with any $c \in \mathbb{R}$, $c \neq 0$. The evolution of the costate is (obviously)

$$\bar{\lambda}(t) = \begin{bmatrix} 1 \\ c \\ t_\mathrm{f} - t \\ (t_\mathrm{f} - t)\,c \end{bmatrix}.$$

The Hamiltonian now becomes

$$\bar{H}\big(\bar{x}(t), v(t), t\big) = \bar{x}_3(t) + c\,\bar{x}_4(t) + (t_\mathrm{f} - t)\,\big(\bar{u}_1(t) + c\,\bar{u}_2(t)\big).$$

Minimizing the Hamiltonian is a static optimization problem that is to be solved at each time instance t: Minimize $\bar{H}\big(\bar{x}(t), \bar{u}(t), t\big)$ over $\bar{u}(t)$ subject to $\bar{u}_1^2 + \bar{u}_2^2 \leqslant g^2$. $\bar{H}$ is a hyperplane. The minimum is unique (for $t \neq t_\mathrm{f}$) and lies at the boundary of the permissible region of $\bar{u}$, hence the constraint is active. We can introduce Lagrange multipliers ν and state the following problem: Minimize

$$F(\bar{u}_1, \bar{u}_2, \nu) = \bar{x}_3 + c\,\bar{x}_4 + (t_\mathrm{f} - t)\,(\bar{u}_1 + c\,\bar{u}_2) + \nu\left(\bar{u}_1^2 + \bar{u}_2^2 - g^2\right).$$

Setting the following derivatives equal to 0

$$\frac{\partial}{\partial \nu} F = \bar{u}_1^2 + \bar{u}_2^2 - g^2 = 0$$

$$\frac{\partial}{\partial \bar{u}_1} F = (t_\mathrm{f} - t) + 2\,\nu\,\bar{u}_1 = 0$$

$$\frac{\partial}{\partial \bar{u}_2} F = (t_\mathrm{f} - t) + c\,2\,\nu\,\bar{u}_2 = 0$$

yields

$$\nu = \pm\frac{\sqrt{1+c^2}\,(t_\mathrm{f}-t)}{2\,g}$$
$$\bar{u}_1 = -\frac{t_\mathrm{f}-t}{2\,\nu} = \pm\frac{g}{\sqrt{1+c^2}}$$
$$\bar{u}_2 = -c\,\frac{t_\mathrm{f}-t}{2\,\nu} = \pm\frac{c\,g}{\sqrt{1+c^2}}.$$

We know from our understanding of the problem that we have to pick $\bar{u}_1 < 0$ and $\bar{u}_2 > 0$, because we constrain $x_2 \geqslant 0$. Therefore we pick

$$\nu = -\frac{\sqrt{1+c^2}\,(t_\mathrm{f}-t)}{2\,g}$$

and get

$$\bar{u}_1 = -\frac{g}{\sqrt{1+c^2}}$$
$$\bar{u}_2 = -\frac{c\,g}{\sqrt{1+c^2}}$$

and conclude that $c < 0$ must hold. We also see that $c = \frac{\bar{u}_2}{\bar{u}_1}$ holds.

We can also compute the final time t_f using a result stated below:

$$\bar{x}_2(t_\mathrm{f}) = d = \frac{\bar{u}_2\,t_\mathrm{f}^2}{2} \Rightarrow t_\mathrm{f} = \sqrt{\frac{2\,d}{\bar{u}_2}}.$$

So the optimal input (as long as the state constraint does not become active) is constant, but we do not know its exact value, since we do not know c.

4.3 Simplified problem - minimization problem

Knowing that the input is constant, we can calculate the trajectory of the point mass explicitly, and then minimize our original cost functional.

The initial and final conditions are

$$\underline{x}(0) = \begin{bmatrix} 0 & 0 & v & 0 \end{bmatrix}^\mathrm{T},$$
$$\underline{x}(t_\mathrm{f}) \in S, \quad S = \{\, \underline{x} \mid \underline{x}_2(t_\mathrm{f}) = d \,\}.$$

And the dynamics are

$$\dot{\underline{x}}(t) = \begin{bmatrix} \underline{x}_3(t) \\ \underline{x}_4(t) \\ -\sqrt{g^2 - \underline{u}^2} \\ \underline{u} \end{bmatrix}.$$

Pro memoria: $v > 0$, $d > 0$, $0 \leqslant \underline{u} \leqslant g$.

4.3.1 Trajectory

It follows that

$$\underline{x}(t) = \begin{bmatrix} v\,t - \frac{1}{2}\sqrt{g^2 - \underline{u}^2}\,t^2 \\ \frac{\underline{u}\,t^2}{2} \\ v - \sqrt{g^2 - \underline{u}^2}\,t \\ \underline{u}\,t \end{bmatrix}.$$

At the final time t_f the following holds

$$\underline{x}_2(t_\mathrm{f}) = d = \frac{\underline{u}\,t_\mathrm{f}^2}{2} \Rightarrow t_\mathrm{f} = \sqrt{\frac{2\,d}{\underline{u}}}.$$

In order for t_f to be finite, $0 < \underline{u}$ must hold. In other words: We need to apply some force in y direction to reach $y = d$.

4.3.2 The optimization problem

We now know the trajectory and final time as functions of v, d, g, and $\underline{u}$. We seek the $\underline{u}$ that minimizes the maximum of $\underline{x}_2(t)$ over the time interval of interest, or more precisely we seek

$$\arg \min_{\underline{u} \in (0,g]} \max_{t \in [0,t_\mathrm{f}]} \underline{x}_1(t).$$

4.3.3 $\max_{t\in[0,t_\mathrm{f}]} \underline{x}_1(t)$

The maximum must be either at the boundaries of the interval $t = 0$, $t = t_\mathrm{f}$, or somewhere within the interval.

The values at the boundaries of the interval are

$$\underline{x}_1(0) = 0,$$

$$\underline{x}_1(t_\mathrm{f}) = v\sqrt{\frac{2\,d}{\underline{u}}} - \frac{d}{\underline{u}}\sqrt{g^2 - \underline{u}^2}.$$

If an extremum exists within the interval, it must hold that

$$\dot{\underline{x}}_1(t) = \underline{x}_3(t) = v - \sqrt{g^2 - \underline{u}^2}\,t = 0,$$

which is true for

$$t_\mathrm{max} = \frac{v}{\sqrt{g^2 - \underline{u}^2}}, \quad \underline{u} < g.$$

If $\underline{u} = g$, the maximum must lie on the boundaries (at $\underline{x}(t_\mathrm{f})$) of the interval, since the speed in $\underline{x}$-direction will never decrease if $\underline{u} = g$.

The extremum at t_max will be a maximum since

$$\ddot{\underline{x}}_1(t) = \dot{\underline{x}}_3(t) = -\sqrt{g^2 - \underline{u}^2} < 0.$$

This maximum is the global maximum over t. It is:

$$\underline{x}_1(t_{\max}) = \frac{v^2}{2\sqrt{g^2 - \underline{u}^2}} > 0.$$

and it lies within the time interval of interest only if

$$0 < t_{\max} < t_{\mathrm{f}}$$

which holds only for

$$\underline{u} < \hat{u} = \frac{1}{4}\left(\sqrt{16\,g^2 + \frac{v^4}{d^2}} - \frac{v^2}{d}\right).$$

Note: $0 < \hat{u} < g$ holds.

If the global maximum is not within the interval, we need

$$\max\left\{\underline{x}_1(0), \underline{x}_1(t_{\mathrm{f}})\right\} = \begin{cases} \underline{x}_1(t_{\mathrm{f}}) & \text{if } \tilde{u} < \underline{u} \\ \underline{x}_1(0) & \text{otherwise} \end{cases}$$

where

$$0 < \tilde{u} = -\frac{v^2}{d} + \sqrt{g^2 + \frac{v^4}{d^2}} < g.$$

That means that if $\underline{u}$ is smaller $\tilde{u}$, the final x-position will be smaller than 0.

Since $\tilde{u} < \hat{u}$ we can conclude that

$$\max_{t\in[0,t_{\mathrm{f}}]} \underline{x}_1(t) = \begin{cases} \underline{x}_1(t_{\max}) & \text{if } 0 < \underline{u} < \hat{u} \\ \underline{x}_1(t_{\max}) = \underline{x}_1(t_{\mathrm{f}}) & \text{if } \underline{u} = \hat{u} \\ \underline{x}_1(t_{\mathrm{f}}) & \text{if } \hat{u} < \underline{u} \leqslant g \end{cases}.$$

In other words: If $\underline{u}$ is smaller than $\hat{u}$, we start moving backwards in x-direction before we hit the desired displacement. Reaching the desired displacement becomes rather meaningless then. Also, if $\underline{u} < \hat{u}$, we violate the constraint $x_3 > 0$ of the original problem.

4.3.4 $\min_{\underline{u}\in(0,g]} \max_{t\in[0,t_{\mathrm{f}}]} \underline{x}_1(t)$

Now, we seek to minimize this maximum over $\underline{u}$. Therefore we minimize $\underline{x}_1(t_{\max})$ and $\underline{x}_1(t_{\mathrm{f}})$ individually and then compare them.

4.3.4.1 $\min_{\underline{u}\in(0,g]} \underline{x}_1(t_{\mathbf{max}})$

First we seek

$$\min_{\underline{u}\in(0,\hat{u}]} \underline{x}_1(t_{\max}) = \min_{\underline{u}\in(0,\hat{u}]} \frac{v^2}{2\sqrt{g^2 - \underline{u}^2}}.$$

The minimum must lie at the boundaries, since

$$\frac{\mathrm{d}}{\mathrm{d}\underline{u}} \frac{v^2}{2\sqrt{g^2 - \underline{u}^2}} = \frac{\underline{u}\, v^2}{2\,(g^2 - \underline{u}^2)^{\frac{3}{2}}} \neq 0 \quad \forall\, \underline{u} \in (0, \hat{u}].$$

As $\underline{u}$ approaches the lower boundary:

$$\lim_{\underline{u} \to 0^+} \frac{v^2}{\sqrt{g^2 - \underline{u}^2}} = \frac{v^2}{2\,g}$$

At the upper boundary:

$$\underline{x}_1(t_{\max})\Big|_{\underline{u}=\hat{u}} = \frac{\sqrt{2}\, d\, v}{\sqrt{\sqrt{16\, d^2\, g^2 + v^4} - v^2}}$$

Since

$$\frac{v^2}{2\,g} < \frac{\sqrt{2}\, d\, v}{\sqrt{\sqrt{16\, d^2\, g^2 + v^4} - v^2}}$$

the minimum is

$$\min_{\underline{u} \in (0, \hat{u})} \underline{x}_1(t_{\max}) \to \frac{v^2}{2\,g} \quad \text{as} \quad \underline{u} \to 0^+.$$

Note: We already know that for $\underline{u} < \hat{u}$, we will violate the constraint $x_3 > 0$, meaning we will turn around before reaching the desired displacement. In this case it is obviously best to chose $\underline{u}$ as small as possible.

4.3.4.2 $\min_{\underline{u} \in (0, g]} \underline{x}_1(t_\mathrm{f})$

Now seek

$$\min_{\underline{u} \in [\hat{u}, g]} \underline{x}_1(t_\mathrm{f}) = \min_{\underline{u} \in [\hat{u}, g]} v \sqrt{\frac{2\, d}{\underline{u}}} - \frac{d}{\underline{u}} \sqrt{g^2 - \underline{u}^2}.$$

At the lower boundary we get

$$\underline{x}_1(t_\mathrm{f})\Big|_{\underline{u}=\hat{u}} = \underline{x}_1(t_{\max})\Big|_{\underline{u}=\hat{u}} = \frac{\sqrt{2}\, d\, v}{\sqrt{\sqrt{16\, d^2\, g^2 + v^4} - v^2}}$$

At the upper boundary we get

$$\underline{x}_1(t_\mathrm{f})\Big|_{\underline{u}=g} = v \sqrt{\frac{2\, d}{g}}.$$

The last possibility is that the minimum lies within the interval. Then

$$\frac{\mathrm{d}}{\mathrm{d}\underline{u}} \left(v \sqrt{\frac{2\, d}{\underline{u}}} - \frac{d}{\underline{u}} \sqrt{g^2 - \underline{u}^2} \right) = \frac{d\, g^2}{\underline{u}^2 \sqrt{g^2 - \underline{u}^2}} - \sqrt{\frac{d}{2\,\underline{u}}}\, \frac{v}{\underline{u}} = 0.$$

Which can be rearranged to

$$\underline{u}^3\, v^2 - \underline{u}\, v^2\, g^2 + d\, g^4\, 2 = 0. \tag{4.1}$$

The three solutions are

$$\begin{aligned}
\underline{u}_1 &= \frac{3^{\frac{1}{3}}\, g^2\, v^4 + b^{\frac{2}{3}}}{3^{\frac{2}{3}}\, v^2\, b^{\frac{1}{3}}} \\
\underline{u}_2 &= \frac{(-1)^{\frac{2}{3}}\, b^{\frac{2}{3}} - (-3)^{\frac{1}{3}}\, g^2\, v^4}{3^{\frac{2}{3}}\, b^{\frac{1}{3}}\, v^2} \\
\underline{u}_3 &= \frac{-(-3)^{\frac{1}{3}}\, b^{\frac{2}{3}} + (-3)^{\frac{2}{3}}\, g^2\, v^4}{3\, b^{\frac{1}{3}}\, v^2}
\end{aligned}$$

where

$$\begin{aligned}
b &= -9\, d\, g^4\, v^4 + \sqrt{81\, d^2\, g^8\, v^8 - 3\, g^6\, v^{12}} \\
&= g^3\, v^4 \left(-9\, d\, g + \sqrt{9^2\, d^2\, g^2 - 3\, v^6}\right).
\end{aligned}$$

Note that the root in b will vanish if

$$d = \frac{v^2}{3\sqrt{3}\, g} = d_b(v, g)$$

and then b becomes

$$b = -\sqrt{3}\, g^3\, v^6.$$

The root will be real if $d > d_b$.

Further analytic statements are hard to make. Numerically, the following can be shown though (for $v > 0$, $d > 0$, $g > 0$):

- $\underline{u}_2$ is always real, but negative, and hence not the solution we are looking for.
- $\underline{u}_1$ and $\underline{u}_3$ have real parts that are strictly positive.
- for $d \leqslant d_b$, $\underline{u}_1$ and $\underline{u}_3$ are real and

$$0 < \underline{u}_3 \leqslant \frac{g}{\sqrt{3}} \leqslant \underline{u}_1 < g.$$

- for $d \geqslant d_b$, $\underline{u}_1$ and $\underline{u}_3$ are complex and $\mathrm{Re}(\underline{u}_1) = \mathrm{Re}(\underline{u}_2)$ and $\mathrm{Im}(\underline{u}_1) = -\mathrm{Im}(\underline{u}_2)$.
- $\underline{u}_1$ is indeed the solution we are looking for. The minimum $\underline{x}_1(t_\mathrm{f}, \underline{u}_1)$ is smaller than $\min_{\underline{u}\in(0,\hat{u})} \underline{x}_1(t_\mathrm{max}, \underline{u} \to 0)$ for $d < \hat{d} < d_b$. But $\hat{d}$ is very hard to determine analytically. Numerically: $\hat{d} = \frac{v^2}{d}\, 0.15014099121093$ $74633626401873698341660201549530029296875\ldots$.

4.3.4.3 Force and final velocity

The dot product of the velocity of the point mass at t_f and the force is is

$$\begin{bmatrix} v - \sqrt{\frac{2\,d}{\underline{u}}\,(g^2 - \underline{u}^2)} \\ \sqrt{2\,d\,\underline{u}} \end{bmatrix}^{\mathrm{T}} \begin{bmatrix} -\sqrt{g^2 - \underline{u}^2} \\ \underline{u} \end{bmatrix} = g^2 \sqrt{\frac{2\,d}{\underline{u}}} - \sqrt{g^2 - \underline{u}^2}\,v$$

Setting this expression equal to zero yields the very Equation (4.1), which we set equal to zero to determine $\underline{u}$ in the first place. Therefore the force is rectangular to the final velocity. This was claimed in [1] and is now proven.

4.4 Back to the Simplified Control Problem

We can use $\underline{u}_1$ to calculate c:

$$c = -\frac{\sqrt{-b^2 - 3^{\frac{1}{3}}\,3\,b^{\frac{4}{3}}\,g^2\,v^4 - 3^{\frac{2}{3}}\,3\,b^{\frac{2}{3}}\,g^4\,v^8 - 3\,g^6\,v^{12}}}{\sqrt{b^2 + 3\,g^6\,v^{12}}}$$

The trajectory of this problem is

$$\bar{x}(t) = \begin{bmatrix} v\,t - \frac{1}{2}\,\bar{u}_1\,t^2 \\ \frac{1}{2}\,\bar{u}_2\,t^2 \\ v + \bar{u}_1\,t \\ \bar{u}_2\,t \end{bmatrix}, \quad \bar{\lambda}(t) = \begin{bmatrix} 1 \\ c \\ t_\mathrm{f} - t \\ (t_\mathrm{f} - t)\,c \end{bmatrix}.$$

The evolution of the Hamiltonian then becomes

$$\begin{aligned} \bar{H}(\bar{x}(t), \bar{\lambda}(t), \bar{u}(t)) &= \bar{\lambda}_1(t)\,\bar{x}_3(t) + \bar{\lambda}_2(t)\,\bar{x}_4(t) + \bar{\lambda}_3(t)\,\bar{u}_1 + \bar{\lambda}_4(t)\,\bar{u}_2 \\ \bar{H}\big(\bar{u}(t), t\big) &= v + \bar{u}_1\,t + c\,\bar{u}_2\,t + (t_\mathrm{f} - t)\,\big(\bar{u}_1 + c\,\bar{u}_2\big) \\ \bar{H}\big(\bar{u}(t), t\big) &= v + (\bar{u}_1 + c\,\bar{u}_2)\,t + (t_\mathrm{f} - t)\,\big(\bar{u}_1 + c\,\bar{u}_2\big) \\ \bar{H}\big(\bar{u}(t)\big) &= v + t_\mathrm{f}\,\big(\bar{u}_1 + c\,\bar{u}_2\big) \\ \bar{H}\big(\bar{u}(t)\big) &= v + \sqrt{\frac{2\,d}{\bar{u}_2}}\,\big(\bar{u}_1 + c\,\bar{u}_2\big) \end{aligned}$$

When replacing $\bar{u}_i$ by

$$\begin{aligned} \bar{u}_1 &= -\frac{g}{\sqrt{1 + c^2}} \\ \bar{u}_2 &= -\frac{c\,g}{\sqrt{1 + c^2}} \end{aligned}$$

and setting $\bar{H}$ to zero, we get another equation in c and v, d, g, which can be solved for c. We gain the same equation by doing the same as above: setting the dot product of the force and final velocity equal to zero.

4.5 Back to the Original Control Problem

We can use the mapping of $\bar{u}$ to the original u to make further conclusions on the original problem.

4.5.1 Without weight shift ($h = 0$)

No momentum will be exerted on the vehicle, therefore $x_3(t) = x_6(t) = 0$. We also know that

$$\begin{bmatrix}\lambda_1(t)\\ \lambda_2(t)\\ \lambda_4(t)\\ \lambda_5(t)\end{bmatrix} = \begin{bmatrix}\bar{\lambda}_1(t)\\ \bar{\lambda}_2(t)\\ \bar{\lambda}_3(t)\\ \bar{\lambda}_4(t)\end{bmatrix} = \begin{bmatrix}1\\ k\\ t_\mathrm{f} - t\\ (t_\mathrm{f} - t)\,k\end{bmatrix}.$$

The relationship between u and $\bar{u}$ for $h = 0$, $\varphi(t) \equiv 0$ is

$$\begin{aligned}(u_1 + u_3) &= m\,\bar{u}_1,\\ (u_2 + u_4) &= m\,\bar{u}_2,\end{aligned}$$

therefore $x_4(t) = v + \bar{u}_1\,t$ and $x_5(t) = \bar{u}_2\,t$.

4.5.1.1 Costate

This simplifies the costate dynamics to

$$\begin{aligned}\dot{\lambda}(t) &= \begin{bmatrix}0\\ 0\\ x_5\,\lambda_1 - x_4\,\lambda_2\\ -\lambda_1\\ -\lambda_2\\ -\lambda_3 - x_5\,\lambda_4 + x_4\,\lambda_5\end{bmatrix}\\ &= \begin{bmatrix}0\\ 0\\ \bar{u}_2\,t - (v + \bar{u}_1\,t)\,k\\ -1\\ -k\\ -\lambda_3 - \bar{u}_2\,t\,(t_\mathrm{f} - t) + (v + \bar{u}_1\,t)\,(t_\mathrm{f} - t)\,k\end{bmatrix}.\end{aligned}$$

Therefore

$$\dot{\lambda}_3(t) = -k\,(v + \bar{u}_1\,t) + \bar{u}_2\,t = -k\,v + (\bar{u}_2 - k\,\bar{u}_1)\,t = -k\,v$$

since $k = \frac{\bar{u}_2}{\bar{u}_1}$ and thus

$$\lambda_3(t) = k\,v\,(t_f - t).$$

Furthermore

$$\begin{aligned}\dot{\lambda}_6(t) &= -k\,v\,(t_f - t) - \bar{u}_2\,t\,(t_\mathrm{f} - t) + (v + \bar{u}_1\,t)\,(t_\mathrm{f} - t)\,k \\ &= (t_f - t)\big(-k\,v + k\,v + (-\bar{u}_2 + k\,\bar{u}_1)\,t\big) \\ &= 0\end{aligned}$$

and thus $\lambda_6(t) = 0$.

4.5.1.2 Hamiltonian

The Hamiltonian

$$H\big(x(t), \lambda(t), u(t)\big) = (x_4\,\cos x_3 - x_5\,\sin x_3)\,\lambda_1 + (x_4\,\sin x_3 + x_5\,\cos x_3)\,\lambda_2 + x_6\,\lambda_3 + \left(\frac{u_1 + u_3}{m} + x_5\,x_6\right)\lambda_4 + \left(\frac{u_2 + u_4}{m} - x_4\,x_6\right)\lambda_5 + \frac{l_\mathrm{F}\,u_2 - l_\mathrm{R}\,u_4}{\Theta}\,\lambda_6.$$

again becomes

$$H = v + t_\mathrm{f}\,(\bar{u}_1 + k\,\bar{u}_2).$$

4.5.2 With weight shift ($h \neq 0$)

The situation is slightly more complicated, because a momentum will be exerted on the vehicle which causes $x_3(t)$ and $x_6(t)$ to be unequal to 0. As is shown in [3], the results of the analytical mapping and the numerical solution of the optimal control problem with weight shift are identical. The vehicle with four wheel steering, as modeled here, can generate any force within the limits of friction independent of it's orientation, even if the weight shift effect is considered.

Chapter 5

Influence of Tire Characteristics

The influence of the tire characteristics on the maneuverability has been investigated. For a total of nine different tire characteristics, the obstacle avoidance maneuver was used as the benchmark. The characteristics were changed in the following way: The peak traction coefficient μ has been increased to 1.1 and decreased to 0.9, the default value is 1. The cornering stiffness C has been compared for it's original value and triple and half of that.

The results show that the cost criterion decreases with increasing μ, as one would expect. It also decreases with increasing cornering stiffness.

Table 5.1: Absolute distance to complete maneuver, in meters (smaller is better).

	$c = *3$	$c = 1$	$c = /2$
$\mu = 1.1$	26.62	26.37	26.62
$\mu = 1$	27.39	27.73	28.02
$\mu = 0.9$	28.95	29.32	29.62

Table 5.2: Relative to the nominal case (a decrease is better).

	$c = *3$	$c = 1$	$c = /2$
$\mu = 1.1$	-4.01%	-4.9%	-4.0%
$\mu = 1$	-1.25%	base	1.04%
$\mu = 0.9$	4.4%	5.7%	6.81%

For more details, please refer to the MATLAB-Software.

Chapter 6

Influence of Active Tires

The idea investigated here is to change the cornering stiffness of the unsteered rear tire throughout the maneuver. This is accomplished mathematically by adding an input which is multiplied with the cornering stiffness. This input is limited to a certain range around 1. The equations of motion and the equations governing the optimal control problem are found in the same fashion as for the other problems in [1]. During the numerical computation, the value of this new input is almost always at the limits of it's range, the algorithm that minimizes the Hamiltonian with respect to this input exploits this fact.

Unfortunately, the active tire does not prove effective. Of course, the steered rear wheel defines the upper bound for the effectiveness of an active tire on the rear wheel. However, the active tire is not even close to that bound, which is already much lower than expected when the investigations leading to [1] started. A flaw of the simulation carried out here is that a tire with a fixed in- or decreased cornering stiffness should be a lower bound for the active tire, but the active tire does not reach this lower bound. The reason is likely that the optimal problem is not well defined.

For more details, please refer to the MATLAB-Software.

Table 6.1: Summarizing the performance of different vehicle configurations for the obstacle avoidance maneuver.

	setup		st.	t_f	x_1	% to 1	% to 11
1	d	default		0.99	27.74	0.00%	
2	s	dec. mu, inc. c		1.02	28.95	4.38%	
3	t	inc. mu, dec. c		0.96	26.62	-4.01%	
4	x	dec. mu		1.04	29.32	5.73%	
5	y	inc. mu		0.94	26.37	-4.94%	
6	g	inc. c		0.97	27.39	-1.25%	
7	j	dec. c		1.00	28.02	1.04%	
8	i	dec. mu, dec. c		1.05	29.62	6.81%	
9	f	inc. mu, inc. c		0.93	26.05	-6.08%	
10	v	c: 0.9-1.1		0.98	27.70	-0.14%	
11	w	c: 0.7-1.3		0.98	27.64	-0.36%	
12	z	c: 0.5-3.0		0.98	27.51	-0.82%	
13	d	default	✓	0.93	26.49	-4.51%	0.00%
14	e	w.s.e.	✓	0.93	26.49		0.00%
15	s	dec. mu	✓	0.97	27.98		5.66%
16	t	inc. mu	✓	0.88	25.20		-4.87%

Bibliography

[1] Patrick Dingle. Optimal emergency maneuvers for passengers vehicles on highways. Master's thesis, Eidgenössische Technische Hochschule Zürich, 2009.

[2] H. P. Geering. *Optimal Control with Engineering Applications*. Springer, 2007.

[3] Mu Wang. Optimal emergency maneuvers for passengers vehicles with advanced single track models, Semester Project, Eidgenössische Technische Hochschule Zürich, 2010.

Optimal Emergency Maneuvers on Highways for Passenger Vehicles with Two- and Four-Wheel Active Steering

Patrick Dingle*
Kiva Systems, Inc.
225 Wildwood Ave.
Woburn, MA 01801 USA
prd8@cornell.edu

Lino Guzzella
Dynamic Systems and Control Laboratory
ETH Zürich
Zürich, Switzerland
lguzzella@ethz.ch

***Abstract*— This paper presents and utilizes an optimal-control based method for quantifying the maneuverability of actively-controlled passenger vehicles during emergency highway-speed situations. The research is motivated by the desire to better understand the performance benefits of additional actuated degrees of freedom when compared to a typical vehicle. Specifically, the performance benefits of front-steer vehicles are compared to front- and rear-steer vehicles. In both cases, the vehicle is assumed to be capable of applying independent accelerating/braking torques to the front and rear wheels. The emergency maneuvers considered are obstacle avoidance, barrier avoidance, lane changes, and recovery from an arbitrary state. Necessary conditions for optimality and optimal control laws are found for each case. Solutions are found using a lumped-parameter planar single-track vehicle model and nonlinear tire dynamics are assumed. Front- and rear-steering vehicles are shown to have better maneuverability during all emergency maneuvers. Based on the optimal vehicle trajectories, the benefits are quantified using appropriate performance indices.**

I. INTRODUCTION

A critical safety metric in the design of automobiles is maneuverability. In particular, this ability for vehicles to quickly change speed and direction is important for lightweight vehicles since they are most susceptible to damage should a collision occur. The primary motivation for this research is to investigate and quantify the potential performance benefits of augmenting a typical front-steer vehicle with rear-steering as well as independent accelerating/braking torques for each.

Interest in optimal emergency maneuvers has intensified over the past two decades. Research can generally be categorized into open-loop methods aimed at finding optimal or near-optimal vehicle trajectories for various objectives, and closed-loop methods for following a desired trajectory. Early methods for finding open-loop lane change maneuvers for front-wheel steering vehicles were proposed by Chee et al. [1] and Hatipoglu et al. [2]. The lane change maneuver was later formulated as an optimization problem by Shiller et al. [3] and approximately solved as a parameter optimization problem for front-wheel actively-steered vehicles. In [4], the general problem of finding optimal trajectories for changing heading given acceleration constraints is discussed. A lane-change trajectory assuming simplified vehicle dynamics is discussed along with closed-loop implementations in [5]. Closed-loop methods for executing lane change maneuvers has also been the subject of intense study [6], [7]. With recent technological advancements in automation and actuation, four-wheel active steering and braking has become a feasible technology within the automotive industry. Some of the advantages of active steering were outlined by Ackermann et al. [8]. Closed-loop utilizations of active steering in four-wheel vehicles are studied by Higuchi et al. [9] and Cho et al. [10]. It appears that the study of optimal avoidance maneuvers for vehicles with multiple actuated degrees of freedom has scarcely been studied to date.

* Corresponding author. Research was carried out at the Swiss Federal Institute of Technology (ETH Zürich)

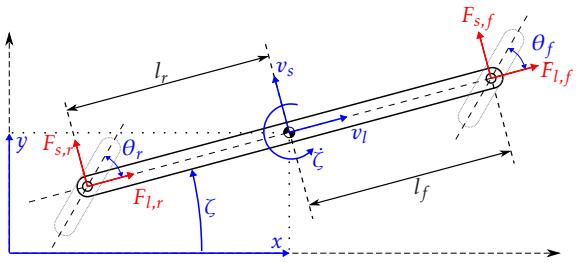

Fig. 1: Single-track planar vehicle model: top view

The purpose of this paper is to present an optimal control based method that can be used to quantify the performance of a vehicle during various highway-speed maneuvers, and to utilize the method to quantify the advantages of vehicles with various actuated degrees of freedom. A planar single-track bicycle model is assumed; pitch and roll dynamics are therefore neglected. Nonlinear tire dynamics are assumed and serve as the critical constraint bounding vehicle performance. Pontryagin's Minimum Principle is utilized to find the optimal control laws, and the optimal open-loop control inputs and trajectories are presented. The tradeoffs and benefits of the different vehicles are discussed by direct comparison of the results. Since the trajectories are optimal and generally maximize the tire tractive force at all wheels, the maneuvers are not robust and therefore impractical to implement directly. Extensions to closed loop control are certainly possible, but outside the scope of this paper.

II. SYSTEM MODELING

The selection of a system model requires making tradeoffs between conflicting goals. Given the goal of finding optimal control trajectories in continuous time, a simple model is desired. On the other hand, relevant vehicle dynamics must be captured by the model for the results to be useful. The model presented in this section is chosen as a compromise. The chosen system model contains three components: the chassis, front wheel model, and rear wheel model. The model, as mentioned in the introduction, is planar. The dynamics of the left and right wheels are lumped together into single front- and rear-wheel tire models.

Variable	Value	Variable	Value
g	9.806 m/s^2	m_v	910 kg
I_v	1414 kg m^2	l_f	1.005 m
l_r	1.465 m	μ	1
a_2	17.8	a_3	1.5
a_5	0.432		

TABLE I: Vehicle parameters used for numerical optimization

A. Chassis Model

The chassis is modeled as a planar rigid-body with input forces at the locations of the lumped front and rear wheels, as shown in Figure 1. Such a model without pitch and roll dynamics provides simplicity for the purpose of solving optimal control problems, but at the cost of omitting certain dynamic behaviors of the vehicle. In particular, the neglected pitch and roll dynamics are increasingly important for vehicles with a high center of mass. The equations governing the dynamics of the chassis are given by Equations (1) through (5).

$$F_{l,f} + F_{l,r} = m_v\left(\dot{v}_l - v_s\dot{\zeta}\right) \tag{1}$$

$$F_{s,f} + F_{s,r} = m_v\left(\dot{v}_s + v_l\dot{\zeta}\right) \tag{2}$$

$$F_{z,f} + F_{z,r} = m_v g \tag{3}$$

$$F_{z,f}\,l_f - F_{z,r}\,l_r = 0 \tag{4}$$

$$F_{s,f}\,l_f - F_{s,r}\,l_r = I_z\ddot{\zeta} \tag{5}$$

In these equations, F refers to the forces acting upon the tire; the index f refers to the front wheel, r to the rear wheel, l to the longitudinal direction, s to the lateral direction, and z to the vertical (normal force) direction.

B. Vehicle Parameters

To obtain solutions, numerical values are necessary for all vehicle and environmental parameters; optimization and simulation parameters are given in Table I. The chassis parameters were estimated to represent as closely as possible a Volkswagen Golf MK2, and the wheel parameters were obtained from [11]. This vehicle was chosen since it exemplifies the mass and tractive properties of a typical lightweight vehicle, by which this research was motivated.

C. Road/Tire Interaction Model

The purpose of the road/tire interaction model is to map a wheel's steering angle θ and rotational velocity ω_a to longitudinal and lateral forces F_l and F_s acting on the chassis. A simplified variant of the "magic tyre formula" proposed by Pacejka [11] is assumed and governed by Equations (6) through (9). For simplicity, all equations are given the subscript f and refer to the equations that govern the front wheel; with appropriate changes, they are also valid for the rear wheel. This model assumes the magnitude of the tire force F_f to be a nonlinear function of the tire slip magnitude and independent of the slip direction. Isotropic tire properties are thus implicitly assumed.

$$f_{\text{tr}}(\sigma_f) \triangleq \sin\left(a_3 \arctan\left(a_2\left((1-a_5)\,\sigma_f + \left(\frac{a_5}{a_2}\right)\arctan\left(a_2\sigma_f\right)\right)\right)\right) \tag{6}$$

$$F_f = \mu F_{z,f}\, f_{\text{tr}}(\sigma_f) \tag{7}$$

$$F_{l,f} = -\frac{\sigma_{l,f}}{\sigma_f}F_f \tag{8}$$

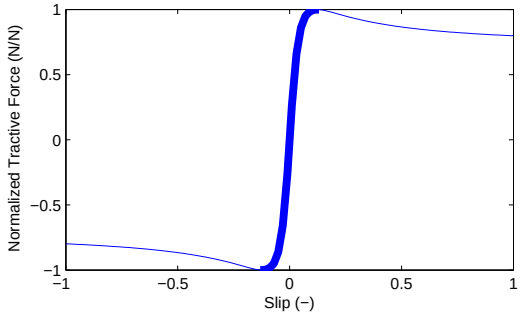

Fig. 2: 2D representation of the slip-based tire tractive force. When the domain (slip σ) is restricted to the bold region, the function is bijective.

$$F_{s,f} = -\frac{\sigma_{s,f}}{\sigma_f}F_f \tag{9}$$

The parameters a_2, a_3, and a_5 are tire-dependent constants, and μ is a "grip coefficient" that is equal to unity under nominal conditions and may change, for example, with the moisture content of the road. The longitudinal and lateral tire slip quantities σ_l and σ_s are the ratios of the contact patch speed to the tire speed, as defined in [11].

The force direction, β, is applied in the opposite direction of the velocity of the tire's contact patch. It is given for the front wheel by

$$\beta_f = \theta_f - \arctan\left(\frac{v_{s,f}}{v_{l,f} - \omega_{a,f}\,r_f}\right), \tag{10}$$

where ω_a represents rotational wheel speed about the axle and r represents the wheel's radius.

Since the wheel speed ω_a is assumed to be completely controllable, the force direction given by Equation (10) is also controllable. This is evident by the observation that the *arctan* function is surjective over a full range of steering angles $\left(\frac{-\pi}{2}, \frac{\pi}{2}\right)$. Further, the tire force F_f, as given by Equations (6) and (7), can be shown to be bijective and therefore invertible over a restricted domain and range (ref. Figure 2):

$$F_f : \left[-\arg\min_{\sigma_f} f_{\text{tr}}(\sigma_f), \arg\max_{\sigma_f} f_{\text{tr}}(\sigma_f)\right] \mapsto \left[-\mu F_{z,f}, \mu F_{z,f}\right] \tag{11}$$

Therefore, within this domain it follows that a one-to-one relationship exists between the wheel force components $\{F_{l,f}, F_{s,f}\}$ and the physical inputs: the wheel speed $\omega_{a,f}$ and steering angle θ_f. The domain is enforced with a constraint

$$\sqrt{F_{l,f}^2 + F_{s,f}^2} \leq \mu F_{z,f} \tag{12}$$

which limits the magnitude of the forces. Given this constraint and the bijective relationship between the force components and wheel angle and speed, it is thus possible to neglect the road/tire interaction model completely when the steering angle and wheel speeds are unconstrained. In such a case the force components can be directly used as inputs. When the wheel speed is controllable but not the steering angle, forces cannot be used directly as inputs.

D. Input-Output Models

The chassis and road/tire interaction models can be combined to form input-output models for the vehicles of interest. For all vehicles, the state vector $\mathbf{x}$ is first defined. The

states consist of the position, orientation, velocity, and rotational velocity of the vehicle. For simplicity of the equations of motion, velocity components v_l and v_s are expressed in the vehicle's reference frame.

$$\mathbf{x} \triangleq \begin{bmatrix} x_1 \\ x_2 \\ x_3 \\ x_4 \\ x_5 \\ x_6 \end{bmatrix} \triangleq \begin{bmatrix} x \\ y \\ \zeta \\ v_l \\ v_s \\ \dot{\zeta} \end{bmatrix} \tag{13}$$

For the dual-steer dual-brake vehicle, the control vector $\mathbf{u}$ is defined as the force components on the front and rear wheels:

$$\mathbf{u} \triangleq \begin{bmatrix} u_1 \\ u_2 \\ u_3 \\ u_4 \end{bmatrix} \triangleq \begin{bmatrix} F_{l,f} \\ F_{s,f} \\ F_{l,r} \\ F_{s,r} \end{bmatrix} \tag{14}$$

For the front-steer front-brake vehicle, the control vector simply omits u_3 and u_4. For the front-steer dual-brake vehicle, the control vector is:

$$\mathbf{u} \triangleq \begin{bmatrix} u_1 \\ u_2 \\ u_4 \end{bmatrix} \triangleq \begin{bmatrix} F_{l,f} \\ F_{s,f} \\ \omega_{a,r} \end{bmatrix} \tag{15}$$

where the wheel speed $\omega_{a,r}$ feeds into the road/tire interaction model – along with the vehicle states – to yield the force components $F_{l,r}$ and $F_{s,r}$.

Given the state vector and control input vectors, the input-output equations of motion can now be stated for each vehicle. The differential equations governing the dual-steer dual-brake vehicle are:

$$\dot{\mathbf{x}} = \begin{bmatrix} \dot{x}_1 \\ \dot{x}_2 \\ \dot{x}_3 \\ \dot{x}_4 \\ \dot{x}_5 \\ \dot{x}_6 \end{bmatrix} = \begin{bmatrix} x_4 \cos x_3 - x_5 \sin x_3 \\ x_4 \sin x_3 + x_5 \cos x_3 \\ x_6 \\ \frac{u_1+u_3}{m_v} + x_5 x_6 \\ \frac{u_2+u_4}{m_v} - x_4 x_6 \\ \frac{l_f u_2 - l_r u_4}{I_v} \end{bmatrix} \tag{16}$$

The differential equations governing the vehicles with fewer control inputs are derived in a similar manner, but are more complex since the rear tire forces are found using the nonlinear road/tire interaction model, rather than being used directly as inputs.

III. OPTIMAL CONTROL FORMULATION

The purpose of this section is to formalize optimal control problems corresponding to avoidance maneuvers in such a way that the performance of each maneuver is measurable. Four general scenarios are considered: A pure obstacle avoidance maneuver, a barrier avoidance maneuver, a recovery maneuver, and a double lane change maneuver.

A. "Pure Obstacle Avoidance" Maneuver

The goal of the "pure obstacle avoidance" optimal control problem is to quantify a vehicle's ability to avoid an obstacle of known width, as depicted in Figure 3(a). The vehicle is assumed to be moving straight forward along the highway at a steady state. Beginning at some initial time, the vehicle must attempt to minimize the distance traveled along the highway until the vehicle translates laterally by a fixed distance y_f, which corresponds to the lateral displacement needed to avoid the obstacle. This longitudinal distance traveled is a direct quantification of the performance of a vehicle executing the maneuver. The problem is formalized as

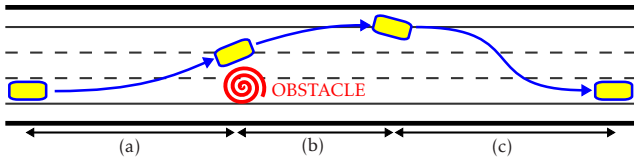

Fig. 3: A phased highway maneuver consisting of: (a) "pure obstacle avoidance" maneuver, (b) "barrier avoidance" maneuver, and (c) "recovery" maneuver

$$\min_{\mathbf{u}(t)\in\mathcal{S}} x_1(t_f) \tag{17}$$

subject to

$$\dot{\mathbf{x}}(t) = f(\mathbf{x}(t), \mathbf{u}(t)) \tag{18}$$

$$\mathbf{x}(0) = \begin{bmatrix} 0 & 0 & 0 & v_{l,i} & 0 & 0 \end{bmatrix}^{\mathrm{T}} \tag{19}$$

$$\mathbf{x}(t_f) \in \mathbb{R}^6 : x_2(t_f) = y_f \tag{20}$$

where $\mathcal{S}$ represents the set of allowable control inputs, $f(\cdot)$ represents the equations of motion of the given vehicle, and $v_{l,i}$ represents the initial longitudinal velocity.

B. "Barrier Avoidance" Maneuver

The purpose of the "barrier avoidance" maneuver is to reduce to zero the velocity of the vehicle in the direction of the barrier, as depicted in Figure 3(b). An arbitrary initial state is assumed which could, for example, be the final state achieved by the "pure obstacle avoidance" maneuver. The performance of such a maneuver can be quantified as the total distance traveled in the direction of the barrier. The objective is only to minimize this distance; additional end constraints such as yaw angle and rate are therefore not specified. Since no control effort is used to achieve a nominal final vehicle state, the vehicle can terminate this maneuver in an extremely dynamic state which might include large tire slip magnitudes and angles. The problem is formalized as

$$\min_{\mathbf{u}(t)\in\mathcal{S}} x_2(t_f) \tag{21}$$

subject to (18) and

$$\mathbf{x}(0) = \begin{bmatrix} x_i & y_i & \zeta_i & v_{l,i} & v_{s,i} & \dot{\zeta}_i \end{bmatrix}^{\mathrm{T}} \tag{22}$$

$$\mathbf{x}(t_f) \in \mathbb{R}^6 : x_5(t_f) = -x_4(t_f) \tan\big(x_3(t_f)\big). \tag{23}$$

C. "Recovery" Maneuver

The purpose of the "recovery" maneuver is to bring the vehicle from an arbitrary initial state to a nominal final state, as depicted in Figure 3(c). The initial state could, for example, be the final state achieved by the "pure obstacle avoidance" or "barrier avoidance" maneuvers. Conflicting objectives prevent a simple quantification for vehicle performance during this maneuver. While one objective is to return to a nominal state in a short amount of time, another objective is to prevent a trajectory that leaves the width of the highway. The second objective could be obtained with state constraints. However, such a method significantly increases the complexity of the

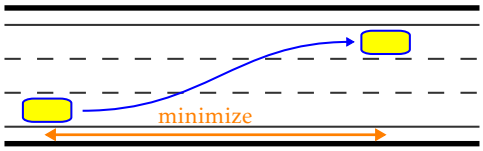

Fig. 4: "Double Lane Change" maneuver: minimize distance to complete a lane change

problem and makes it difficult to obtain an optimal solution. A simpler method is to choose an objective function that heavily penalizes trajectories that move towards the highway barrier while simultaneously minimizing the time to execute the maneuver. An integral-square-error norm over the lateral position works well for these purposes. The problem is formalized as

$$\min_{\mathbf{u}(t)\in\mathcal{S}} \int_0^{t_f} \left(x_2(t) - y_f\right)^2 dt \tag{24}$$

subject to (18) and

$$\mathbf{x}(0) = \begin{bmatrix} x_i & y_i & \zeta_i & v_{l,i} & v_{s,i} & \dot{\zeta}_i \end{bmatrix}^{\mathrm{T}} \tag{25}$$

$$\mathbf{x}(t_f) \in \begin{bmatrix} \mathbb{R} & y_f & 0 & \mathbb{R} & 0 & 0 \end{bmatrix}^{\mathrm{T}} \tag{26}$$

where y_f represents the desired final lateral position on the highway.

D. "Double Lane Change" Maneuver

The purpose of the "double lane change" maneuver is to execute a double lane change such that the vehicle begins and ends in a nominal state, as depicted in Figure 4. The performance of such a maneuver is again quantified by the longitudinal distance to complete the maneuver. The problem is formalized as

$$\min_{\mathbf{u}(t)\in\mathcal{S}} x_1(t_f) \tag{27}$$

subject to (18) and

$$\mathbf{x}(0) = \begin{bmatrix} 0 & 0 & 0 & v_{l,i} & 0 & 0 \end{bmatrix}^{\mathrm{T}} \tag{28}$$

$$\mathbf{x}(t_f) \in \begin{bmatrix} \mathbb{R} & y_f & 0 & \mathbb{R} & 0 & 0 \end{bmatrix}^{\mathrm{T}} \tag{29}$$

IV. METHODS

The purpose of this section is to present an overview of the methods utilized to solve the optimal control problems formulated in Section III.

The main theoretical tool used to find optimal solutions is Pontryagin's Minimum Principle [12], [13]. The Principle provides a set of necessary conditions for optimality. Differential equations are derived that govern the evolution of a costate vector $\boldsymbol{\lambda}(t)$ as a function of the states $\mathbf{x}(t)$, costates $\boldsymbol{\lambda}(t)$, and control inputs $\mathbf{u}(t)$. Further, the principle provides a means of determining the optimal control input $\hat{\mathbf{u}}(t)$ at any time given the state $\mathbf{x}(t)$ and known costates $\boldsymbol{\lambda}(t)$. Given this "optimal control law," the state and costate differential equations are reduced to functions of $\mathbf{x}(t)$ and $\boldsymbol{\lambda}(t)$. Solutions satisfying the necessary conditions for optimality can thus found by a numerical solution of a two-point boundary value problem. The following sections detail the necessary conditions for optimality and methods to solve the optimal control law.

A. Necessary Conditions for Optimality

For any given vehicle at any given time, the Hamiltonian is first defined as a weighted sum of the objective at time t and constraints. The portion of the objective function applied at any time t is defined as the function $L(\mathbf{x}(t), \mathbf{u}(t))$ and is zero for all maneuvers of interest except the "recovery" maneuver. Since no state constraints exist in any maneuvers, the constraints are simply the equations of motion of the vehicle of interest.

$$H(\mathbf{x}(t), \mathbf{u}(t), \boldsymbol{\lambda}(t)) \triangleq L(\mathbf{x}(t), \mathbf{u}(t)) + \boldsymbol{\lambda}^{\mathrm{T}}(t) f(\mathbf{x}(t), \mathbf{u}(t)) \tag{30}$$

Given any optimal control problem defined in Section III, along with any vehicle model defined in Section II, and the corresponding Hamiltonian function, Pontryagin's Minimum Principle provides necessary conditions for optimality. The conditions can be grouped into three sets of requirements.

First, the Hamiltonian must be globally minimized at all times over the vehicle's set of allowable control inputs. The optimal control inputs $\hat{\mathbf{u}}(t)$ and state vectors $\hat{\mathbf{x}}(t)$ and $\hat{\boldsymbol{\lambda}}(t)$ are introduced.

$$H\left(\hat{\mathbf{x}}(t), \hat{\mathbf{u}}(t), \hat{\boldsymbol{\lambda}}(t)\right) \leq H\left(\hat{\mathbf{x}}(t), \mathbf{u}, \hat{\boldsymbol{\lambda}}(t)\right) \forall t \in \left[0, t_f\right] \forall \mathbf{u} \in \mathcal{S} \tag{31}$$

Second, the differential equations must constrain the evolution of the states $\mathbf{x}(t)$ and costates $\boldsymbol{\lambda}(t)$. The set of equations governing the differential equations has already been discussed and is detailed in Section II.

$$\frac{d}{dt}\hat{\boldsymbol{\lambda}}(t) = -\frac{\partial H}{\partial x}\left(\hat{\mathbf{x}}(t), \hat{\mathbf{u}}(t), \hat{\boldsymbol{\lambda}}(t)\right) \tag{32}$$

The third set of requirements provides boundary conditions for the differential equations. In addition to the initial and final state constraints defined in Section III, the optimal costates at the final time must satisfy

$$\hat{\boldsymbol{\lambda}}(t_f) = \frac{\partial K}{\partial t}\left(\hat{\mathbf{x}}(t_f)\right) + \hat{q} \quad \text{s.t.} \quad \hat{q} \in T^{\star}\left(\mathcal{X}_f, \hat{\mathbf{x}}(t_f)\right) \tag{33}$$

where $K\left(\hat{\mathbf{x}}(t_f)\right)$ is the portion of the objective function that is a function of the final states, $\mathcal{X}_f$ is the set of target end states, and $T^{\star}\left(\mathcal{X}_f, \hat{\mathbf{x}}(t_f)\right)$ is the tangent cone of the normal cone of the set $\mathcal{X}_f$ at $\hat{\mathbf{x}}(t_f)$. Ultimately, this requirement adds a costate constraint for every unconstrained end state at $t = t_f$.

B. Solution of the Optimal Control Law

Equation (31) states that the optimal control law is obtained by finding a permissible control input that globally minimizes the Hamiltonian. Since the Hamiltonian depends both on the vehicle model and the optimal control formulation, there are to many combinations to discuss each independently. However, any given vehicle and scenario can be solved by one of the two methods discussed below.

In the case of the dual-steer dual-brake vehicle, the input-output equations of motion bypass the tire dynamics. The Hamiltonian for this vehicle under all maneuvers except the "recovery" maneuver is:

$$\begin{aligned} H(\mathbf{x}, \mathbf{u}, \boldsymbol{\lambda}) = \\ &(x_4 \cos x_3 - x_5 \sin x_3)\lambda_1 + (x_4 \sin x_3 + x_5 \cos x_3)\lambda_2 + \\ &x_6 \lambda_3 + \frac{1}{m_v}(u_1 + u_3 + m_v x_5 x_6)\lambda_4 + \\ &\frac{1}{m_v}(u_2 + u_4 - m_v x_4 x_6)\lambda_5 + \frac{1}{I_v}\left(l_f u_2 - l_r u_4\right)\lambda_6 \end{aligned} \tag{34}$$

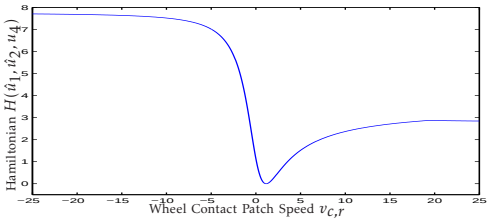

Fig. 5: Typical plot of the Hamiltonian H vs. the wheel longitudinal contact patch speed $v_{c,r}$

The Hamiltonian is clearly affine with respect to $\mathbf{u}$. Given the set of allowable control inputs – see Equation (12) – is also convex, i.e.

$$\mathcal{S} = \left\{ u \in \mathbb{R}^4 \middle| \sqrt{u_1^2 + u_2^2} \leq \mu F_{z,f}, \sqrt{u_3^2 + u_4^2} \leq \mu F_{z,r} \right\}, \quad (35)$$

the optimal control law can be solved analytically using the Karush-Kuhn-Tucker conditions [14]. The resulting optimal control input force vectors are best expressed in polar coordinates:

$$\hat{F}_f = \sqrt{\hat{u}_1^2 + \hat{u}_2^2} = \mu F_{z,f} = \frac{\mu l_r m_v g}{l_f + l_r} \quad (36)$$

$$\hat{\beta}_f = \arctan\left(\frac{\hat{u}_2}{\hat{u}_1}\right) = \arctan\left(\frac{I_v \hat{\lambda}_5 + l_f m_v \hat{\lambda}_6}{I_v \hat{\lambda}_4}\right) \quad (37)$$

$$\hat{F}_r = \sqrt{\hat{u}_3^2 + \hat{u}_4^2} = \mu F_{z,r} = \frac{\mu l_f m_v g}{l_f + l_r} \quad (38)$$

$$\hat{\beta}_r = \arctan\left(\frac{\hat{u}_4}{\hat{u}_3}\right) = \arctan\left(\frac{I_v \hat{\lambda}_5 - l_r m_v \hat{\lambda}_6}{I_v \hat{\lambda}_4}\right) \quad (39)$$

Equations (36) and (38) demonstrate that it is optimal to utilize the maximum possible tire force at all times. The controller is thus a bang-bang controller. The force directions, however, given by Equations (37) and (39), vary as a function of the optimal costate values.

In the cases of the front-steer, dual-brake vehicle, the Hamiltonian is complicated by the inclusion of the road/tire force dynamics in the equations of motion. The Hamiltonian is in fact nonlinear with respect to the rear wheel control input. A "typical" plot of the Hamiltonian as a function of the rear wheel contact patch speed $v_{c,r} \triangleq u_4 r_r$ is given in Figure 5. Due to the nature of the chosen road/tire interaction model, global minimization of the Hamiltonian using the calculus of variations is not possible. At any given time t an iterative approach is instead used. First, the Hamiltonian is searched for a minimum over a discretized input space of the control input. The discretization granularity and limits are chosen heuristically to ensure that a point in the convex neighborhood of a global minimum is found. From this point, a Newton descent method can be used to find a local minimum within a desired tolerance. Given that the Hamiltonian is continuous and that appropriate granularity and search limits of the input space are chosen, this technique will yield a global minima [14].

V. RESULTS

The results of this study were obtained by utilizing the methods outlined in the previous section. The methods were applied using each of the three different vehicles outlined in Section II and the four different maneuvers outlined in Section III. The purpose of this section is to present the most interesting and informative optimal control maneuvers and to quantify the advantages and disadvantages of each vehicle during each maneuver. For each maneuver, the optimal trajectories are first presented along with the quantified performance measurements. Optimal control inputs are then presented and interesting observations are discussed.

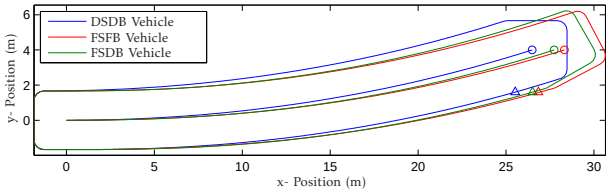

Fig. 6: Swept areas and center of mass path of the three vehicles performing their optimal "pure obstacle avoidance" maneuvers

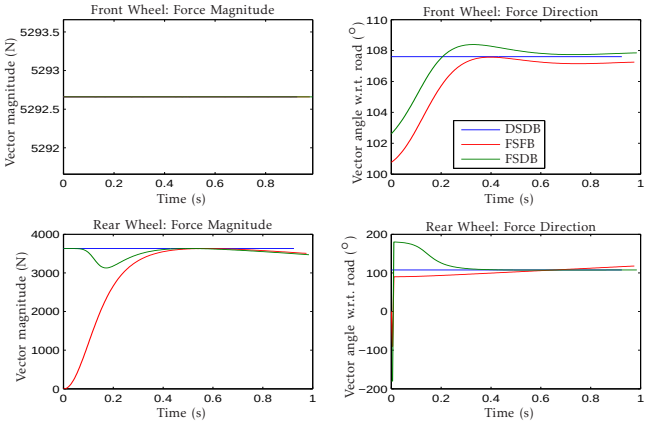

Fig. 7: Optimal wheel force vector components during the "pure obstacle avoidance" maneuver

A. Pure Obstacle Avoidance Maneuver

The optimal trajectories corresponding to each vehicle during the "pure obstacle avoidance" maneuver are given in Figure 6. The performance of each vehicle is quantified by the final longitudinal position. For the front-steer dual-brake (FSDB) vehicle, the maneuver is completed in 27.74 meters. When rear-wheel steering is added to the vehicle (DSDB), the maneuver is completed in 26.49 meters. The results therefore show that for a typical avoidance maneuver, the addition of active rear-wheel steering can reduce the longitudinal distance required to avoid an obstacle by approximately 1.25 meters, or 4.5%.

The optimal control strategies of the vehicles are best interpreted by examining the optimal wheel force vectors in polar coordinates, as in Figure 7. In the case of the DSDB vehicle, the control strategy is straightforward: the force is always maximized, and the force direction is constant and in the direction orthogonal to the final velocity of the vehicle. In the case of the FSDB vehicle, the rear wheel's force vector cannot be fully controlled. The force is again always maximized for the front wheel, but the force direction varies slightly from that of the DSDB vehicle, especially early in the maneuver when the front wheel is able to initiate an ideal

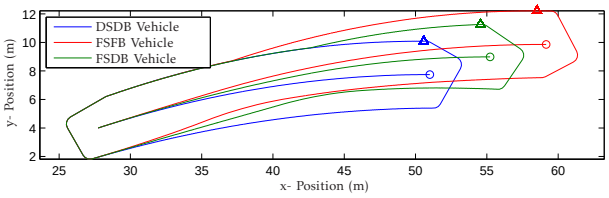

Fig. 8: Swept areas and center of mass path of the three vehicles performing their optimal "barrier avoidance" maneuvers

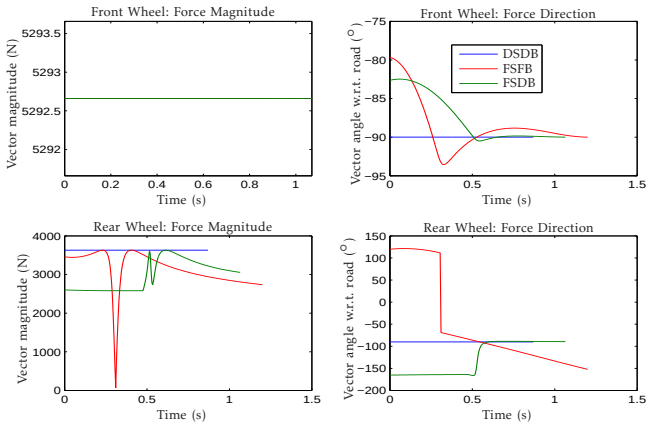

Fig. 9: Optimal wheel force vector components during the "barrier avoidance" maneuver

sideslip magnitude for the rear wheel. Large braking torques are applied by the rear wheel early in the maneuver when the wheel has little sideslip magnitude to generate lateral forces.

B. Barrier Avoidance Maneuver

The optimal trajectories corresponding to each vehicle during the "barrier avoidance" maneuver are shown in Figure 8. During this maneuver, all vehicles begin from a common initial state for comparison purposes. The performance of each vehicle is quantified by the distance traveled in the direction of the barrier. For the front-steer dual-brake (FSDB) vehicle, the distance traveled towards the barrier is 4.99 meters. When rear-wheel braking is added to the vehicle (DSDB), the distance is 3.75 meters. The results therefore show that for this particular "barrier avoidance" maneuver, the addition of active rear-wheel steering can reduce the distance traveled towards the barrier by 1.24 meters, or 24.9%.

The optimal control strategies of the vehicles are again interpreted by examining the optimal wheel force vectors in polar coordinates, shown in Figure 9. Once again, the force magnitude of the front wheel is always maximized for all vehicles since the front wheel is fully controllable. The rear wheel force magnitude is also constant for the DSDB vehicle and generally utilized as much as possible given the slip magnitude for the other vehicles. The force directions are also noteworthy. Not surprisingly, the DSDB vehicle applies its front and rear wheel forces in a direction away from the barrier (−90°). The FSDB vehicle utilizes its rear-wheel braking capability in an interesting way during the early part of the maneuver. During this time, the vehicle's rear wheel has a large lateral slip magnitude in the direction away from the barrier. Without braking capability, this slip

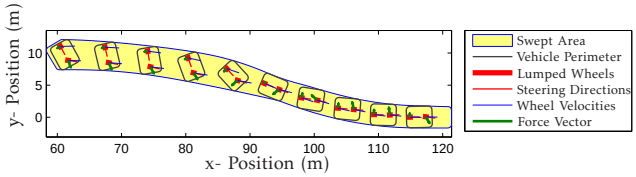

Fig. 10: Birds-eye snapshot view of the FSFB vehicle executing the "recovery" maneuver

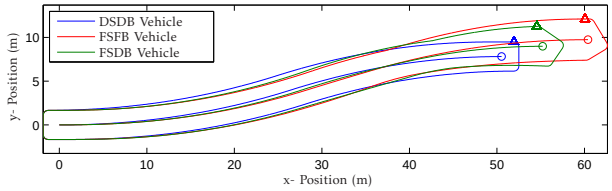

Fig. 11: Swept areas and center of mass path of the three vehicles performing their optimal "pure obstacle avoidance" maneuver and "barrier avoidance" maneuver in sequence

magnitude would result in a force towards the barrier. The vehicle therefore locks its rear wheels (or in fact spins them in reverse at the largest feasible velocity) resulting in the force direction being applied longitudinally with little or no lateral force. This behavior is seen whenever the FSDB vehicle encounters a situation with an undesired lateral slip direction.

C. Recovery Maneuver

The "recovery" maneuver demonstrates the ability for a vehicle to return to a nominal driving condition when starting at an arbitrary state. As discussed in Section II, there is no single measurable quantity that serves as a good performance metric. Instead, an objective was chosen such that the vehicle returns to a nominal state in a reasonable amount of time while heavily penalizing any motion towards the highway barriers. Figure 10 presents an optimal trajectory of the FSFB recovering from an extreme initial state, which is in fact the final state from the "pure obstacle avoidance" and "barrier avoidance" maneuvers being executed in sequence. The maneuver is completed in a reasonable distance with no overshoot towards either barrier. Since this vehicle contains the fewest number of controllable degrees of freedom, this example suffices to show that an acceptable recovery maneuver is possible for all the vehicles considered.

D. Phased-Approach Maneuver

The "phased approach" maneuver consists of the previous three maneuvers being executed in sequence. The optimal trajectory from such an approach represents a vehicle's ability to avoid an obstacle of a known width as sharply as possible, then to eliminate any velocity towards the barrier, and finally to return to a nominal state. Since quantification of the "recovery" phase of this maneuver is not of interest, only the first two phases are measured. Figure 11 depicts the optimal trajectories of the vehicles performing the first two phases of this approach. The resulting quantifications and optimal control inputs are similar to the "barrier avoidance" results, and therefore not presented.

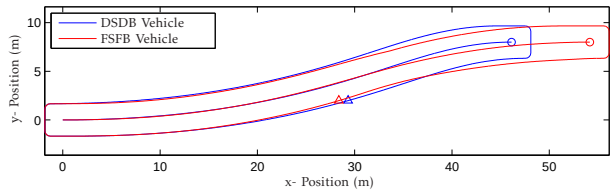

Fig. 12: Swept areas and center of mass path of the DSDB and FSFB vehicles performing the "double lane change" maneuver

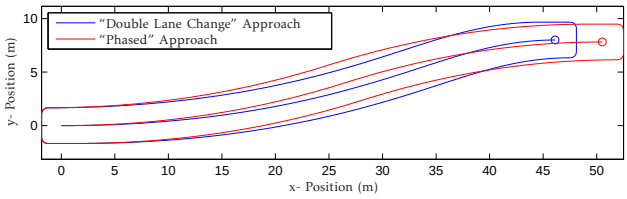

(a) Dual-Steer Dual-Brake (DSDB) Vehicle

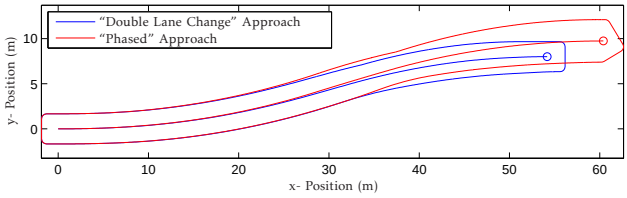

(b) Front-Steer Front-Brake (FSFB) Vehicle

Fig. 13: Overlay of the swept areas of vehicles performing the "double lane change" and "phased approach" maneuvers.

E. Double Lane Change Maneuver

The optimal trajectories corresponding to all vehicles during the "double lane change" maneuver are given in Figure 12. The performance of each vehicle is quantified by the longitudinal distance traveled. For the front-steer front-brake (FSFB) vehicle, the distance traveled towards the barrier is 54.17 meters. When rear-wheel steering and braking is added to the vehicle (DSDB), the distance decreases to 46.12 meters. A solution for the front-steer dual-brake (FSDB) vehicle was not found for this maneuver, likely related to the tendency for the controller to heavily utilize the rear brakes, thereby bringing the vehicle to a stop before the requisite end conditions can be obtained. Although these results suggest that adding rear-wheel control fields a significant improvement, such improvement is not apparent midway through the maneuver. In fact, as pinpointed with triangles in Figure 12, both the center of mass trajectory and the swept area of the DSDB vehicle protrude closer towards obstacles than for the FSFB. Such an observation implies that the "double lane change" maneuver, although designed to both avoid obstacles and return to a nominal driving condition, is in general a poor choice of an optimal control formulation. This "double lane change" approach is further compared and contrasted with the "phased" approach in the next section.

F. Discussion

The "double lane change" and "phased" approaches lead to differing conclusions about the maneuverability of the vehicles. For comparison purposes, the optimal trajectories of the FSFB and DSDB vehicles performing each maneuver are

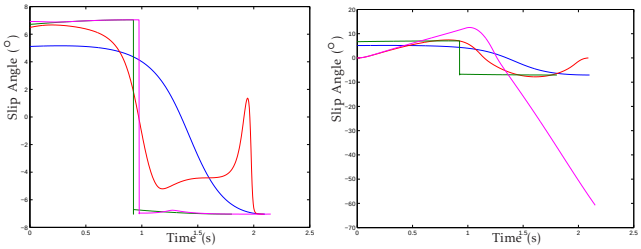

(a) Front Wheel (b) Rear Wheel

Fig. 14: Slip angles of each wheel during optimal maneuvers. Blue: DSDB Lane Change; Red: FSFB Lane Change; Green: DSDB Phased; Magenta: FSFB Phased

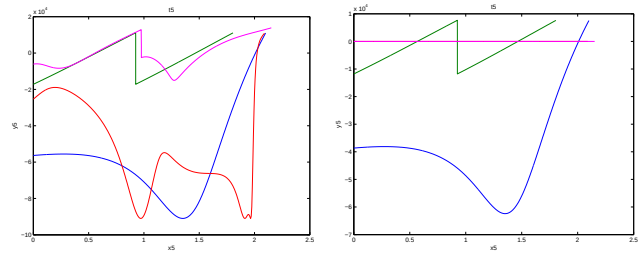

(a) Front Wheel (b) Rear Wheel

Fig. 15: Braking torques of each wheel during optimal maneuvers. Negative values represent braking torques; positive values represent accelerating torques. Blue: DSDB Lane Change; Red: FSFB Lane Change; Green: DSDB Phased; Magenta: FSFB Phased.

overlaid in Figures 13b and 13a. On one hand, the phased approach indicates that when an optimal "pure obstacle avoidance" maneuver is performed, it is difficult for the front-steering vehicles to avoid hitting the highway barrier. On the other hand, the trajectory of the "double lane change" approach is essentially identical to the phased approach for the first half of the maneuver. This plot indicates that for the FSFB vehicle, the "double lane change" maneuver may in fact be a much better approach than the "phased approach". The performance benefit of the "phased approach" is essentially nonexistent for obstacles passed during the first half of the maneuver.

The difference in the control strategies is most visible when considering the slip angle trajectories, as depicted in Figure 14. The "double lane change" approach sacrifices some of its front wheel control effort to maintain ideal rear wheel behavior. On the other hand, the "phased approach" uses its control inputs only in the interest of accomplishing the short-term goals of each particular phase. Interestingly, it only takes a small rolloff in the front wheel slip angle towards the end of the first phase of the maneuver to keep the rear wheel from breaking loose into a rally-car maneuver.

Contrary to the observations for the FSFB vehicle, the DSDB vehicle does much better at avoiding obstacles when using the "phased approach" than when using the "double lane change approach". This behavior occurs because the DSDB vehicle is in full control of the slip angle of both wheels at all times. It is not necessary to "sacrifice" some control

"Pure Obstacle Avoidance" maneuver					
State	Value	Costate	FSFB	FSDB	DSDB
$x_1(0)$	0 m	$\hat{\lambda}_1(0)$	1.0000	1.0000	1.0000
$x_2(0)$	0 m	$\hat{\lambda}_2(0)$	−3.2202	−3.1049	−3.1521
$x_3(0)$	0 rad	$\hat{\lambda}_3(0)$	−95.1838	−90.1177	−87.4835
$x_4(0)$	30 m/s	$\hat{\lambda}_4(0)$	0.9634	0.9795	0.9251
$x_5(0)$	0 m/s	$\hat{\lambda}_5(0)$	−2.7911	−2.6185	−2.9161
$x_6(0)$	0 rad/s	$\hat{\lambda}_6(0)$	−3.5193	−2.7202	−0.0000

"Barrier Avoidance" maneuver					
$x_1(0)$	27.74 m	$\hat{\lambda}_1(0)$	0.0000	0.0000	0.0000
$x_2(0)$	4.000 m	$\hat{\lambda}_2(0)$	1.0000	1.0000	1.0000
$x_3(0)$	0.5197 rad	$\hat{\lambda}_3(0)$	31.426	27.491	23.262
$x_4(0)$	27.356 m/s	$\hat{\lambda}_4(0)$	0.5760	0.5180	0.4341
$x_5(0)$	−5.7762 m/s	$\hat{\lambda}_5(0)$	0.9001	0.8629	0.7587
$x_6(0)$	0.6121 rad/s	$\hat{\lambda}_6(0)$	1.1313	0.6073	0.0000

"Double Lane Change" maneuver					
$x_1(0)$	0 m	$\hat{\lambda}_1(0)$	1.0000		1.0000
$x_2(0)$	0 m	$\hat{\lambda}_2(0)$	−2.5035		−1.8248
$x_3(0)$	0 rad	$\hat{\lambda}_3(0)$	−82.594		−66.7038
$x_4(0)$	30 m/s	$\hat{\lambda}_4(0)$	1.9902		2.1014
$x_5(0)$	0 m/s	$\hat{\lambda}_5(0)$	−2.9378		−2.2235
$x_6(0)$	0 rad/s	$\hat{\lambda}_6(0)$	−2.8153		0.0000

TABLE II: Initial states and associated optimal costates for selected optimal solutions. Additional solutions and values with more precision are available from the author.

effort on one wheel for the purposes of utilizing the other wheel in an effective manner.

VI. CONCLUSION

For a typical lightweight passenger vehicle traveling at highway-speed, this study has compared emergency maneuvers given varying objectives and controllable degrees of freedom. In all maneuvers, a vehicle with independently-controllable front and rear wheels including braking torques to each wheel was shown to perform better than the same vehicle without rear-wheel steering. Performance further decreases when braking capability is removed from the rear wheel. The performance of the vehicle under each maneuver was quantified using objective functions corresponding to physical distances. The performance benefit of active rear-wheel steering varies greatly depending on the initial vehicle state and maneuver objective. For the "pure obstacle avoidance" maneuver, the dual-steer dual-brake (DSDB) vehicle performs only slightly better than the front-steer vehicles. On the other hand, the DSDB vehicle performs much better given the "barrier avoidance" maneuver. The front-steer dual-brake (FSDB) vehicle also performs much better than the front-steer front-brake (FSFB) vehicle on the same maneuver.

For front-wheel steering vehicles, the "phased" approach of performing a "pure obstacle avoidance" maneuver and a "barrier avoidance" maneuver in sequence is shown not to offer a significant performance benefit over the "double lane change" approach. Therefore, the optimal "double lane change" maneuver seems to be an appropriate strategy for avoiding obstacles. However, for dual-steering vehicles, the "phased" approach offers significant advantages and is thus the more appropriate avoidance strategy.

At a high level, this research demonstrates that significant performance benefits can be realized by independent and active control of steering angles and wheel torques of both the front and rear wheels. In the most basic emergency maneuvers, the optimal control strategy is fairly intuitive. However, for more complex situations or with many control inputs, the maneuvers are often non-obvious. For example, a typical FSDB vehicle realizes a very significant performance benefit during a barrier avoidance maneuver by locking its rear wheel at certain points during the maneuver. Unfortunately, performance benefits appear to be the least significant during a pure obstacle avoidance maneuver. Instead, benefits are significant only when attempting to return to a nominal operating condition.

Due to the broad nature of this study, many extensions are possible. Pitch and roll dynamics could be added to the model in addition to independent control of all four wheels. Such additions would yield a comprehensive optimal control strategy but would be substantially more difficult to solve using the same optimal control methods. This research has shown that all optimal wheel force magnitudes are "bang-bang" in nature; therefore another extension is to research closed-loop controllers that maintain peak traction in the force directions such that the optimal behavior is still realized.

The main conclusion of this research is that active control of lighter, more agile vehicles with many controllable degrees of freedom is an interesting and potentially useful possibility for future vehicles.

References

[1] W. Chee and M. Tomizuka, "Lane change maneuver of automobiles for the intelligent vehicle and highway system," in *American Control Conference, Proceedings of the*, Baltimore, MD, 1994, pp. 3586–3587.

[2] C. Hatipoğlu, Ü. Özgüner, and A. Ünyelioğlu, "On optimal design of a lane change controller," in *Intelligent Vehicles 1995 Symposium, Proceedings of the*, Detroit, MI, 1995, pp. 436–441.

[3] Z. Shiller and S. Sundar, "Emergency lane-change maneuvers of autonomous vehicles," *Dynamic Systems, Measurement and Control*, vol. 120, pp. 37–44, March 1998.

[4] S. Bhat and A. Venkatraman, "Optimal planar turns under acceleration constraints," *IEEE Transactions on Automatic Control*, vol. 54, no. 7, pp. 1654–1660, July 2009.

[5] R. Isermann, M. Schorn, and U. Sthlin, "Anticollision system proreta with automatic braking and steering," *Vehicle System Dynamics*, vol. 46, no. 1, pp. 683–694, 2008.

[6] C. Hatipoğlu, Ü. Özgüner, and K. Redmill, "Automated lane change controller design," *IEEE Transactions on Intelligent Transportation Systems*, vol. 4, no. 1, pp. 13–22, March 2003.

[7] O. Mokhiamar and M. Abe, "Simultaneous optimal distribution of lateral and longitudinal tire forces for the model following control," *Dynamic Systems, Measurement, and Control*, vol. 126, no. 4, pp. 753–763, 2004.

[8] J. Ackermann, T. Bünte, and D. Odenthal, "Advantages of active steerng for vehicle dynamics control," in *Proceedings of the International Symposium on Automotive Technology and Automation*, vol. **32**, Vienna, Austria, 1999, pp. ME 263–270.

[9] A. Higuchi and Y. Saito, "Optimal control of four wheel steering vehicle," *Vehicle System Dynamics*, vol. 22, no. 5, pp. 397–410, September 1993.

[10] Y. Cho and J. Kim, "Design of optimal four-wheel steering system," *Vehicle System Dynamics*, vol. 24, no. 9, pp. 661–682, October 1995.

[11] E. Bakker, L. Nyborg, and H. Pacejka, "Tyre modelling for use in vehicle dynamics studies," *SAE Technical Papers #870421*, 1987.

[12] H. Geering, *Optimal Control with Engineering Applications*. New York, NY, USA: Springer, 2007.

[13] A. Bryson and Y. Ho, *Applied Optimal Control: Optimization, Estimation, and Control*. Brystol, PA, USA: Taylor & Francis, 1975.

[14] S. Boyd and L. Vandenberghe, *Convex Optimization*. Cambridge, UK: Cambridge, 2004.